UNIVERSITÀ DEGLI STUDI DI GENOVA

SCUOLA POLITECNICA

DIME

Dipartimento di Ingegneria Meccanica, Energetica, Gestionale e dei Trasporti

CORSO DI DOTTORATO IN INGEGNERIA DELLE MACCHINE E DEI SISTEMI PER L'ENERGIA, L'AMBIENTE E I TRASPORTI

Experimental Analysis and 1D Model Simulation of an Advanced Twin Stage Hybrid Boosting System

Tutor:

Chiar.ma Prof.ssa Ing. Silvia Marelli

Co-Tutor:

Chiar.mo Prof. Ing. Massimo Capobianco

Candidate:

Vittorio Usai

Experimental Analysis and 1D Model Simulation of an Advanced Twin Stage Hybrid Boosting System

Abstract

Due to the increasingly restrictive limits of pollutant emissions, electrification of automotive engines is now mandatory. For this reason, adopting hybrid boosting systems to improve brake specific fuel consumption and time-to-boost is becoming common practice. In this thesis an innovative turbocharging system is analysed, consisting in an electrically assisted radial compressor and a traditional turbocharger. As a first step, the steady-state performance of each component was measured at the University of Genoa test rig. Due to problems related to over temperature, the working time of the e-compressor coupled to the electric motor is limited avoiding an accurate evaluation of compressor efficiency. For this reason a driving system (instead of the electric machine) was designed to provide a more accurate evaluation of the compressor map. Subsequently another experimental campaign was carried out to evaluate the transient response of the entire turbocharging system. Two different layouts were compared: upstream and downstream. In the upstream configuration the electrically assisted compressor was placed in front of the traditional turbocharger, in the downstream configuration the e-compressor was positioned after the traditional turbocharger. The two different coupling configurations, upstream and downstream, were then modelled in 1-D simulation software following the dimensions and characteristics of the experimental line from which the exploited data originates. The models were first validated by emulating the steady-state condition and subsequently the transient response was simulated and analysed. Secondly, the transient response of the two layouts was compared, removing the constraints imposed by the experimental activity.

Contents

1. Introduction

Internal combustion engines have been the predominant mean of propulsion in passenger cars. The power to weight ratio, the compactness, the light weight and the low production cost of this energy system are four of the reasons why internal combustion engines have been used in passenger cars since the early development of vehicles. The main quality that makes internal combustion engines so widespread, however, is their ability to perform fast transients and work at high efficiency in off-design operating conditions.

Nowadays vehicles engines have to pass a severe procedure to be approved; driving cycles performed on roller bench or normalized paths are necessary for vehicles approval. In the European Union (EU) two driving cycles are adopted. Until a few years ago, for light commercial vehicles the NEDC (New European Driving Cycle) has been adopted, consisting of four urban path and an extra urban path for a total length of 11 km at an average speed equal to 33.5 km/h.

Since 2017 the new driving cycle called "Worldwide harmonized Light vehicles Test Procedure" (WLTP) is adopted for light duty vehicles [1]. Three different driving cycles were developed and represent three different vehicle classes, based upon a vehicle's power-to-mass (PMR) ratio and its maximum speed.

Class 3	PMR > 34	Low, middle, High, Extra High
Class 2	22<PMR≤34	Low, Middle, High
Class 1	PMR ≤22	Low, Middle

Table 1.1 – WLTP test Cycles
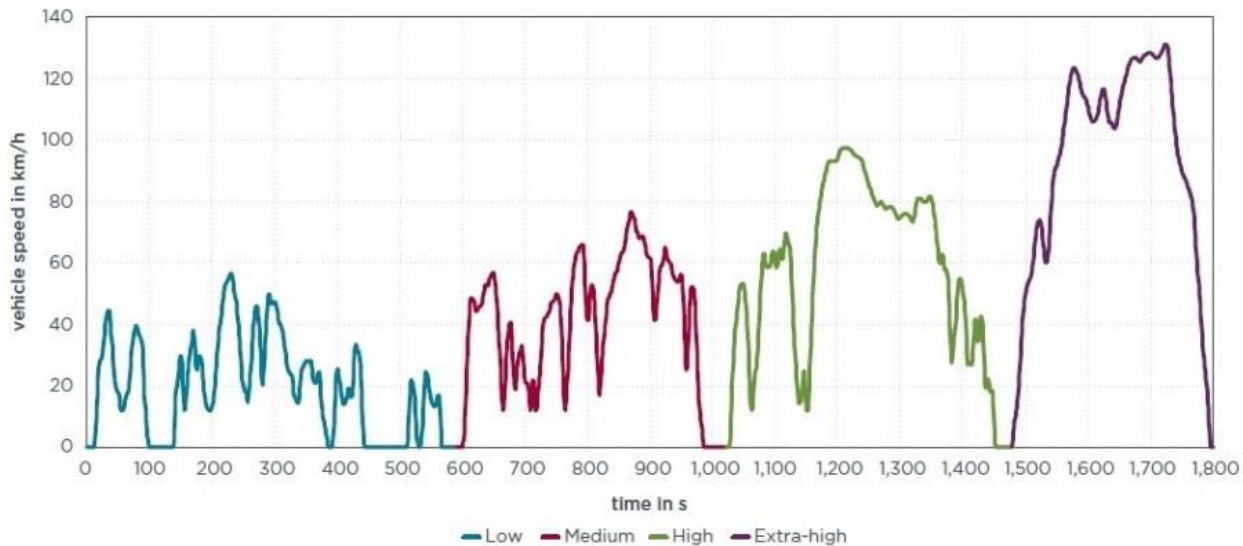
In figure 1.1 an example of cycle for class 3.

Fig. 1.1 Class 3 driving cycle pattern

Starting in 2017, the Real-Driving Emissions (RDE) test became part of the type-approval procedure for all new passenger cars [2]. The RDE test is an on-road emissions test meant to complement laboratory tests to ensure vehicle emissions are similar during normal, real-world operating conditions as they are during laboratory testing. To ensure a technological transition, the EU Parliament adopted "conformity factors" (CF). In 2017 (phase 1 of RDE), this factor was set at 2.1, this means that a vehicle may initially emit 2.1 times as much as it does when test under laboratory conditions – whereby the vehicle is driven on a real road, where the driving situation described above can arise, leading to increased emissions. Since 2020 (phase 2 of RDE), the conformity factor has been reduced to 1.5. The RDE test procedure was initially developed in Europe for European vehicles but a new Global Technical Regulation (GTR) and UNECE Regulation on RDE are under development.

The increasingly restrictive limits on pollutant emissions imposed in recent years are pushing OEMs (Original Equipment Manufacturers) towards the development of low emissions vehicles. The European Commission and ACEA (Association des Constructeurs Européens d'Automobiles) periodically provide new targets in terms of the CO2 emissions to the OEM [3]. In recent years in order to take into account the limit imposed by the legislator the OEMs important research program are carrying on to reduce the fuel consumption. Recent evaluations highlight good improvement in CO2 emissions: in 2010 the medium emission of the registered vehicles was 140 g/km, in 2020 108.2 g/km.

In a long-term scenario hydrogen fuel cell propulsion or battery electric vehicles (BEV) [4] will be the most adopted solutions. These technologies are not yet ready to be produced and sold on a large scale, as they still have some important disadvantages such as a high initial cost, short driving range and long charging times [5]. For this reason, at least for the next two decades, it seems more reasonable to assume a gradual transition, characterized by the integration of electrical components coupled to internal combustion engines [6]. The development of hybrid electric vehicles (HEV) is necessary to obtain powertrains with greater efficiency than conventional internal combustion engines, with a lower initial price and greater driving range than electric vehicles. Besides, the energy source for the road transportation sector represented by fossil fuels will continue to prevail for the next decades, thanks to a more substantial adoption of advanced liquid and gaseous biofuel [7] to promote a progressive substitution with renewable energy sources. In recent years, car manufacturers are still improving the powertrain performance and efficiency with particular attention to spark ignition engines. Spark ignition engines have become the majority in recent years thanks to lower particulate and NOx emissions than Diesel engines. Direct gasoline injection is now the standard for mitigating knock and subsequently increasing the engine compression ratio [8]. If injected directly into the combustion chamber, the fuel will evaporate absorbing heat and reducing the in-cylinder temperature. Another effective way to improve the spark ignition engine efficiency, both at part and full load, is provided by the Variable Valve Actuation (VVA) system [9]. Thanks to VVA systems it is possible to independently define the lift and timing of the valves; this solution allows to limit the pumping losses caused by the throttle valve. Moreover, this technology allows to implement different strategies such as Early Intake Valve Closure (EIVC) and Late Intake Valve Closure (LIVC). Teodosio et al. [10] studied the influence of different valve strategies on fuel consumption and knock tendency using a hierarchical 1D/3D numerical approach: they found a significant reduction in Brake Specific Fuel Consumption (BSFC) (for example at low load, comparing EIVC strategies to full lift strategies a 5.6% improvement was found in BSFC). However, the EIVC and LIVC strategies penalized the volumetric efficiency and therefore an adequate boosting system is necessary to provide the required torque. Two stage turbocharging systems are a good solution to provide the high boost pressure required by EIVC and LIVC. Zheng et al. [11] performed a theoretical analysis and an experimental study on the effects of a two-stage turbocharging system on engine performance, found that inter-stage cooler improves the efficiency of the engine and that the better

fuel economy can be made by compromising engine boost pressure and pumping losses. However, turbocharging is the most common solution for providing boost pressure despite turbo-lag [12] and several researchers have analyzed different solutions to mitigate the impact of turbo-lag on vehicle drivability. Fun to drive and drivability are important issues in modern vehicles, and the propulsion system plays a key role in achieving these goals. Today most engines are characterized by the presence of a turbocharging system to achieve a high level of specific power and efficiency. Unfortunately, turbocharged engines are characterized by a delay in the delivery of toque, especially at low load and low speed, a phenomenon commonly called turbo-lag. Sandoval et al. [13] develop a computational technique with the aim to identify the transient behavior of the turbocharger in a vehicular application. In Figure 1.3 different engine load pattern are indicated schematically on the compressor map [14].
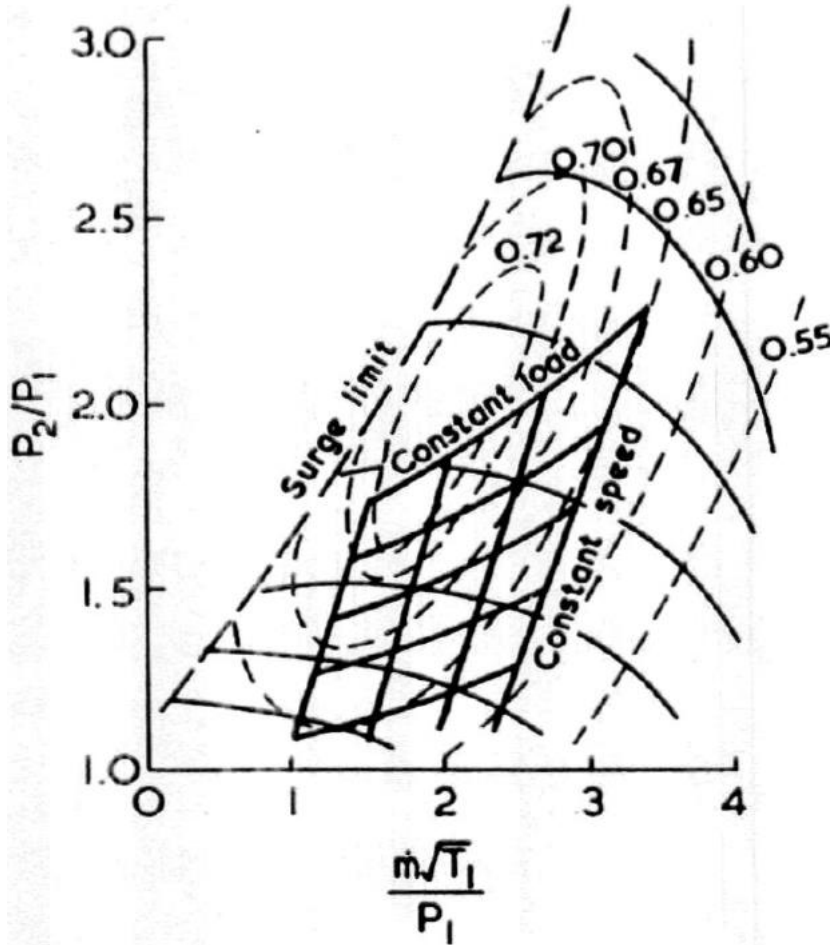
Figure 1.2 – Example of possible engine transient condition reported on compressor map

In order to predict the transient response of turbochargers the definition of an acceleration parameter is useful. The angular acceleration of the turbocharger ($\frac{d\omega}{dt}$, where ω is the angular speed) depends on its moment of inertia (J_{TC}) and on the excess turning moment available for acceleration (ΔC_{TC}):

$$\frac{d\omega}{dt} = \frac{\Delta C_{TC}}{J_{TC}} \qquad (1.1)$$

3

The time required to accelerate to a certain speed (t_b) could be obtained integrating the equation of the angular acceleration of the turbocharger:

$$\int_0^{t_b} \frac{\Delta C_{TC}}{J_{TC}} \, d\tau = \omega_b - \omega_0 \qquad (1.2)$$

Where ω_b is the rotational speed target and ω_0 is the initial rotational speed.

However, the integral of the excess torque is not readily obtained: to determine the acceleration of the turbocharger would require step-by-step computation of turbine and compressor power including complete computation of the engine cycle, with a large amount of computational effort.

For the purpose of comparing different turbocharger design, an acceleration parameter B can be defined as follow in equation 1.3:

$$B = \frac{J_{TC}\omega_b^2}{M_C \eta_c \eta_t \eta_m \Delta h_c} \qquad (1.3)$$

Where $\eta_c \eta_t \eta_m$ are the compressor, turbine and mechanical efficiency respectively, M_C the compressor mass flow rate and Δh_c the compressor specific enthalpy.

The parameter B is defined as a time, as the value of the acceleration parameter increases, the acceleration becomes slower. Despite the fact that the unit of the parameter is a time this is not the time required for the acceleration.

Under the conditions of geometric similarity, the parameter B is directly proportional to the geometric turbocharger size. In other words, the parameter B increases with the size of the turbocharger. Thus, it may be more favorable to use several small turbocharges instead of a large one. On this topic Albin Rajasingham [15] confirm that two turbocharging units which are placed in series allows a fast transient increase in load and at the same time a high specific power. Keller et al. [16] present a prototype demonstrator vehicle equipped with a two-stage sequential turbocharging system and low pressure EGR (Exhaust Gas Recirculation). The twin stage turbocharged engine has an increased specific power output and can be downsized to increase the efficiency. Moreover, by using the EGR system at high load the in-cylinder temperature can be lowered reducing knock tendency and exhaust gas temperature. Tang et al. [17] compare the transient performances of several kinds of exhaust gas turbocharging (EGT), the system that they analyzed are three: steam-assisted turbocharging (SAT), electronically controlled turbocharging (ECT) and supercharger-exhaust gas turbocharging (SET). A turbocharged gasoline engine, on which was conducted bench test firstly to get basic data for building and calibrating the simulation model, was employed as the study object. The results show that SET, SAT and ECT can reduce the response time and fuel consumption in acceleration process. The response time of various turbocharging approaches follows the descending sequence of EGT, SAT, ECT and SET. At the speed of 2000 r/min (from idling to full load), compared with EGT engine, the specific fuel consumption (SFC) of SET engine is decreased by 23.3%, while it can be reduced by 38.2% and 36.3% in SAT engine and ECT engine, respectively. Finally, to reveal the improvement potentials of SAT and ECT, both of them were re-matched with a larger turbine without wastegate. The results indicate that the torque and thermal efficiency of SAT and ECT engines can be further improved, while the acceleration equilibrium time is increased. Rinaldini et al. [18] propose a triple turbocharger system. Their study is based on a current SI GDI V8 turbocharged engine modeled by means of CFD tools. The triple turbocharging system shown in figure 1.3 is conceptually similar to a two-stage system, the only different is that the high pressure stage is made by two compressor in parallel instead of one. The low pressure stage consists in a bigger turbocharger, delivering a flow rate about two times higher than that of the single bank turbocharger, in a conventional

system. Conversely, the high pressure turbochargers are much smaller, since they are completely by-passed at an engine high rotational speed (about 3500 rpm). Furthermore, at low engine speed, the low pressure compressor delivers a charge already compressed to the high pressure stage, whose maximum volumetric flow rate is therefore reduced, in comparison to a compressor with ambient induction. The triple turbocharger, in comparison to the twin stage configuration provide some advantages such as higher boost pressure at low engine speed, lower pumping losses at high speed and a better transient response.
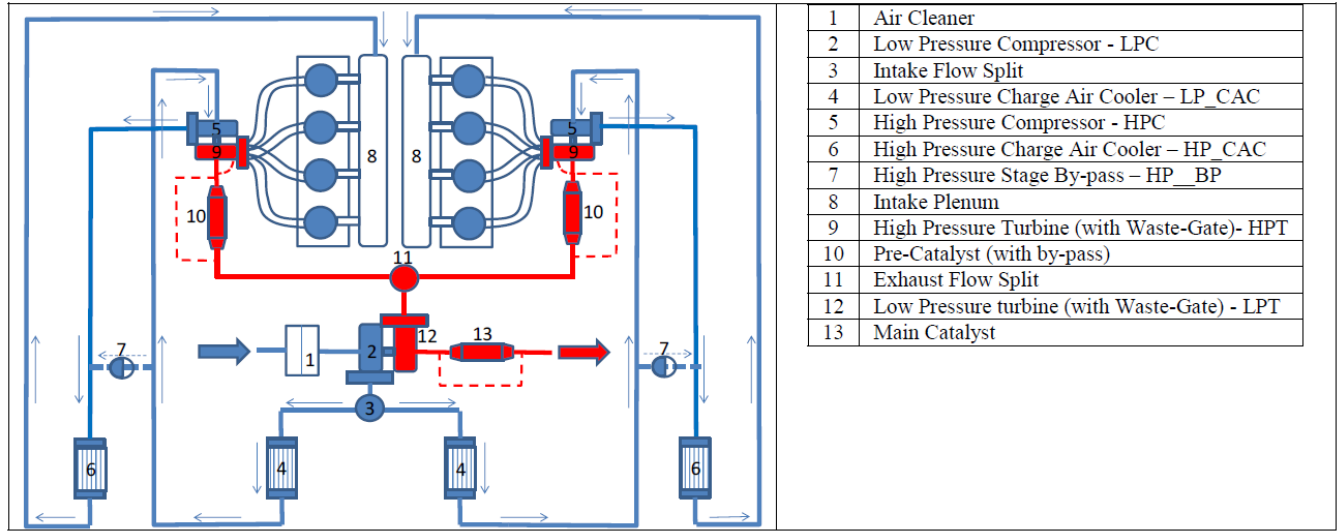

1	Air Cleaner
2	Low Pressure Compressor - LPC
3	Intake Flow Split
4	Low Pressure Charge Air Cooler – LP_CAC
5	High Pressure Compressor - HPC
6	High Pressure Charge Air Cooler – HP_CAC
7	High Pressure Stage By-pass – HP__BP
8	Intake Plenum
9	High Pressure Turbine (with Waste-Gate)- HPT
10	Pre-Catalyst (with by-pass)
11	Exhaust Flow Split
12	Low Pressure turbine (with Waste-Gate) - LPT
13	Main Catalyst

Figure 1.3 – Layout of the triple turbocharger proposed by Rinaldini et al. [17]

In recent years thanks to the propulsion system hybridization different authors propose advanced solution to improve the dynamic performance of the turbocharging systems. The aim of the boosting system electrification is the increase in the turning moment available for acceleration (ΔC_{TC}) thanks to the power provided by an electric motor. For example, Tang et al. [19] investigated several types of improved exhaust turbochargers and analyzed their transient response. The Authors found a noticeable improvement in specific fuel consumption and transient performance of the turbocharger. One of the most promising solutions today is represented by the Electrically Assisted Turbocharger (EAT). A high-speed electric machine is installed between the compressor and the turbine. At low rotational speeds, the electric machine works like a motor, providing additional torque to the compressor. As a result, the boost pressure is increased, which results in a reduction in the transient response [20]. On the other hand, at high engine speed, the electric motor works as a generator, producing power and transmitting energy to the batteries. Current research states that EAT brings several benefits, as well as a large reduction in turbo-lag. The electrically assisted turbocharger maintains its speed during gearshift, additionally, turbocharger speed is reduced at higher engine speeds [21]. Mattarelli et al. [22] evaluate the pros and cons of MGU-H technology when applied on engine on different displacement for passenger cars. The maximum advantage in term of fuel economy on the fuel economy is achieved for the smaller displacement engine. However, in the bigger engine configuration it is possible to strongly simplified the turbocharging scheme thank to the adoption of one e-turbo instead of two traditional turbochargers. Moreover, the elimination of the turbo-lag allows the designer to adopt more fuel efficient settings. Of course, this technology has some drawbacks. As the electric machine provides the connection between

5

the compressor and the turbine, the shaft inertia is increased. Therefore, more power is required for the turbocharger operation. Furthermore, additional cooling is needed required to prevent the effects of high temperatures on the electric machine.

Lee et al. suggested a different approach to the electric machine installation. With the usage of clutches the machine could be connected or disconnected from the shaft as it is installed outside the turbocharger assembly [23].

In [24] a new layout of the boosting system which consists in a compressor and turbine decoupled to work independently is presented. The compressor is driven by a motor to avoid the turbo-lag, and the turbine is controlled to work at high efficiency zone by using the speed optimization strategy. Results showed that the system seems to be a good solution to improve fuel economy of the engine in different operating conditions. An et al. [25] develop a two stage turbocharger system with electric supercharger, in their paper introduces the result of the engine bench test and simulation using engine simulation tool. As a result of the tests on a 1.5 liter gasoline engine, the electric two-stage turbocharger demonstrated the 43 % improvement in the response time at 1500 rpm if compared to the normal two-stage turbocharger. Moreover, the electric two-stage supercharger improve the catalytic activity at the cold start since the turbine outlet temperature is 100 °C higher than the two-stage turbocharger.

Therefore, turbocharging layouts have been developed in recent years, coupling an electrically driven compressor with a traditional one. The low inertia of the e-compressor guarantees an excellent response in the event of a torque request, improving the readiness of the system. This is advantageous not only because the time to boost is reduced, but also because the engine back-pressure is limited. In addition, the boost pressure at low engine speed is increased compared to a conventional unit. Since the compressor is electrically driven by an electric machine, the control is much more flexible. However, this type of technology does not have the ability to generate power, requiring greater battery capacity coupled with other generation solutions, such as a regenerative braking system.

Furthermore, the voltage required by this system proves to be a challenge. A normal automobile is designed to work on a 12V architecture, while the e-compressor needs a 48V one to work at high performance. A study by Nishiwaki et al. [26] stated that a 48V system, thereby producing more power, provides an increase in regenerative electrical power and an increase in overall engine power as boost pressure increases.

This work aims to highlight the benefits in terms of transient response on the adoption of an e-compressor coupled with a traditional turbocharger in both upstream and downstream configurations. A recurrent example of this type of configuration is presented in Figure 1.4, where a detailed system overview of the turbocharger assembly and its different modes of operation on the new generation of V6 TDI engines is provided.
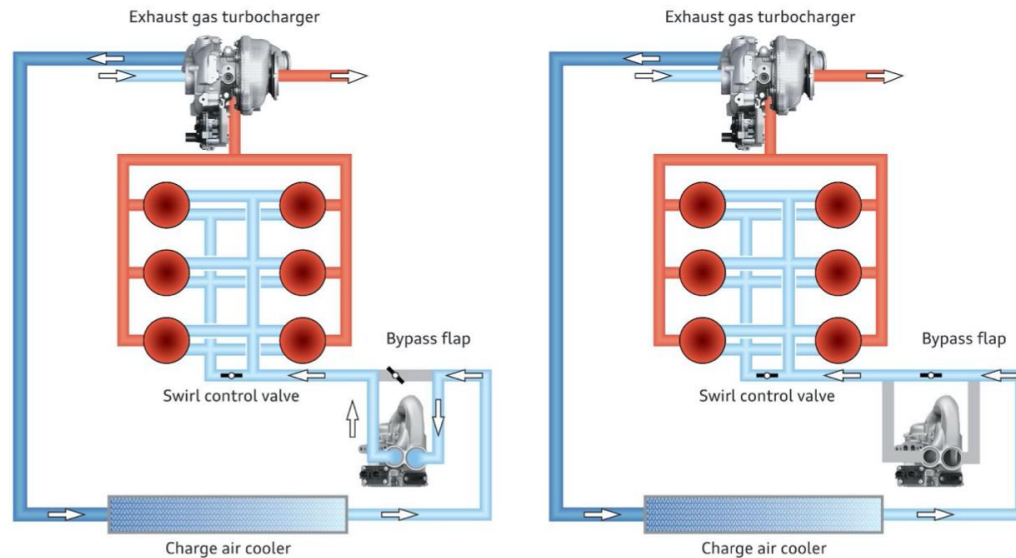
Figure 1.4 – Example of e-compressor application and working scheme [27]

After compression, the fresh air drawn in by the turbocharger is routed via a charge pressure pipe on the left-hand side of the engine to the on-board charge air cooler. From there, the cooled charge air flows towards the e-compressor. Depending on the dynamic response demanded of the engine, a 2/3-way throttle valve varies its position to route the air either directly to the engine or to the e-compressor. If the e-compressor support is requested when starting off and accelerating, the valve closes off the direct flow to the engine and routes the charge air compressed by the turbocharger to the e-compressor, which compresses it further before it is routed back into the air flow to the engine downstream of the valve. Moreover, the introduction of an e-compressor which is able to support the engine independently from the engine speed, allows to install a larger capacity conventional turbocharger which usually lacks transient performance at low speeds. The optimization of the combined operation of both machines delivers both instant response at low speeds and high performance at the higher rotational speeds.

2. Experimental Set-up and Measuring Equipment

The experimental investigations described in this thesis utilized the test rig for components of propulsion system of the University of Genoa. This chapter describes the characteristics and capabilities of the test bench, measurement system and acquisition system.

The test bench's open loop configuration allows an independent analysis of the compressor and the turbine in both steady and unsteady conditions. To test the compressor, the power into the system is controlled by regulating the airflow upstream of the turbine, as the turbine acts as a controlled power source into the system. To test the turbine, the compressor acts as a controlled load on the system by regulating the pressures at the compressor inlet and outlet. An electrical heater and three screw compressors control the operating conditions at the turbine inlet. Combined the screw compressors can provide 0.65 kg of air per second to a maximum pressure of 8 bar and temperature of 750 °C. The ability to reach these conditions allows the test bench to replicate engine exhaust gas conditions. The test bench's pulse generators allow the system to reproduce the pressure oscillations seen when opening and closing the intake and exhaust valves in an engine with varying degrees of accuracy. The pulse generators can be placed at either the compressor outlet or the turbine inlet, depending on the test being conducted.

The sensors installed in the test bench measure mass flow rate, static pressure, total temperature, rotational speed and valve position. The measurement system collects the time average of all parameters for measurements during steady state conditions and the instantaneous values during transient or unsteady conditions. The lab operator can control testing parameters and collect data using the control room's pneumatic, electronic, and digital interfaces with the test bench.

2.1 Test Bench Description

The test bench, shown in Fig. 2.1 can be divided in the following systems: the Compression Unit, the Working Fluid Circuit, the Auxiliary Fluid Conditioning System and the Control System. The Compression Unit supplies the required air flow rate and pressure for different sizes of turbochargers. The Working Fluid Circuit provides treated air at set conditions to the compressor and turbine using air filter, drier, and heater. The air filter and drier pretreat the air to prevent damage to the measuring equipment and turbocharger components. The heater regulates the turbine inlet temperature to avoid ice formation on blades and guarantee test repeatability. The Auxiliary Fluid Conditioning System provides oil and coolant to the turbocharger and motor head, if the motor head is present. The Control System allows the operators to visualize and collect relevant test parameters and command the behaviors of the systems remotely.
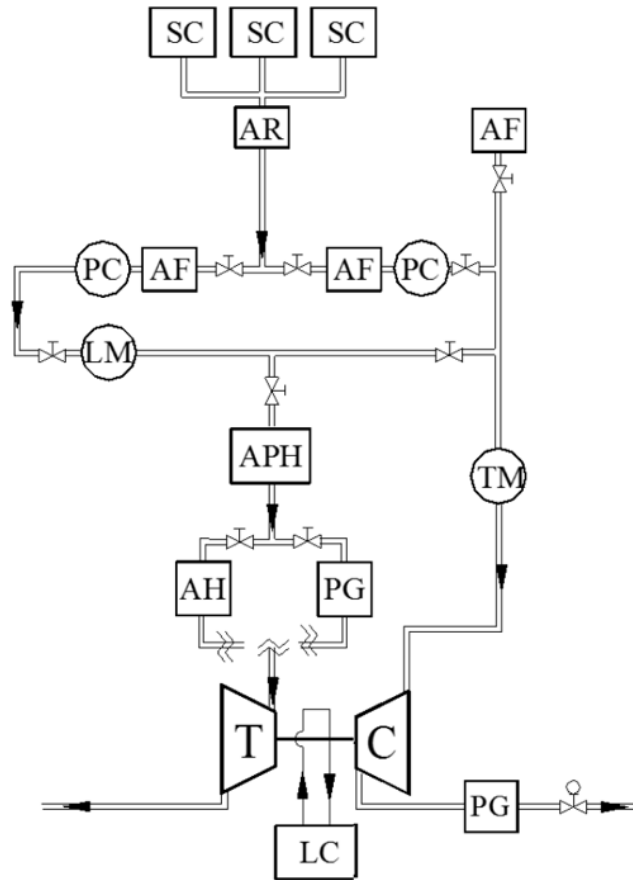
AF	Air Filter	LM	Laminar Flow Meter
AH	Air Heater	PC	Pressure Control
APH	Air Pre-Heater	PG	Pulse Generator
AR	Air Reservoir	SC	Screw Compressor
C	Compressor	T	Turbine
LC	Lubricating Circuit	TM	Thermal Mass Flow Meter

Fig. 2.1 – Schematic representation of the test rig for components of propulsion system of the University of Genoa.

2.1.1 Compression Unit

Located outside the test cell, the compression unit provides the pressure and air flow into the turbocharger. The three screw compressors (two KAESER model CSD 122 and one DEMAG) are located outside the testing room and operate in parallel, producing a total mass flow rate of 0.65 kg/s. The two KAESER compressors can produce the required mass flow rate for most test conditions by working in parallel: one compressor works continuously, while the second one is active during demand peaks. The compressors switch roles after several hours to guarantee similar utilization in both machines. The DEMAG compressor acts as a redundancy to support the two KAESER compressors.

The KASER compressors operate using a 380 V and 50 Hz frequency three phase supply, requiring a maximum power of 75kW each. Each compressor can provide a maximum air mass flow rate of 0.22

kg/s, considering an ambient temperature of 30 °C and a maximum pressure of 8 bar gaug [28]. The various components that make up a KAESER screw compressor are shown in Appendix A. Ambient air flows through the filter (1) and expansion valve (2) to reach the screw compressors (3). The expansion valve regulates the pressures at each machine's inlet and avoids high mass flow rate oscillations during fast flow rate transients. Because the working fluid is a mixture of lubricating oil and air, it is necessary to insert an air oil separator (5) at the compressor outlets. After the separation of the oil and air mixture, the cooler (6) chills the fluid to a temperature of 5 to 10 °C higher than ambient.

2.1.2 Working Fluid Circuit

The circuit is shown in Figure 2.2 and Figure; Table A-0.1, located in Appendix A, provides the legend for these figures. The air feeding line begins downstream of the compression unit and provides air to both the compressor and turbine in an open circuit configuration. The circuit can be divided in the following five sublines: the common feeding line, the turbine feeding line, the compressor feeding line, the turbine outlet line and the compressor outlet line.
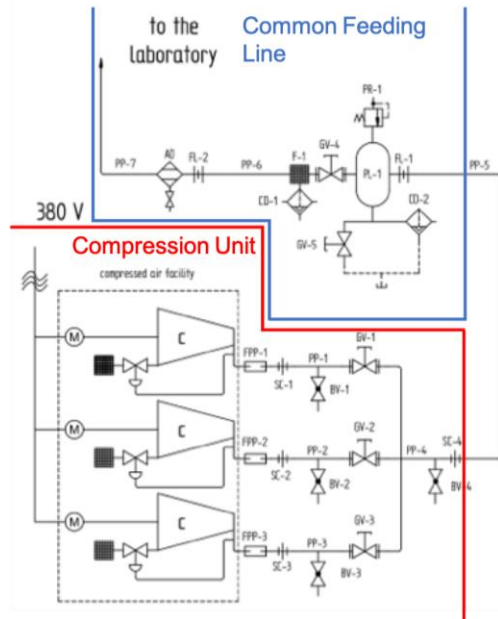

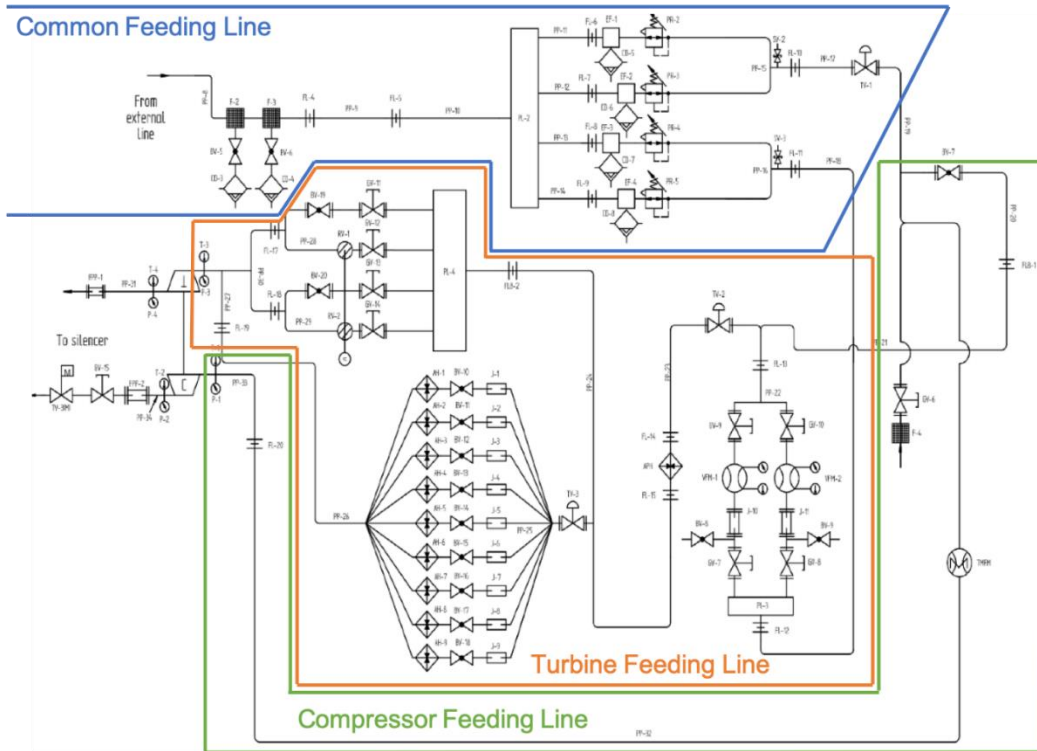*Figure 2.2 – Working fluid circuit external to the lab*

Figure 2.3 – Working fluid circuit internal to the lab

2.1.2.1 Common Feeding Line

The air provided by the compression unit is stored in an air reservoir, indicated by PL-1 in Figure2.4. The air reservoir has a capacity of 3 m^3 and a security valve (PR-1 in Figure) which activates if the reservoir pressure exceeds 12 bar, nominal pressure of the vessel. The purpose of this component is to reduce air oscillations generated by transient or unsteady turbocharger operation and compensate for the different mass flow rates between the compression unit and turbocharger. At the reservoir outlet, the air crosses a purifying and treatment system. The first component is a filter (F-1 in Figure) and the second is an air dryer (AD in Figure). The dryer unit contains one air to air and one air to glycol mixture heat exchanger, which remove condensation to avoid damage in critical downstream equipment.
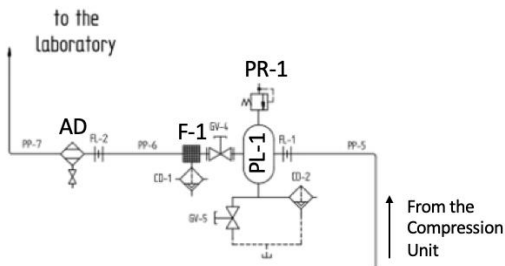

Figure 2.4 – External common feeding line, segment from Figure 2.2

The air then enters the lab, and two Zander filters complete the air treatment, indicated as F-2 and F-3 in Fig. 2.3. The Zander filters have a cut-off diameter of 1 μm and of 0.01 μm to allow a maximum oil concentration of 0.001 mg/m^3 [29]. A distributor (PL-2 in Figure) regulates the amount of treated air provided to the two parallel lines that independently feed the compressor and turbine. Each feeding line contains two pneumatically powered pressure reducers arranged in parallel (PR-2, PR-3, PR-4 and PR-5 in Figure). Two relief valves activate in case of a malfunction of the pressure reducers to avoid damage

11

to the turbocharger or measurement equipment. An additional safety device interrupts air flow to the turbocharger if the lubricating system has failed.
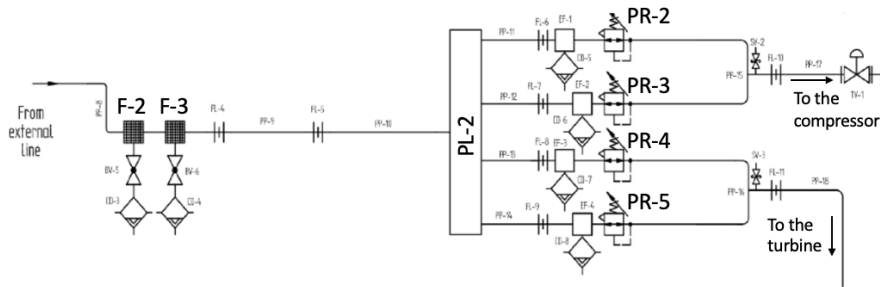

Figure 2.5 – Internal common feeding line, segment from Figure

2.1.2.2 Turbine Feeding Line

Downstream of the common feeding line, the turbine feeding line includes a pressure control station, another air reservoir (PL-3 in Figure 2.6) and two parallel air flow rate measuring systems (VFM-1 and VFM-2 in Figure 2.6). The air flow rate measuring systems are laminar flow meters which measure a maximum air flow rate of 100 l/s and 200 l/s and can be used in three different configurations: for low mass flow rates the 100 l/s sensor is used, for high mass flow rate the 200 l/s sensor is used, for mass flow rates that exceed 200 l/s both measuring systems are used in parallel [30] To select a configuration, the stop valves (GV-7, GV-8, GV-9 and GV-10 in Figure 2.6) are either opened or closed.
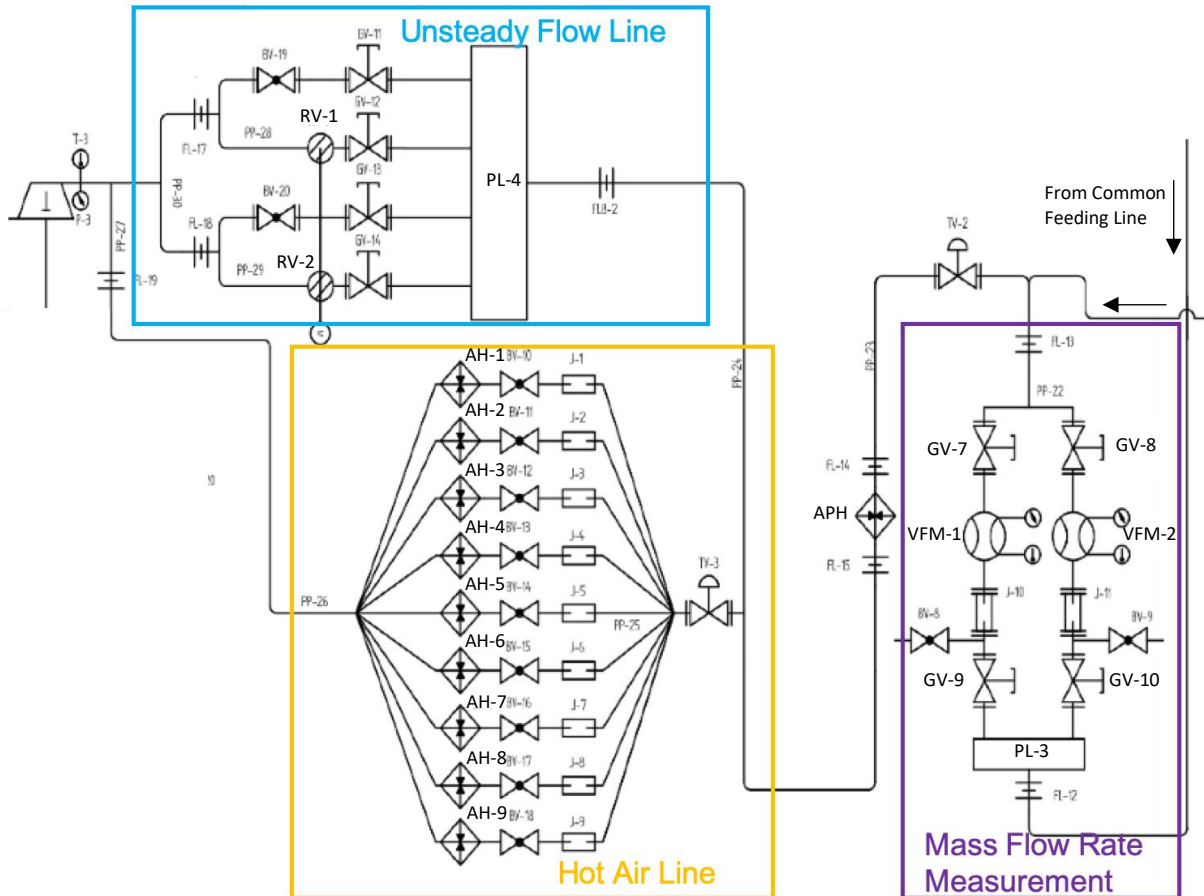

Figure 2.6 – Turbine feeding line, segment from Figure

Immediately downstream of the Mass Flow Rate Measurement segment, the turbine feeding line contains an electric air preheater (APH in Figure 2.6). This device is used to avoid ice formation in the turbine outlet pipe if a high expansion ratio is required. The maximum heating power is 54 kW and can preheat the air to 110 °C at the maximum air flow rate. The temperature can reach higher values at lower air flow rates but is limited to 120 °C for lab safety. Further downstream of the air preheater there are two parallel branches allowing two types of testing: the first branch contains a pulse generator system and is used for unsteady flow tests (Unsteady Flow Line in Figure 2.6), the second branch contains an electric heater used for high turbine inlet temperature tests (Hot Air Line in Figure 2.6). When performing unsteady flow tests the air preheater is used to increase the turbine inlet temperature.

A vessel (PL-4 in Figure 2.6) with a capacity of 60 liters is the first component in the unsteady flow line. The vessel feeds four lines: two with the pulse generator systems (RV-1 and RV-2 in Figure 2.6) and two that are simple pipes. The lines with the pulse generator systems determine the frequency of the oscillations in the flow while the other two lines regulate the steady component of the flow which will affect the oscillation amplitude once the two flows mix. For most tests only one pair of pulse generator and steady line are needed but having two of these sets of lines provides the capability to test double entry machines. The pulse generator system consists of a rotary shutter valve, shown in Figure. The valve has two parts: a hollow cylindrical stator and a rotor with a diametrical slot. An electric motor controls the pulse frequency.

Figure 2.7 – Rotating valve used in the pulse generator system

The hot air line is used when performing high temperature steady flow tests (The maximum turbine inlet temperature is about 600 °C, on the basis of the turbocharger size and the quality of the piping insulation). The heater increases the thermal power to 324 kW and is composed of nine Sylvania SureHeat MAX F074735 heating elements (AH-1 to AH-9 in Figure 2.6 and shown in Figure) [31].
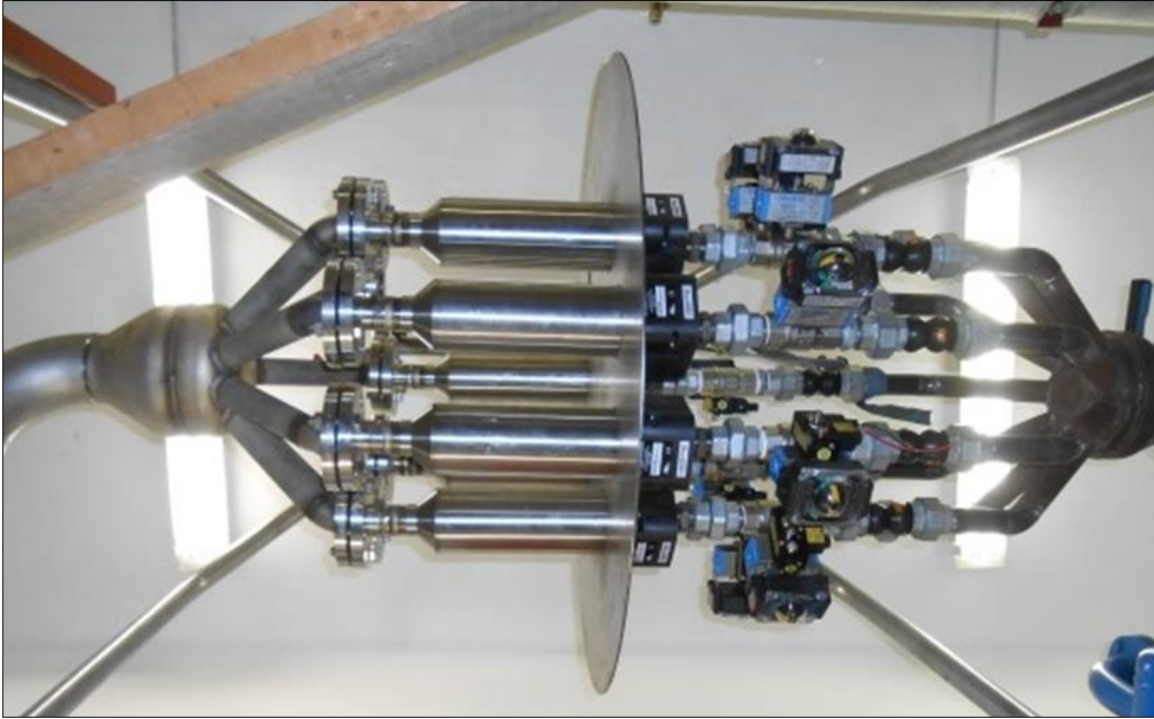
Figure 2.8 – Electrical heaters used in the hot air line

Each heating element has an electro-pneumatic valve that allows a specific number of elements to be used, BV-10 to BV-18 in Figure 2.6 and shown in detail in Appendix A. The number of heating elements used depends on the mass flow rate required by the turbine: if too many heating elements are used, the heat produced will not be absorbed by the air and may damage the heaters; if too few heating elements are used, the desired temperature may not be reached.

2.1.2.3 Compressor Feeding Line

As shown in Figure, two separate lines can be used to feed air to the compressor: the filter compressor feeding line sucks air from the test lab through a filter (F-6 in Figure), while the controlled pressure feeding line is connected to the common feeding line and provides pressurized air to the compressor. Valves TV-1 and GV-6 shown in Figure allow the operator to select the line used to feed the compressor. A ventilator is activated when the compressor is not fed through the common feeding line to compensate for the air the compressor is removing from the room. When the compressor is connected to the common feeding line, the mass flow rates to the compressor and to the turbine can be regulated with valves TV-1 and BV-7 shown in Figure. Downstream of the valves GV-6 and TV-1, the two lines merge and pass through a mass flow rate sensor (THMF in Figure) before entering the compressor.
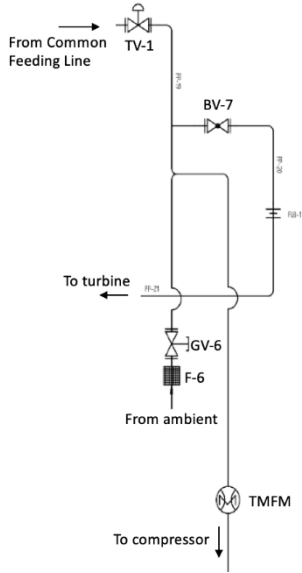
Figure 2.9 – Compressor feeding line, segment from Figure

2.1.2.4 Turbine Outlet Line

The exhaust air from the turbine is discharged outside the lab. The air exits the lab and enters a silencer to avoid excessive noise during unsteady flow investigations, as shown in Figure.
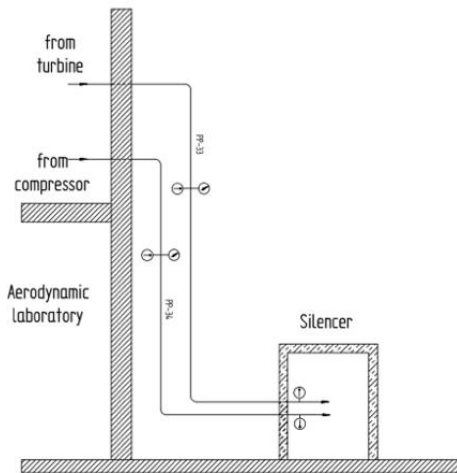

Figure 2.10 – Turbine and compressor external outlet line

2.1.2.5 Compressor Outlet Line

The first part of the pipe at the compressor outlet contains the measurement equipment while the second contains a motorized throttle valve; this consists of a UNITECH TF series DN 65 butterfly valve motorized by a VALPES ER35.X0B.G00 model actuator [32]. The throttle valve, shown in Figure , regulates the compressor operating point and the power absorbed by changing the circuit external characteristic. After crossing the butterfly valve, the air is sent to the silencer discussed in Appendix A, 2.1.2.4 Turbine Outlet Line.
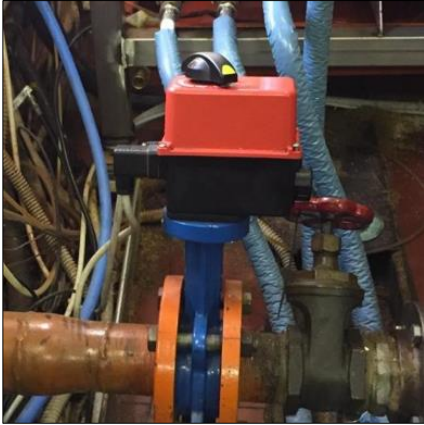
Figure 2.11 – Motorized throttle valve

2.1.3 Auxiliary Fluid Conditioning System

The Auxiliary Fluid Conditioning system is responsible for the lubrication and cooling of the turbocharger and cylinder head. The system consists of three lines: a lubrication line cycling oil, a coolant line cycling a water-glycol mixture, and a water-glycol line used for cooling of the other two lines. The system is shown in Figure 2.12. The lubrication line stores oil in the reservoir, S1, and uses two 5kW resistances and the plate heat exchanger, SC1, to control the oil temperature. Oil is pumped from the reservoir to the heat exchanger, PR1, and from the reservoir to the turbocharger and cylinder head, P1. The lubrication line uses a gravity fed return where used oil is collected in a reservoir at the lowest point of the system, this oil is then pumped back into the main reservoir, S2 and P2. The coolant line is designed similarly to the lubrication line, a water-glycol mixture is stored in a reservoir, S3, and the coolant temperature is controlled by a resistance in the heat exchanger, SC3. Pumps P3 and PR3 circulate the coolant through the turbocharger and heat exchanger. The common water line stores chilled water in a reservoir, S4, feed by the public water supply. If either the oil or coolant is being cooled the water is fed into one, or both, of the plate heat exchangers.
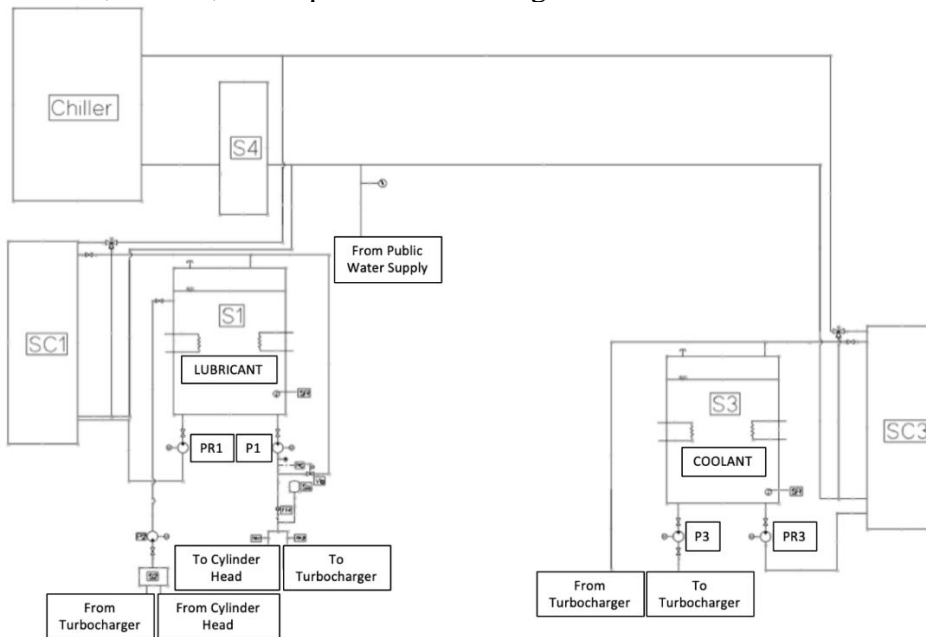

Figure 2.12 – Auxiliary fluid conditioning system

2.1.4 Control System

The control room provides the test operator with a safe work station, separated from the temperatures, pressures, and failure risks of the test cell. With a large window into the test cell, the control room's console provides the test operator with the pneumatic and electrical command signals for the system, several initial feedback interfaces, and circuit calibration equipment. The control console's command interface includes: manual valve controls for the compressor and turbine inlet pressures, a closed-loop temperature control system for the Auxiliary Fluid System, open-loop system to power the compressor outlet butterfly valve, a touchscreen console for closed-loop control of the electric air heaters, the test cell ventilation power button and fan speed control, the air dryer power and trigger buttons, and the compression unit power activation switches. The control console's feedback interface includes pressure gauges from the turbine and compressor inlets, the compressor outlet butterfly valve position, signals from the LabVIEW digital data acquisition system, feedback from the display for the electric air heaters, current temperatures in the Auxiliary Fluid System, and oil pressures. These interfaces are labeled in 2.13. The LabVIEW digital data acquisition system uses one computer for high sample rate measurements and another system for time-averaged measurements; Appendix A discusses the two LabVIEW interfaces and their digital data acquisition in detail. Six manometers are located behind the control console and are used to calibrate the circuit's pressure transducers discussed in paragraph 2.2.3 Pressure Measurements.
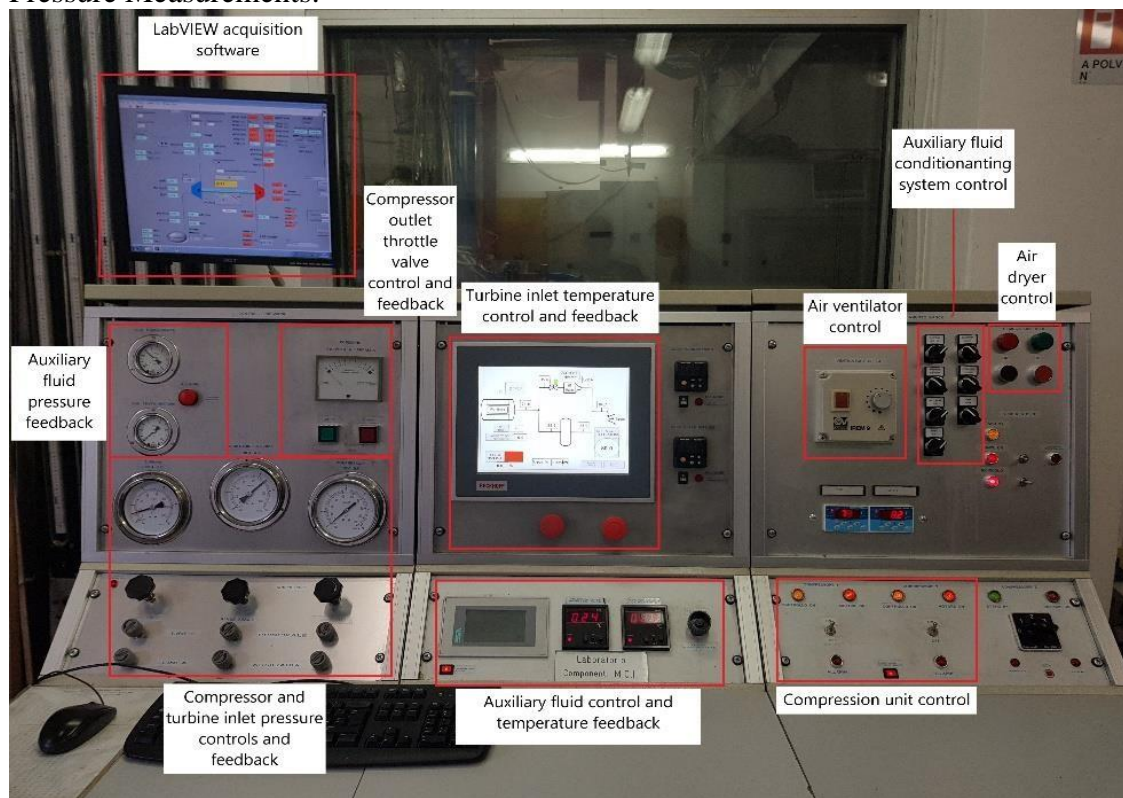

Figure 2.13 – Control console

2.2 Measurement Equipment

Sensors were placed in the test cell to measure the ambient conditions and in specific position along the turbine, compressor and auxiliary fluid circuits. This section describes the location the measuring stations

17

and the instrumentation used for different types of measurements: temperature, pressure, frequency, flow rate, vibration and acoustic measurements.

2.2.1 Measuring Stations

The DIME Internal Combustion Engine component test bench usually utilizes six primary measurement station to monitor the test bench's gas dynamics. Stations 1, 2, and 6 are located along the compressor circuit while Stations 3, 4, and 5 are located along the turbine circuit, shown in Figure. Stations T, C and PG instrument the turbine casing, compressor casing and the pulse generator. Station Ambient is present in the middle of the test cell.

- Station 1 is at the compressor intake,
- Station 2 is at the compressor discharge,
- Station 3 is at the turbine intake,
- Station 4 is at the turbine discharge,
- Station 5 is at the turbine flow rate meter,
- Station 6 is at the compressor flow rate meter,
- Station T is on the turbine casing,
- Station C is on the compressor casing,
- Station LC is along the lubricant fluid circuit,
- Station PG is at the pulse generator,
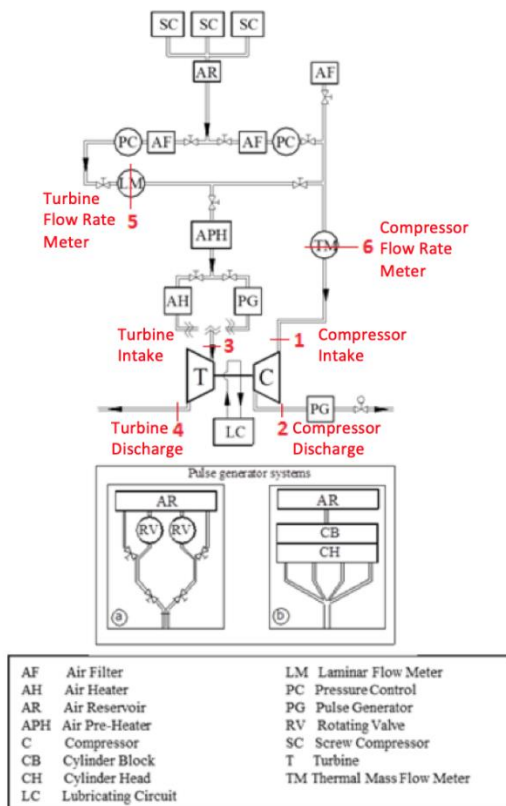- Station Ambient measures ambient conditions in the test cell.

AF	Air Filter	LM	Laminar Flow Meter
AH	Air Heater	PC	Pressure Control
AR	Air Reservoir	PG	Pulse Generator
APH	Air Pre-Heater	RV	Rotating Valve
C	Compressor	SC	Screw Compressor
CB	Cylinder Block	T	Turbine
CH	Cylinder Head	TM	Thermal Mass Flow Meter
LC	Lubricating Circuit		

Figure 2.14 – Location of the six measuring stations in the test bench.

Each measurement station has a set of ports allowing specific measurement equipment to be inserted into the circuit. The type of measurement equipment used at each measurement station is dependent on its location in the working fluid circuit. The specific capabilities of each measuring station are given in Table.

Port Capability	Station 1	Station 2	Station 3	Station 4	Station 5	Station 6	Station T	Station C	Station LC
Resistance Thermometers - Time and Space-Averaged Total Temperature	x	x							x
Thermocouples - Time and Space-Averaged Total Temperature			x	x					
Pressure Transducer on Pressure Ring - Time and Space-Averaged Static Pressure	x	x	x	x					
Instantaneous Pressure Measurement - Local Instantaneous Static Pressure	o	o	o	o					
Two Laminar Flow Meters - Turbine Average Mass Flow Rate					x				
Thermal Mass Flow Meter - Compressor Average Mass Flow Rate						x			
One Hot-Wire Anemometer - Local Instantaneous Mass Flow Rate	o	o	o	o					
Lobe Displacement Meter - Average Lubricant Mass Flow Rate									x
Eddy Current Pick-Up Sensor - Average and Instantaneous Rotational Speed								x	
(x: essential, o: optional)									

Table 2.1 – Description of measurements and sensors in each measuring station

2.2.2 Temperature Measurements

The DIME test bench uses both resistance thermometers and high-temperature thermocouples to monitor the thermal state in several key locations of the working fluid circuit. The resistance thermometers are made of platinum and are type Pt100, with a precision of 0.15 °C ± 0.2 % of the value read on the instrument [33] The thermometer functions based on the principle that a variation in temperature generates a variation of the conductive material's resistivity. These sensors are inserted into the circuit perpendicular to the air flow and deep in the pipe to guarantee that the measurement is not influenced by the pipe temperature.

The turbine feeding line can have significantly higher temperatures than the compressor feeding line and requires high-temperature, k-type, thermocouples. The thermocouples are made of Chromel and Alumel and have a precision of ± 1.5 °C [34]. These thermocouples function based on the Seebeck effect: two conductive resistances made of different materials are connected at both ends and a potential difference

is generated proportional to the temperature difference between the joined ends. An example of the resistance thermometer and the thermocouple are shown in Appendix B.

2.2.3 Pressure Measurements

Two different type of pressure sensors are described in this section: the first are regular pressure sensors, used for the pressure measurements along turbine and compressor circuits; the second is a differential pressure sensor, used to measure the pressure drop in the laminar flow meters described paragraph 2.2.5 Flow Rate Measurements.

2.2.3.1 Average and Instantaneous Pressure Sensors

Twenty-three different pressure sensors are available for tests in the laboratory. This large assortment of sensors allows for a broad spectrum of testing and each sensor can be utilized at a different measurement station to uniquely tailor the data acquisition strategy to the tests being conducted. The characteristics for each sensor are listed in Table. Sensors 7.01 to 7.05 are Gems Sensors 2600 series strain-gage transducers. Each requires an amplification circuit and has a precision of 0.15% of the full scale [35]. Pressure transducer 7.06 to 7.13 are Sensing & Inspection Technologies pre-amplified piezo-resistive sensors with output voltage proportional to the pressure and a precision of 0.1% of the full scale. Sensors 7.01 to 7.13 have a low frequency response and are used for average value pressure measurements during steady flow tests.

Code	Manufacturer	Range	Temperature Range	Accuracy
7.01 to 7.03	Gems Sensors	0÷2.5 bar VG	-54÷120 °C	±0.15% f.s.
7.04 and 7.05	Gems Sensors	0÷4 bar VG	-54÷123 °C	±0.15% f.s.
7.06 and 7.07	Sensing & Inspection Technologies	0÷2.5 bar VG	-20÷80 °C	±0.1% f.s.
7.08 and 7.09	Sensing & Inspection Technologies	0÷4 bar VG	-20÷80 °C	±0.1% f.s.
7.10 to 7.13	Sensing & Inspection Technologies	0÷0.35 bar VG	-20÷80 °C	±0.1% f.s.
7.14 to 7.20	Kulite Semiconductor	0÷4.48 bar G	25÷232 °C	±0.1% f.s.
7.21	Kulite Semiconductor	0÷2 bar A	20÷120 °C	±0.1% f.s.
7.22 and 7.23	Kulite Semiconductor	0÷1.7 bar A	-40÷177 °C	±0.1% f.s.

Table 2.2 – Pressure transducers

The Kulite semiconductor pressure transducers, 7.14 to 7.23, are piezo-resistive pressure transducers characterized by a wide measuring frequency range. These transducers measure pressure with a high frequency response and are used to measure time-variant signals. The transducers are often used in pulsating flow tests and surge detection. It is important to underline that these pressure sensors are accurate up to an operating temperature of 232 °C; meaning that they can operate reliably in the high

temperatures, seen at the compressor outlet. At the turbine inlet, temperatures during high temperature tests can be higher than 232 °C so Kulite semiconductors pressure transducers cannot be used. They are all characterized by a precision of ±0.1 % of the full scale [36] [37] [38]. Additional information on sensors 7.14 to 7.20 can be found in Appendix B.

2.2.3.2 Differential Pressure Transducer

One ABB ASK-800 differential pressure transducer measures the pressure drop in the laminar flow meters used in Measuring Station 5. This sensor is capable of pressure differences up to 60 mbar, which is more than necessary to measure pressure losses in the laminar flow meter [39]. The output is a current signal proportional to the pressure drop.
Two Wika model DPT-10 [40] are adopted to measure the pressure drop in the flanges with calibrated orifice (described in paragraph 2.2.5.2). The maximum static pressure is 160 bar while the measuring range is 500 mbar. The main feature of the *Wika DPT-10* is the high accuracy equal to the 0.75% of the full scale.

2.2.3.3 Pressure Sensor Calibration

The pressure sensors were calibrated by correlating the sensor's output voltage and the pressure at the calibration station with one of the six manometers located in the control room. The relation between pressure and voltage was programmed into a calibration program that validated the relation by comparing it against calibration results obtained in previous tests.

2.2.4 Frequency Measurements

The turbocharger and pulse generator are two components of the test bench whose rotational speed is critical to the behavior of the system. A PICOTURN BM-V6 inductive tachometer is used to measure the speed of the compressor impeller and an inductive encoder is used to measure the frequency of the pulse generator's valve.

2.2.4.1 PICOTURN BM-V6 Turbocharger Tachometer

A PICOTURN BM-V6 inductive tachometer measures the turbocharger's rotational frequency. This sensor can measure very high speeds and provide the instantaneous value with high precision (0.5% of the full scale [41]). PICOTURN's BM-V6 is composed of a dedicated signal conditioner and an eddy current pickup sensor, shown in Figure2.15. The eddy current pickup sensor faces the compressor impeller and records inductance changes caused by blades passing. The signal conditioner converts the pickup sensor's pulse signal into the turbocharger rotational speed using the number of compressor blades.

Figure 2.15 – PICOTURN BM-V6 system

2.2.4.2 Pulse Generator Valve Inductive Encoders

Inductive pickups are used to measure the rotational frequency of the rotating valves of the pulse generator. These pickups are composed of coils wrapped around a permanent magnet that face a ferromagnetic phonic wheel. The phonic wheel is connected to the valve shaft and the teeth movement varies the electromagnetic field which is measured by the inductive pickup and correlated to the valve's rotational frequency.

2.2.5 Flow Rate Measurements

Two laminar flow meters, one thermal mass flow meter and two hot film anemometers measure air mass flow rate in different measurement stations along the circuit. A lobe displacement meter measures the lubricant mass flow rate.

2.2.5.1 Cussons Technology Laminar Flow Meters

The two laminar flow meters (shown in Figure 2.16), Cussons Technology P7205 and P7209, measure the air mass flow rate in the turbine intake circuit. The P7205 sensor can measure values up to 100 l/s, while the P7209 can measure values up to 200 l/s [30]. They can be used simultaneously if the flow rate requested by the turbine is higher than 200 l/s.

Figure 2.16 – Laminar flow meters, P7205 (left) and P7209 (right)

An internal matrix straightens the flow to guarantee laminar flow conditions. A differential pressure sensor estimates the flow rate from the pressure loss, see Figig. 2.17 for a cross section of the device. When the flow is laminar, the pressure drop across the instrument is proportional to the average volumetric flow rate. Equation 2.1 provides the relation between the flow's speed and the volumetric flow rate:

$$Q = C \cdot \Delta p \cdot FT$$

<div align="right">(2.1)</div>

Where:
- Q is the volumetric flow rate,
- C is the slope of calibration line,
- Δp is the pressure drop,
- FT is the corrective coefficient that take into account viscosity variations with temperature.

Temperature and pressure measurements downstream the sensor allow the calculation of the density, which is multiplied to the volumetric flow rate to obtain the mass flow rate.
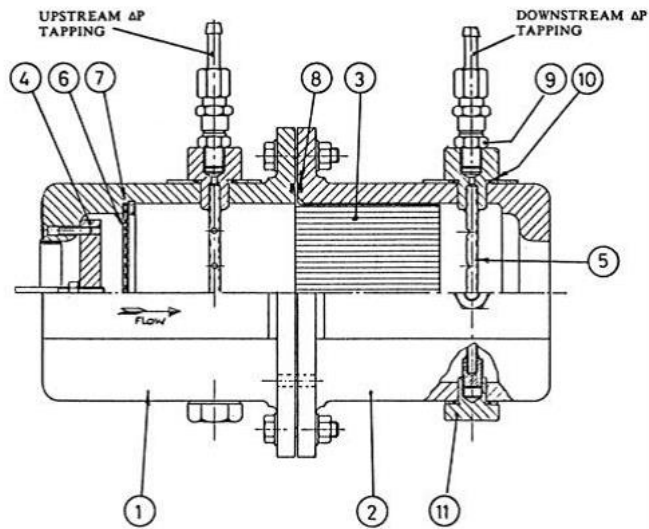
Figure 2.17 – Laminar flow meter

Moreover, by consulting Figure 2.18 and Figure 2.19 it is possible to see the calibration curves of both the laminar flow meters and the effects of p_5.
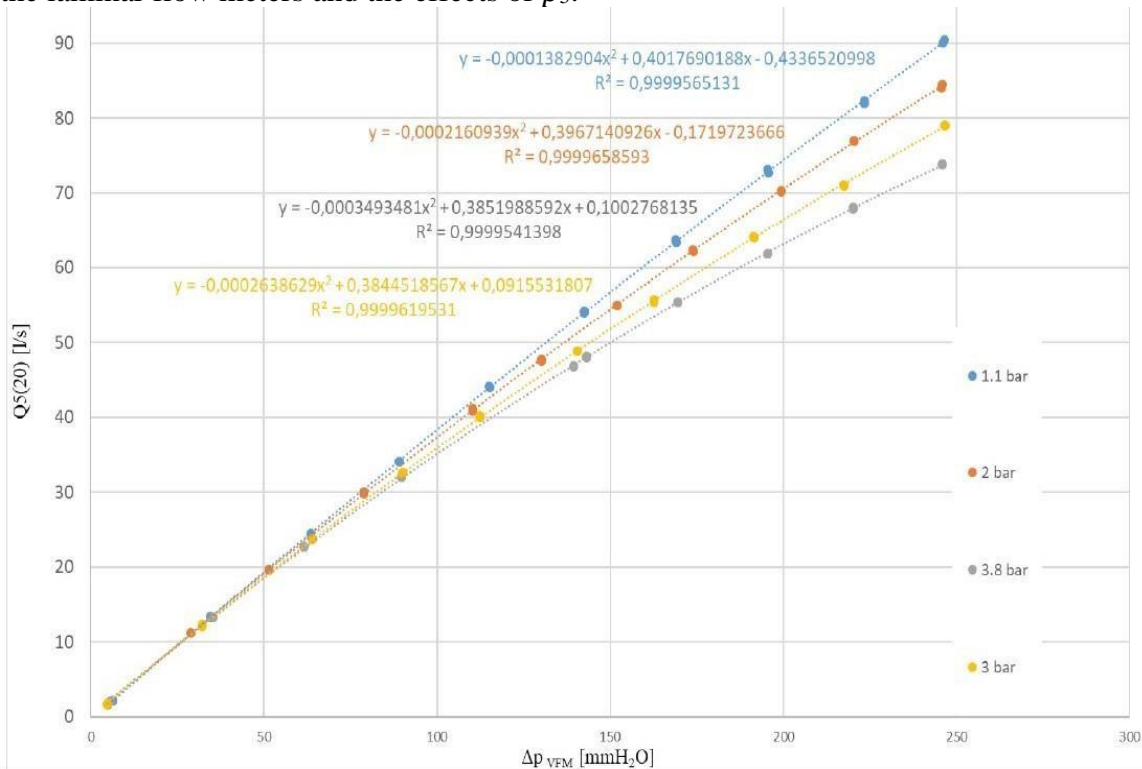
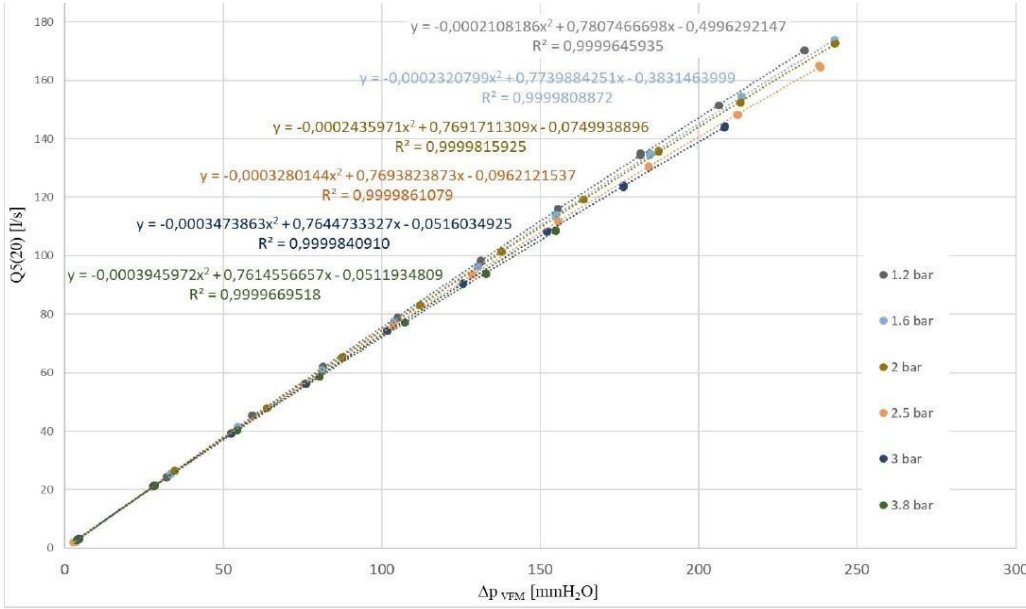

Figure 2.18-Calibration curves of laminar flow meter P7205

Figure 2.19-Calibration curves of laminar flow meter P7209

2.2.5.2 Flanges with Calibrated Orifice

Two flanges with a calibrated orifice *(*Wika, model FLC-FL [42]) are installed to measure the air mass flow rate in each turbine sector. Using diaphragms is a common solution because of their quite simple installation, versatility, and reliability. In this case is used a sharp-edged diaphragm suitable for general application on fluid and gasses. The hole diameter is dimensioned by the constructor to generate a specific differential pressure referred to the full-scale measure. The scheme reporting the main geometrical data of the flanges with calibrated orifice is reported in Appedix B.

The differential pressure generated by the orifice is proportional to the air mass flow rate, as showed in (2.2) equation, and using a differential pressure transmitter it's possible to obtain an electric measurement signal.

$$q_m = \frac{C}{\sqrt{1 - \beta^4}} \varepsilon \frac{\pi}{4} d^2 \sqrt{2\Delta p \rho_1} \tag{2.2}$$

where:

- *C* is the *Discharge Coefficient* provided by the Reader-Harris/Gallagher equation [43]. C is a function of geometry and flow properties.

   Geometry influence involves: β, the distance l_1 between the upstream pressure tap and the up face of the orifice and the distance l_2 between the down face of the orifice and the downstream pressure tap (25.4 mm), divided by the duct internal diameter (52.48 mm). About the flow, the main important coefficient is the Reynold number, but it is a function of q_m, and required an iteration procedure to determine the value;

- β is the *Diameter Ratio*

- ε is the *Expansibility or Expansion Factor*. It is calculated from the empirical equation (eq. 2.3) explained in [44]:

$$\varepsilon = 1 - (0.351 + 0.256\beta^4 + 0.93\beta^8)\left[1 - \left(\frac{p_2}{p_1}\right)^{\frac{1}{k}}\right]$$

<div align="right">(2.3)</div>

- d is the diameter of the calibrated orifice;
- Δp is the differential pressure on the diaphragm;
- ρ_1 is the fluid density calculated with the law of ideal gasses (eq. 2.4).
  p is the pressure measured with the upstream tap.
  The temperature, under the hypothesis of adiabatic flow, is measured five diameters downstream the orifice with a thermocouple. In fact, in this way, the flow is not influenced by the presence of the transductor while the five diameters distance is needed to obtain a uniform air flow.

$$p = \rho RT$$

<div align="right">(2.4)</div>

2.2.5.3 ABB Thermal Mass Flow Meter

An ABB Sensyflow FTM500-IG thermal mass flow meter, shown in Fig. 2.20, measures the average compressor mass flow rate. This sensor is denoted as TMFM in the compressor feeding line. This sensor is less invasive than the laminar flow meter because it does not occupy the whole area of the pipe; the only intrusive part is the sensor and its support. Since the accuracy of the measurement increases when the flow is fully developed, a flow rectifier (Zanker plate) was placed upstream the sensor. The sensor probe is made of platinum elements which allows a higher reliability and mechanical resistance than a hot film anemometer but reduces the sensor frequency response. For this reason, the thermal mass flow meter is only used for steady flow measurements. This device can measure an air flow rate up to 3200 kg/h and is characterized by an error of ±0.9 % of the measured value plus ±0.5 % of the full scale [45] An image of the ABB Sensyflow sensor is provided in Appendix B.

Figure 2.20– ABB Sensyflow FTM500-IG installed on testing line

2.2.5.4 Flomec Lobe Displacement Meter

The Flomec OM006A lobe displacement meter used in the Lubrication Circuit uses the Hall Effect to measure the lubricant flow rate. The full scale of the sensor is 100 l/h and its accuracy is ±1 % of the full scale [46].

2.2.5.5 Dantec Dynamics Hot Film Anemometers

Several Dantec Dynamics hot film anemometers are used to measure instantaneous air flow rates. The sensor Dantec Dynamics model 55R04 is made of nickel which provides a valuable compromise on diameter while providing good mechanical resistance and maintaining a high frequency response [47]. This device requires a Dantec Dynamics Mini CTA 54T30 conditioner, shown with the anemometer in Figure 2.2.21, to maintain the anemometer's film at a constant temperature [48]. The anemometer's film is an electric resistance and dissipates heat according to the Joule Effect while exchanging heat with the fluid. Because the current required to maintain a constant film temperature is proportional to the thermal power exchanged with the fluid and this exchange is proportional to the flow's speed, the conditioner can estimate the volumetric flow rate at the measuring station.
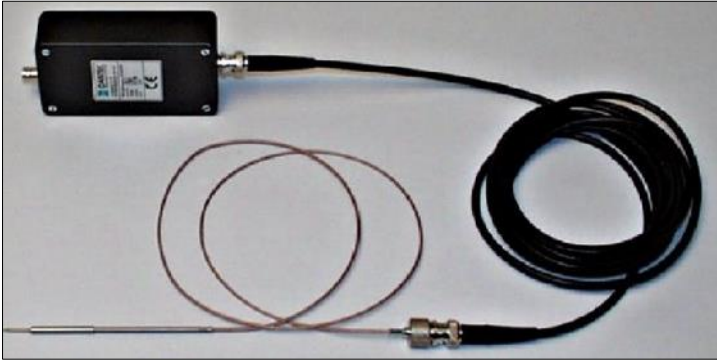
Figure 2.21 – Hot film anemometer and conditioner

The anemometers were positioned in the center of the pipe with the sensor probe perpendicular to the oncoming flow. The sensors were kept in the same position for both tests and calibration, but the pipe containing the measuring station was connected to the hot air turbine line during calibration. This set-up allowed calibration at a broader range of temperatures. The temperature ranges were determined for each anemometer based on the results of the expected flow temperature.
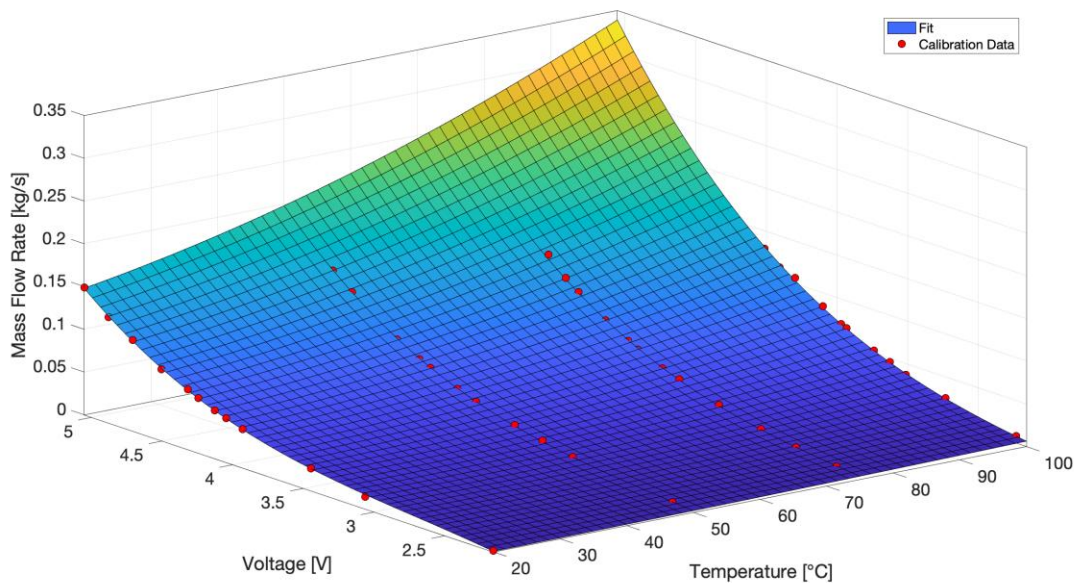

Figure 2.22 – Example of anemometer calibration curve

2.2.6 Vibration Measurements

The experimental investigation used two types of accelerometers as each captured a different frequency range. The accelerometers were installed on turbocharger casing with a two-component adhesive which guaranteed adhesion at both high and low temperatures. The PCB model 352C33 accelerometer is a larger accelerometer which measures low frequency vibrations (2.5 to 10000 Hz) [49]. The other accelerometer, a Brüel & Kjær type 4393, can capture high frequency vibrations (higher than 10 kHz) [50]. The characteristics of both accelerometers are shown in Table. Images of the accelerometers are provided in Appendix B.

	PCB Model 352C33	Brüel & Kjær type 4393
Sensitivity	10.2 (±10%) mV/(m/s²)	0.316 (±2%) pC/(m/s^2)
Frequency Range	2.5 to 10000 (±5%) Hz	0.1 to 27000 (±10%) Hz
Resonance Frequency	>50 kHz	>55 kHz
Weight	5.8 g	2.4 g

Table 2.3 – Accelerometer characteristics

2.2.7 Acoustic Measurements

Two different microphones were used during the experimental activity; a G.R.A.S. 40AE 1/2" pre-polarized free field [51] was located near the compressor casing, and a pre-amplified G.R.A.S. 26CA 1/2" CCP standard [52] was located at the pipe inlet by the filter inlet section. The microphones' characteristics are given in Table 2.. Images of the microphones are provided in Appendix A.

	G.R.A.S. 40AE 1/2"	G.R.A.S. 26CA 1/2" CCP
Frequency Range	3.15 to 20000	2.5 to 200000 Hz
Noise	-	1.8 μV
Sensitivity	50 mV/Pa	-0.30 dB
Dynamic range	15 to 148 dB(A)	-

Table 2.4 – Microphones characteristics

2.3 Acquisition System

All transducers electrical lines connect to a rack in testing room. Here, the different signals connect to selected devices to be converted from analog to digital and then recorded by the acquisition system. The acquisition system is segregated into an instantaneous and a time-averaged structure, shown in Fig. 2.. In this structure, all signals used for time-averaged measurements transmit to an Agilent data acquisition unit and are recorded by PC1; in parallel, all signals used for instantaneous measurements transmit to one of two National instruments PCI acquisition cards and are recorded by PC2.
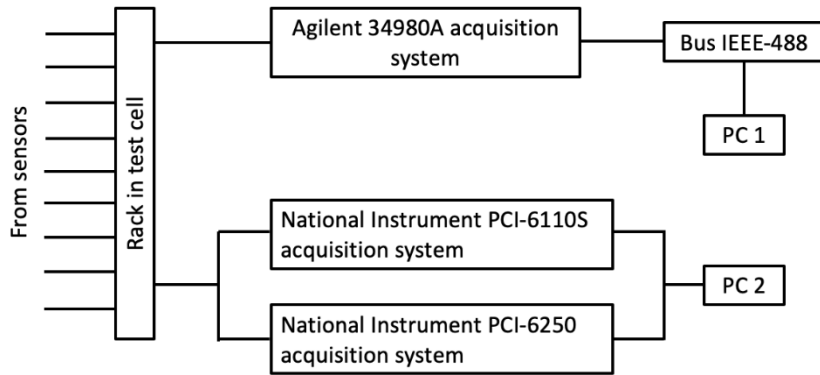
Fig. 2.23 – Data acquisition structure

The signal management rack simplifies the connection of different sensors to the two acquisition systems and reduces the complexity of electrical connections between to the acquisition systems. This solution also allows different components to be centralized and connects the test cell to the control room with a reduced number of electric cables. The main components in the rack include the:

- junction box which connects the power supply and acquisition circuits to the Agilent A34980A,

- terminal board which connects the sensors to the high sampling frequency National Instruments acquisition systems, and

- stabilized 24V DC power supply.

Given the need to connect different types of sensors, the terminals in the junction box have been reorganized to directly connect the sensors used during tests. The rack has a capacity of:

- 12 BNC connections,

- 14 thermocouple connections,

- 12 current connections, characterized by a three-cable plug,

- 96 additional three cable plugs used for alternative sensors.

The Agilent A34980A acquisition system collects, handles and post-processes all time-averaged data [53]. The Agilent system can collect signals through a total of 132 channels, of which, 12 are specifically dedicated to current measurements and communicates with the computer PC1 through an ethernet connection. On PC1 LabVIEW TURBO program allows the test operator to set test parameters, visualize and import variables, and start and end the data acquisition from one centralized console; the front panel of this program is shown in Figure 2.24. A picture of the acquisition system and a detailed description of the program TURBO is provided in Appendix A.

The two dedicated National Instruments acquisition systems, NI PCI-6110S and NI PCI-6250, collect dynamic measurements and are located in PC2. The PCI-6110S system can collect measurements in 4 channels with a resolution of 12 bits and a sampling frequency up to 5 MHz for each channel [54]. The PCI-6250 can collect data on 16 channels with a resolution of 16 bits and a sampling frequency up to 1.25 MHz for a single channel acquisition and up to 1 MHz for a multiple channel acquisition [55]. A LabVIEW software on PC2 allows the test operator to set the number of channels, the sampling frequency and the acquisition length for all instantaneous signals. PC2 also synchronizes the acquisition of sensors connected to the two different NI PCI acquisition systems.
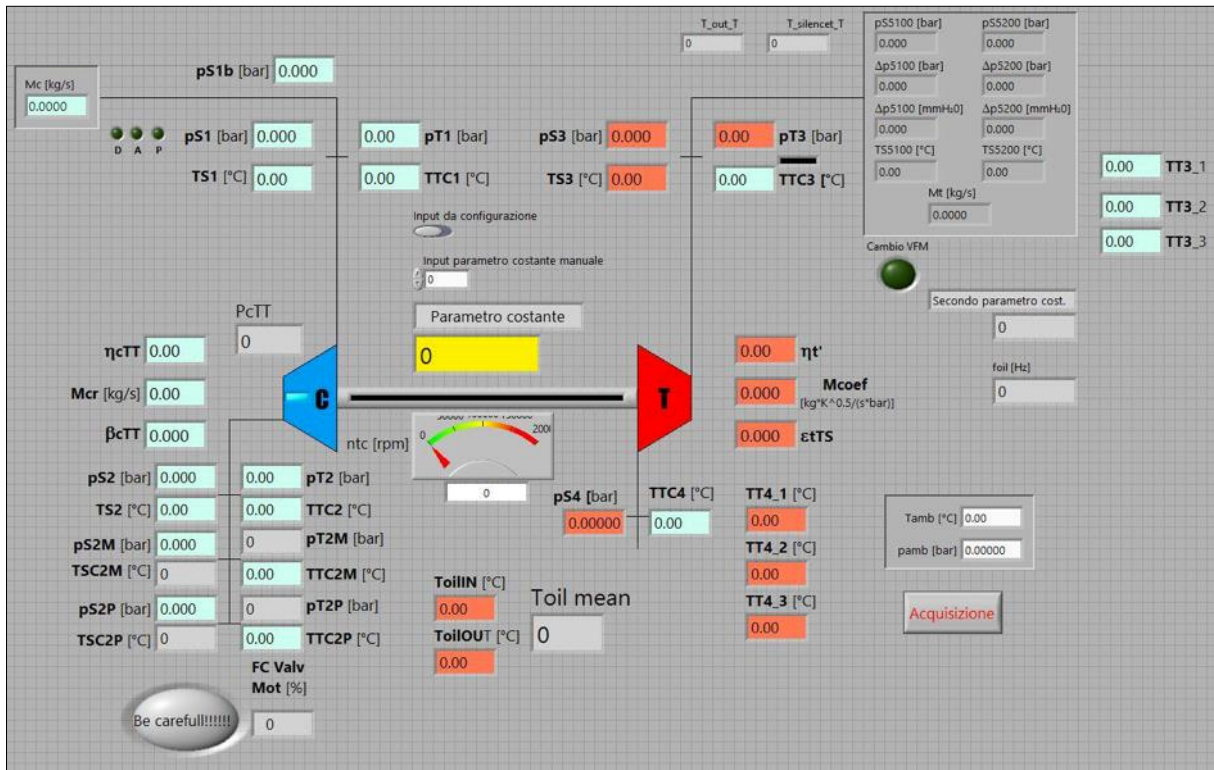
Figure 2.23 – TURBO.vi front panel

2.4 Electric Supply System

In order to supply with the correct voltage, the e-compressor a battery emulator by AVL was adopted. The voltage output of the emulator goes from 0 to 60 V, which are the most common value required by modern mild hybrid vehicles.

2.4.1 AVL E-STORAGE LV

The AVL E-STORAGE LV (Fig. 2.25) is a low voltage version of the E_STORAGE products developed for the characterization of electric component in automotive industry [56]. The system is based on a CC regenerative power supply easy to use on test bench application.

Figure 2.25 – AVL E-STORAGE LV

2.4.1.1 Feeding mode and regenerative mode.

The battery emulator present two working mode called Q1 e Q4:

- In Q1, the feeding mode (fig. 2.26) the battery emulator presents positive value of current and voltage. The Q1 mode is characterized by positive value of current: the current is provided by the e-storage to the load. The working conditions are delimited by the nominal voltage, the nominal current and the maximum power.
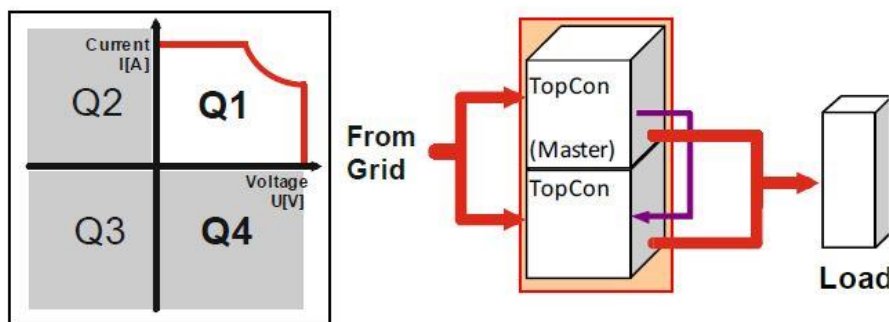
Fig. 2.26 – Q1 mode scheme

- In Q4 the regenerative mode (fig. 2.27) the battery emulator presents positive value of current and negative value of voltage.

The Q4 mode is characterized by negative value of current: the current is generated by the load to the e-storage. The working condition in this mode are characterized by the nominal voltage, the nominal negative current and the negative maximum power.
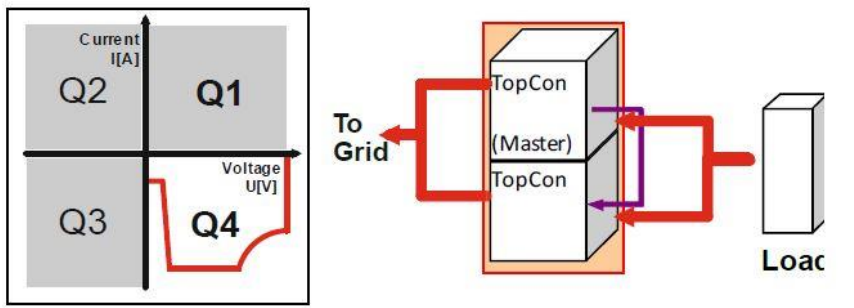
Fig. 2.27 – Q4 mode scheme

The possibility of having two operating modes, feeding mode and regenerative allows to the e-storage to be versatile. In automotive application the e-storage can replicate realistically all the behavior of a battery stack equipped on low voltage mild hybrid vehicles.

4.1.1.2 Battery emulator settings

Through the control software TopControl (in fig. 2.28 the user interface), provided with the battery emulator, all the output parameters are set:

- Output voltage equal to 12.7V, in order to replay the typical condition occurring on vehicles;
- Maximum current equal to 200 A, the limit admitted by the e-compressor;
- Minimum current equal to 0 A in order to avoid negative value of current during slowdown transients, situation not compatible with the correct operation of the e-compressor.

Figure 2.28 – Top Control user interface

3. Experimental Activity

As a first step, the steady-state performance of each component was measured test rig for components of propulsion system of the University of Genoa test rig. Subsequently another experimental campaign was carried out to evaluate the transient response of the entire turbocharging system. Two different layouts were compared: upstream and downstream. In the upstream configuration the electrically assisted compressor was placed in front of the traditional turbocharger, in the downstream configuration the e-compressor was positioned after the traditional turbocharger.

3.1 e-Compressor Steady State Characterization

The e-compressor (eSC) is a radial centrifugal compressor driven by a switched reluctance motor (SRM) which is designed to deliver an instant boost pressure to reduce the response time and therefore enhance the system performance.
The component is usually operated by the ECU which sends a signal that imposes the rotational speed setpoint.

Figure 3.1 – e-Compressor CAD model

The e-compressor is composed of various aerodynamical, mechanical and electrical subsystems, assembled in one component. In particular, the components are listed below:
- radial centrifugal compressor;
- high-speed electrical motor;
- electronic control system;
- power and control electrical connections;
- integrated thermocouples.

The impeller is made of a lightweight aluminum alloy in order to reduce the inertia momentum as possible, gaining advantages in terms of acceleration. The volute, also composed of the same aluminum alloy, is refrigerated with an internal circuit by means of two ducts placed on the top (Figure 3.1). In Figure 3.2 an image of e-compressor impeller and volute is shown.

Figure 3.2 – e-Compressor impeller, volute and shaft

The electrical motor is a variable reluctance (SR) type. The constructor chose this typology because of the typical easiness and reliability given by the absence of rotor windings or permanent magnets. Due to the reduced inertia momentum and the presence of low-friction bearings, the motor reaches a maximum acceleration of 400.000 rpm/s^2. This type of motor allows also to carry the compressor rotational speed up to 70000 rpm.

3.1.1. Experimental Set-up

The steady state compressor map was measured using a specific layout designed to drive the compressor wheel with a turbine and avoid over-temperature issues. Actually, the operational time of the e-compressor is limited due to the working temperature of the bearings and of the electrical components. With the aim to measure compressor performance with good accuracy, a specific driving system was designed, consisting in a turbocharger turbine adopted instead of the electric machine, according to the requested power levels (Figure 3.3). As a matter of the fact, the correct definition of compressor efficiency starting from the measurement of the upstream and downstream temperatures takes a long time for the stabilization of the system not compatible with restrictions imposed by the electrical components.

Figure 3.3 – Turbocharger turbine selected as the e-compressor driving system

In Figure 3.4, the connection between the compressor and the turbine is shown. Particular attention was paid to the bearings located on the compressor shaft; a low axial load was adopted together with a spring to guarantee good operation. The junction between the turbine and the compressor shafts was realized guaranteeing a small radial clearance, and the whole assembly was coupled through a specific casing inserted between each volute.
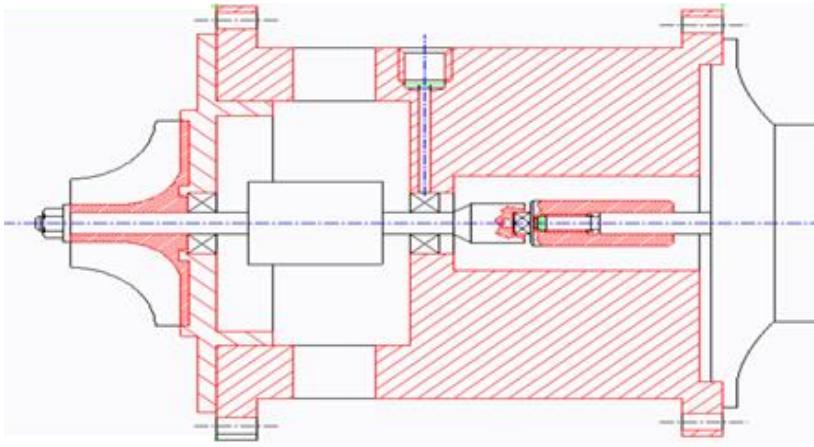

Figure 3.4 – Details of the e-compressor driving system

The assembled system, visible in figure 3.5, was then balanced before starting the experimental investigation.
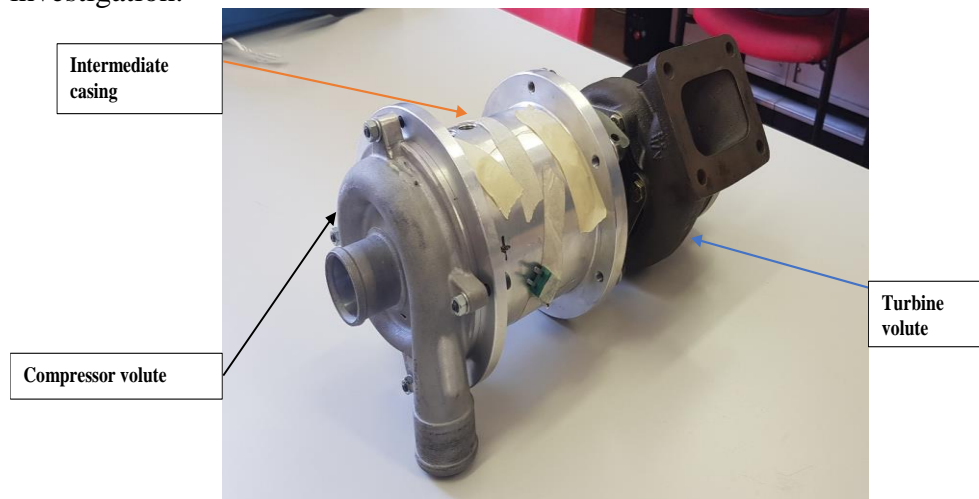
Figure 3.5 – Assembled prototype

To avoid over temperature issues, dry air at ambient temperature was provided in the central casing. Moreover, the bearing temperature was monitored through two thermocouples inserted in.
The compressor and the relevant connecting pipes were properly insulated to avoid inaccuracies in the evaluation of the compressor isentropic efficiency. The outlet temperature of the compressor could be measured in an unrealistic way reflecting the impact of the heat transfer of the ambient and of the hot side of the turbocharger [57]. Actually, the adiabatic assumption cannot be used for small turbomachines, especially at low speeds and low loads [58]. This effect leads to an incorrect evaluation of compressor efficiency, generally underestimated at lower rotational speed.

During the experimental campaign, vibro-acoustic measurements were performed to check the good structural behavior of the prototype and to better identify and define the surge occurrence.

To this aim, mono and three axial accelerometers are mounted on the compressor and turbine housing, and on the intermediate casing (Figure 3.6). Due to the dynamic response of the probes, it was possible to capture frequencies up to the compressor Blade Passing Frequency (BPF). Besides, acoustic measurements were carried out with pre-polarized microphones with range between 2 and 50 kHz of dynamic response. The sensors were located close to the compressor housing and to the intermediate casing (where the bearings are located).
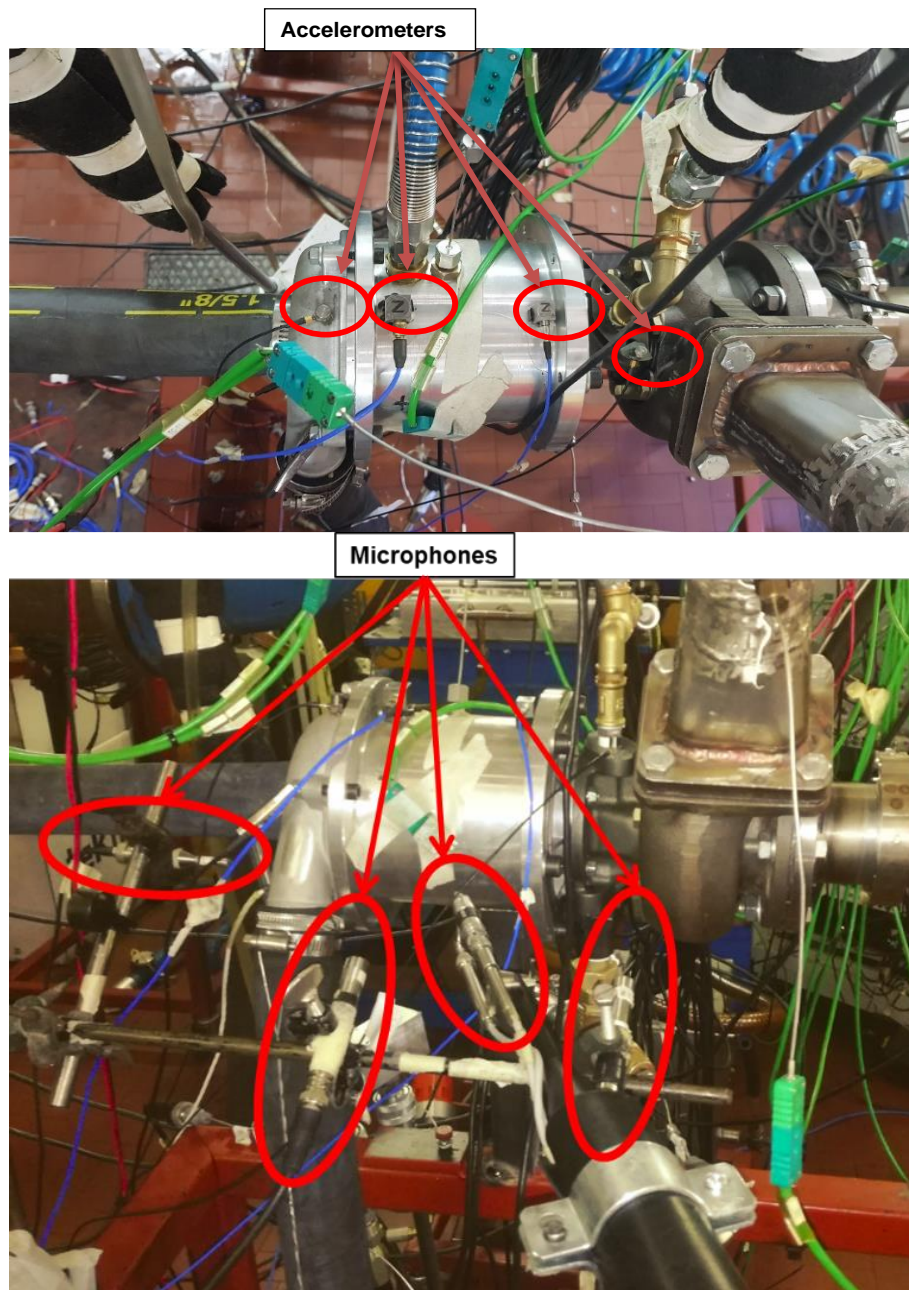
Figure 3.6 – Detail of the accelerometers and microphones installation

During the monitoring phase, attention was paid on the prototype connection between compressor and turbine shafts. To diagnostic purpose, the vibration and noise response of the system was monitored. Figure 3.7 shows time-frequency analysis through a color-map of accelerometer signal, measured on the compressor casing. The horizontal (x) and vertical (y) axis represent the frequency content and the rotational speed, respectively. The amplitude is related with the color intensity with reference to the color-bar. In figure 3.7 some harmonic components could be identify: not integer super-synchronous component (2.66X) related to ball bearings, high frequency contribution related to compressor blade passage (8X and 16X) and turbine blade passage (11X and 22X); moreover, some sub-synchronous and synchronous components probably related to structural resonance could be observed.
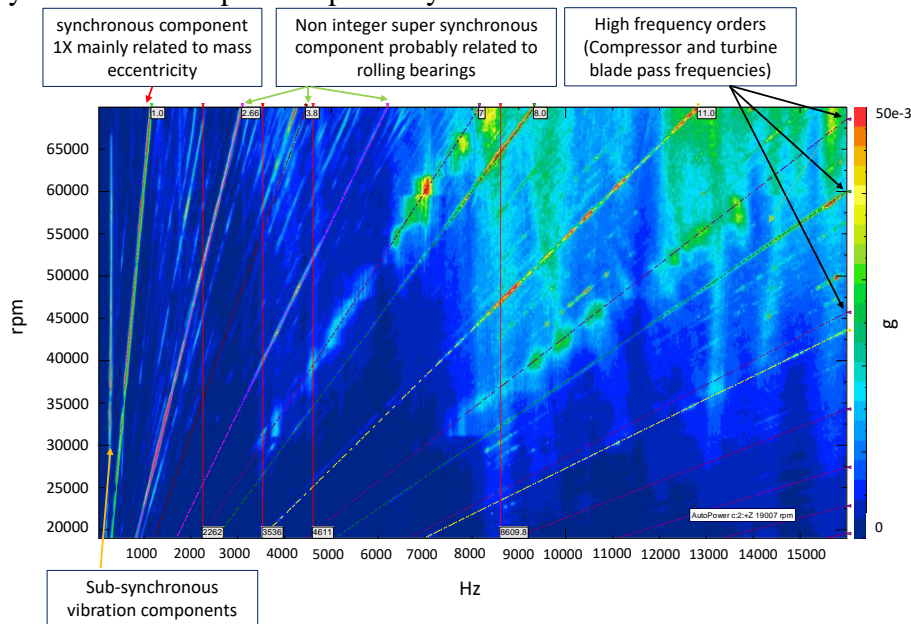
Figure 3.7 – Time frequency analysis at the compressor housing of the accelerometer

Moreover, a fixed frequency component (2200 Hz) raises for higher rotational speed than 30000 rpm, when the 3.8X component related to the e-compressor bearings reaches this frequency value (green box in Figure 3.8). This phenomenon could be associated to a structural resonance of the system.
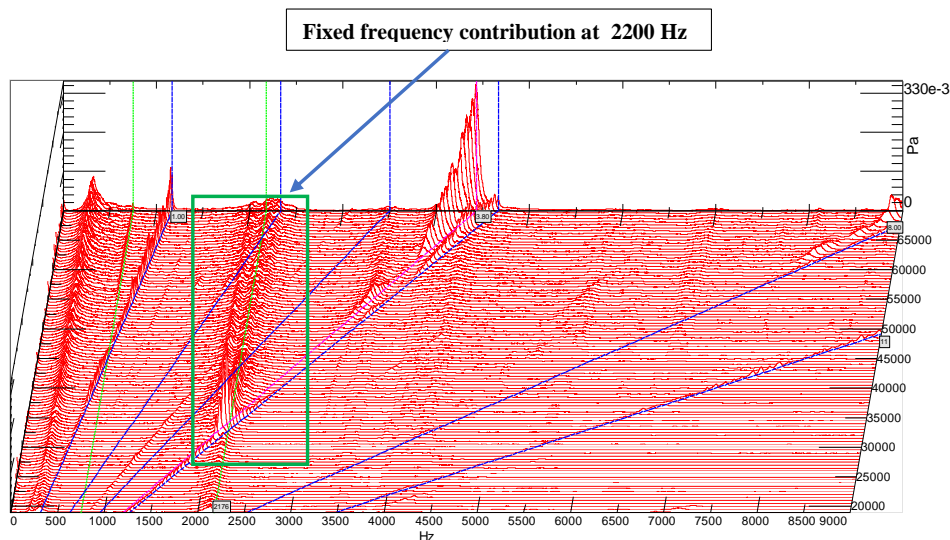

Figure 3.8 – Waterfall of microphone near the compressor housing evaluated during run up

36

Different run-up measurements were performed at the beginning (magenta line in figure 3.9), in the middle (blue line) and at the end (red and green lines) of the experimental campaign. A good system behaviour can be observed in Figure 3.9 with reference to the microphone and accelerometer signals. A comparison of the RMS (Root Mean Square) levels in the frequency band 3-5000Hz is reported, highlighting a similar trend during the whole experimental investigation due to a not damaged system.
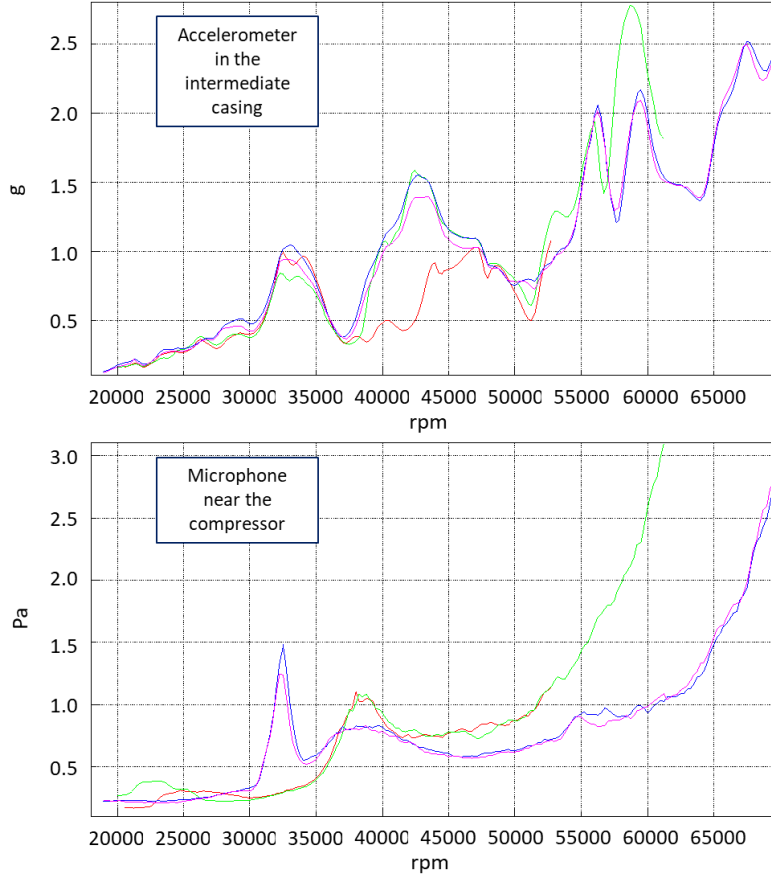

Figure 3.9 – Comparison of RMS levels (3-5000Hz) of different signals used for the diagnostic analysis

3.1.2 e-Compressor Steady Flow Performance

Compressor steady flow characteristic curves were measured referring to the following parameters:

- Corrected rotational speed: n_{cr} [rpm]

$$n_{cr} = \frac{n\sqrt{T_0}}{\sqrt{T_{T1}}} \tag{3.1}$$

where:
n is the turbocharger rotational speed;
T_0 is the reference condition equal to 293.15 K;
T_{T1} is the compressor inlet total temperature.

- Total-to-total compression ratio: β_{cTT} [-]

$$\beta_{cTT} = \frac{p_{T2}}{p_{T1}} \tag{3.2}$$

where:
p_{T2} is the compressor outlet total pressure;
p_{T1} is the compressor inlet total pressure.

- Corrected mass flow rate: M_{cr} [kg/s]

$$M_{cr} = \frac{M_c p_0 \sqrt{T_{T1}}}{p_{T1} \sqrt{T_0}} \tag{3.3}$$

where:
p_0 is the reference condition equal to 0.981 bar;
M_c is the compressor mass flow rate.

- Total-to-total isentropic efficiency: η_{cTT} [-]

$$\eta_{cTT} = \frac{T_{T2is} - T_{T1}}{T_{T2} - T_{T1}} \tag{3.4}$$

where:
T_{T2} is the compressor outlet total temperature;
T_{T2is} is the compressor outlet total temperature for an isentropic compression.

The steady state compressor performance curves (Figures 3.10 and 3.11) are measured from the choking zone to the surge line changing the external circuit characteristic through a motorized throttle valve located downstream of the compressor, and properly controlling the turbine power.
Performance maps were measured for the following levels of compressor corrected rotational speed: n_{cr} = 20000, 30000, 40000, 50000, 55000, 60000, 65000 and 70000 rpm.
Each iso-speed line was explored considering a minimum of 6 different measuring points. Several measurements were performed in each operating condition, with multiple data acquisition (10 cycles) for each measurement.
Tests were performed in cold condition with a turbine inlet temperature equal to 50 °C in order to avoid condensation and freezing problems during expansion and to limit an extreme thermal stress to the bearings of the e-compressor.
In Figure 3.10, the steady state compressor characteristic curves are reported with reference to the total-to-total pressure ratio plotted versus the corrected mass flow rate.
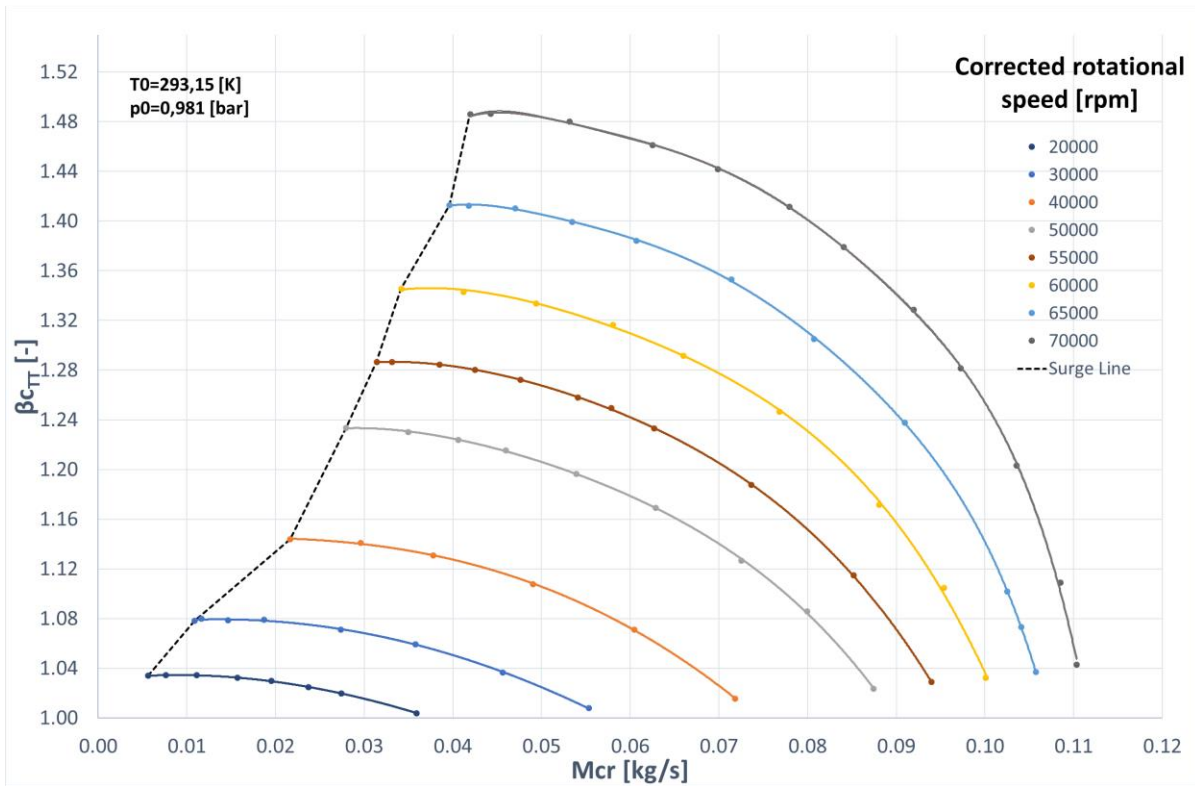
Figure 3.10 – e-Compressor total-to-total pressure ratio map

In Figure 3.11, the total-to-total isentropic efficiency plotted versus the corrected mass flow rate is shown for different values of corrected compressor rotational speed. It can be observed that the impact of the heat transfer appears to be less important at higher rotational speed since the heat power transferred to the gas decreases with respect to the increase of mechanical power. Measurements show that at fixed mass flow the heat power decreases with the revolution speed because of the complex heat balance of the whole turbocharger group, which includes the contribution of the air, of the lubricating oil and of the heat transfer to the environment.
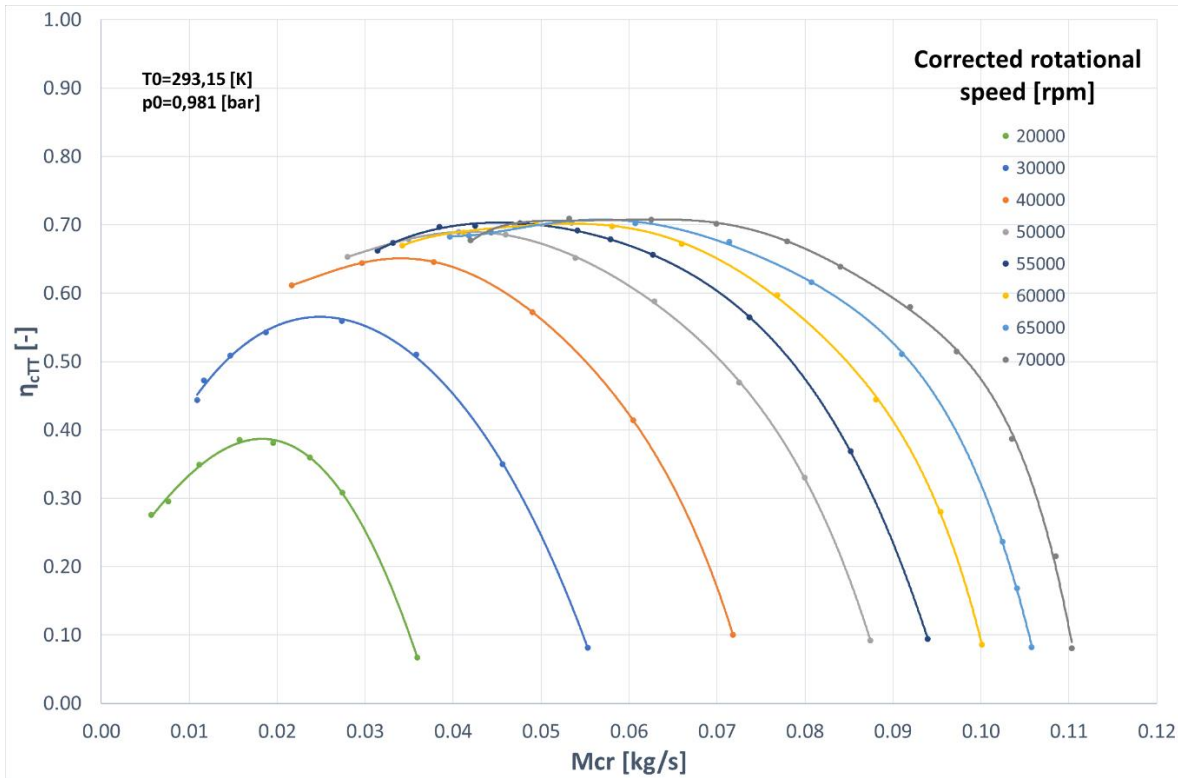
Figure 3.11 – e-Compressor total-to-total isentropic efficiency map

The surge line was detected through a high frequency response pressure transducer. As an example, in Figure 3.12 the surge occurrence is highlighted referring to the outlet pressure (in green, minus the mean value) and rotational speed (in red) signals in the upper figure. Monitoring the time based signal of pressure, it was possible to state the instant when it turned from the almost flat stable condition shape to a clearly sinusoidal wave, typical of the surge condition. The slight increase of pressure and rotational speed that can be observed is due to the reduction of the compressor power when surge onset. The definition of the surge condition could be defined more clearly in the time-frequency domain shown in the figure below, where the beginning of the surge occurrence is highlighted in green with reference to pressure signal.
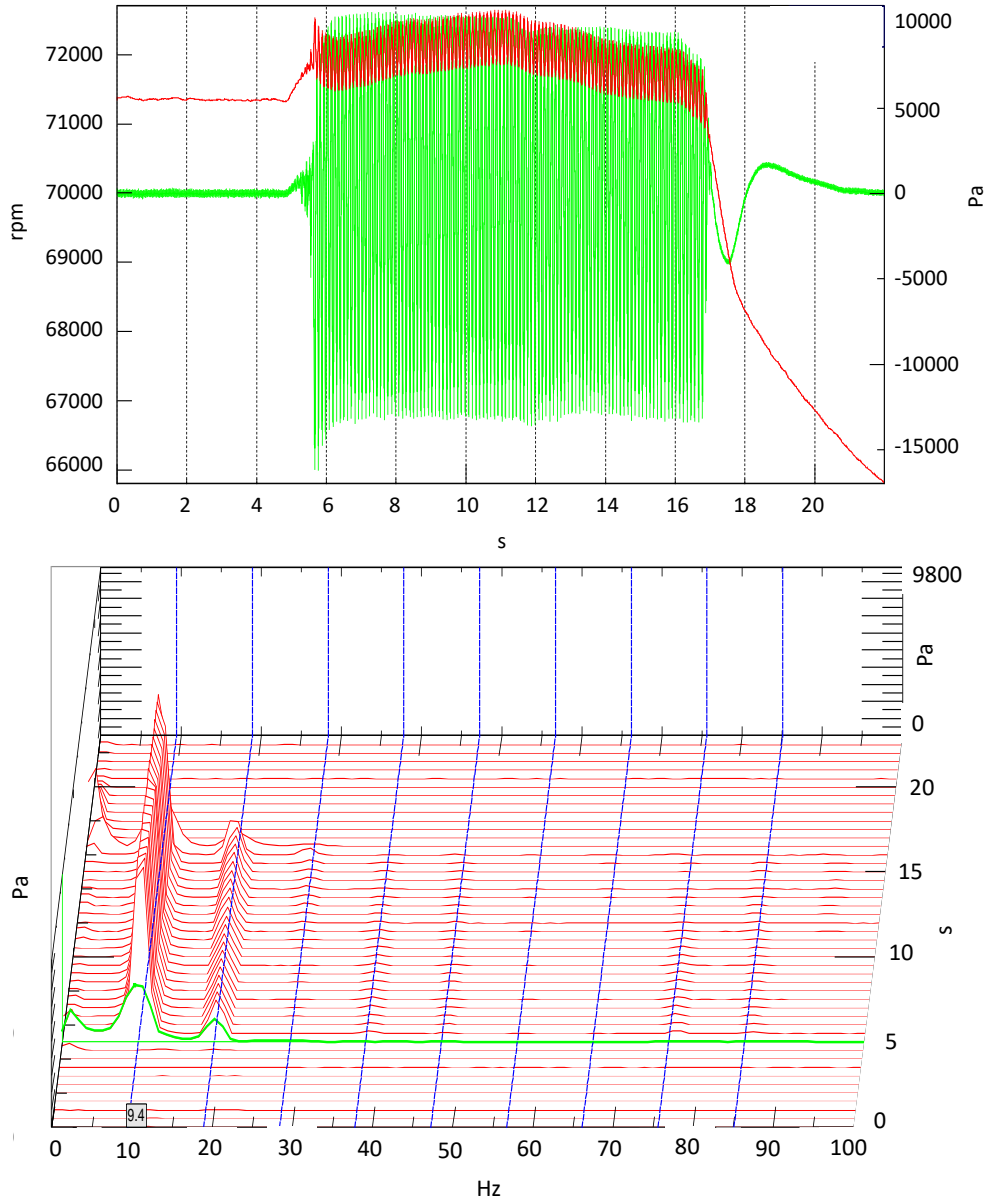
Figure 3.12 – Rotational speed (red) and compressor outlet pressure (green) signals in time domain (on the top) and time-frequency domain analysis of the pressure signal (on the bottom)

3.2 Main Turbocharger Steady State Characterization

The installed component is a small-sized turbocharger, characterized by a reduced inertia momentum (Figure 3.13).

It is constituted by a radial centripetal turbine mechanically fitted to a radial centrifugal compressor. A waste-gate valve is installed close to the turbine volute inlet to work as regulation system. The mass flow evolving through the turbine is modulated by operating the waste-gate position and consequently also the turbine power output is controlled.

Figure 3.13 – Borg Warner turbocharger

3.2.1 Turbine Steady Flow Performance

In following equations are described parameters according to the Mach similarity theory that guarantee comparison between the turbocharger performance in different test conditions.

- Speed parameter N_t [rpm/$\sqrt{K}$]:

$$N_T = \frac{n}{\sqrt{T_{T3}}}$$

(3.5)

where:

T_{T3} is the total temperature at the turbine inlet.

- Total-to-static expansion ratio ε_{tTS} [-]:

$$\varepsilon_{tTS} = \frac{p_{T3}}{p_{s4}}$$

(3.6)

Where:

p_{T3} is the turbine total inlet pressure;
p_{s4} is the static pressure at the outlet of the turbomachine.

- Mass Flow Parameter MFP [kg $\sqrt{K}$/ (s bar)]:

$$MFP = \frac{M_{t3} \cdot \sqrt{T_{T3}}}{p_{T3}}$$ (3.7)

where M_{t3} is the total air mass flow rate.

As regard the turbine efficiency is introduced the thermomechanical efficiency (η'_t), defined in equation 3.8 as the product between the turbine total-to-static isentropic efficiency and the turbocharger mechanical efficiency. However, because of the issue related to the measurement of the temperature at the turbine outlet due to the flow structure, is consolidated the use of the thermomechanical efficiency based on the turbocharger power balance exploiting compressor power, thermodynamically evaluated with good accuracy [59].

$$\eta'_t = \eta_{tTS} \cdot \eta_m = \frac{P_{cTT}}{P_{tTS,iso}} = \frac{M_c \cdot c_{pc} \cdot (T_{T2} - T_{T1})}{M_{t3} \cdot c_{pt} \cdot T_{T3}\left(1 - \left(\frac{p_{s4}}{p_{T3}}\right)^{\frac{k-1}{k}}\right)}$$ (3.8)

Where:

P_{cTT} is the compressor total-to-total power;
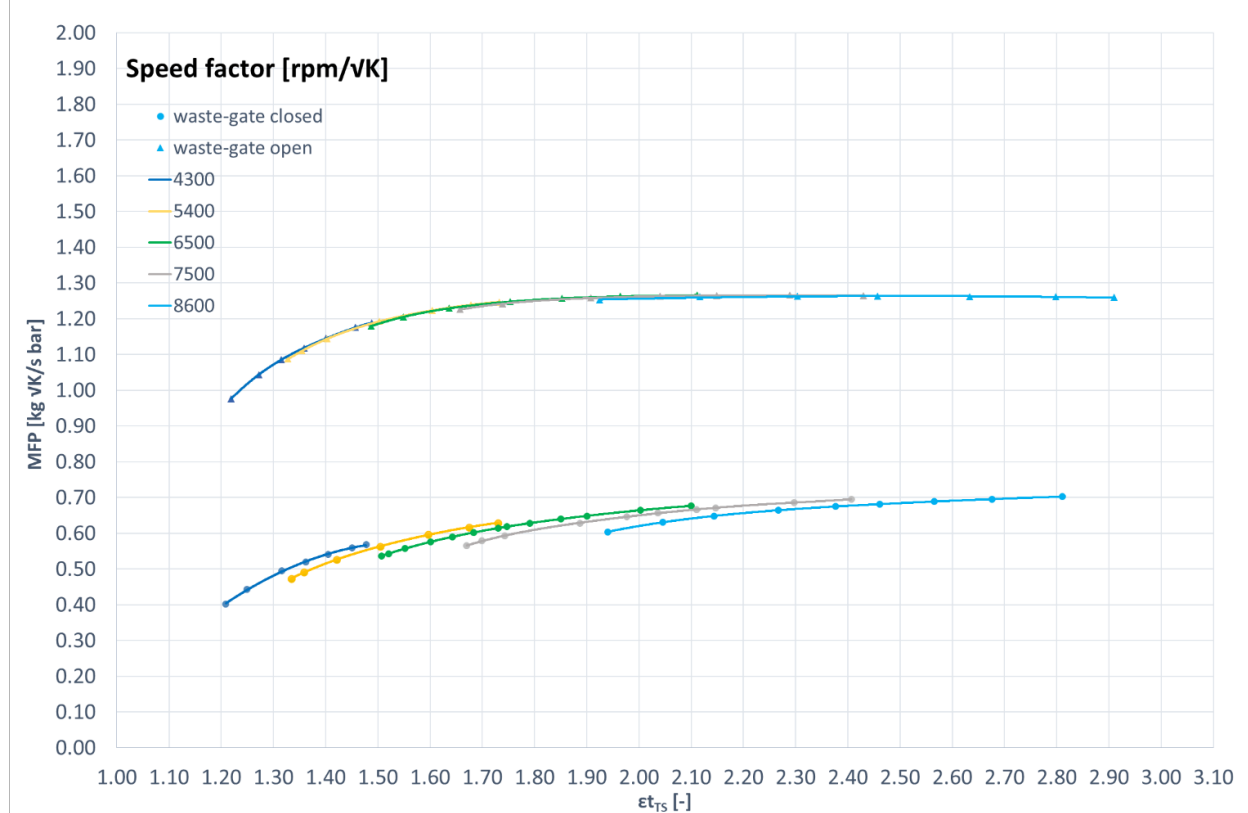$P_{tTS,iso}$ is the turbine total-to-static isentropic power.

Figure 3.14 – Borg Warner turbine swallowing capacity characteristic curves for different position of the waste-gate valve
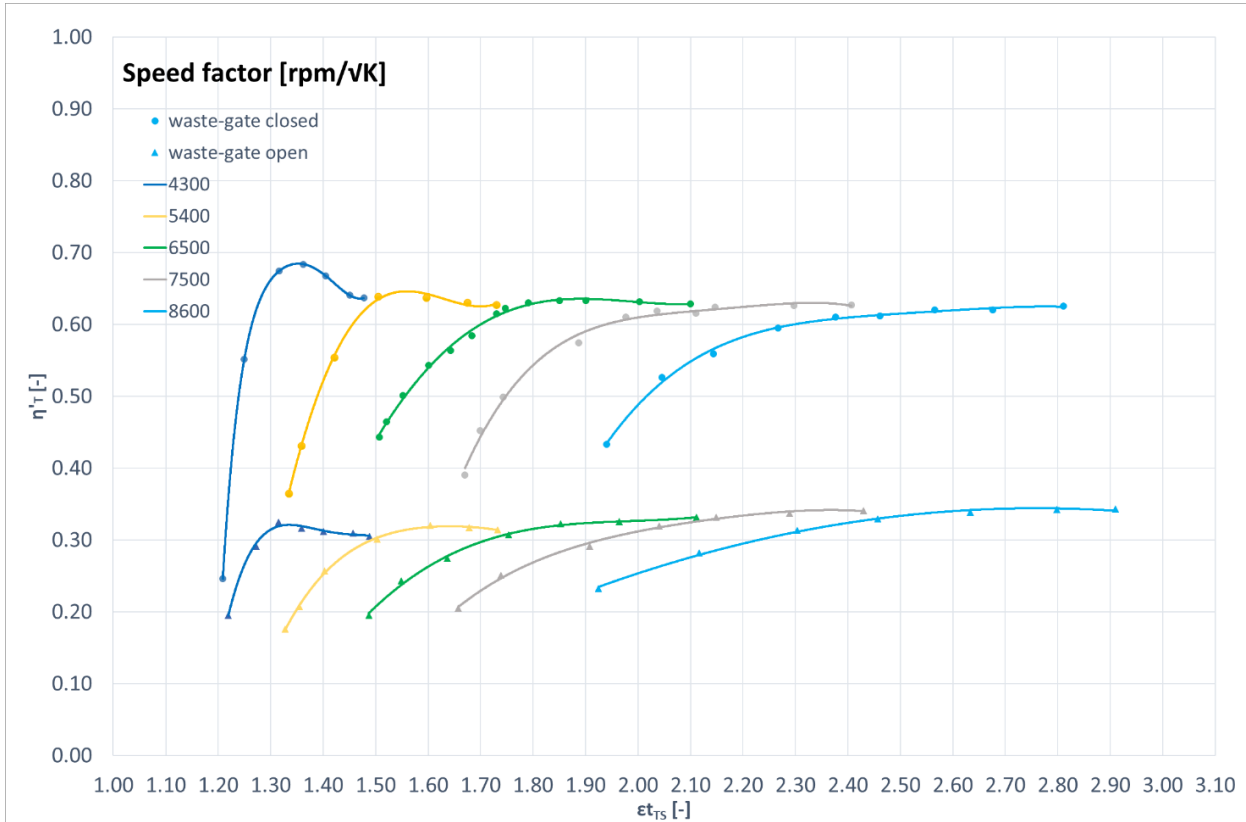
Figure 3.15 – Borg Warner turbine thermomechanical characteristic curves for different position of the waste-gate valve

Figures 3.14 and 3.15 show the turbine characteristic curves for different levels of the turbine speed factor and two different positions of the regulation system. The investigation was extended to several turbine speed factor levels, ranged from 4300 to 8600 rpm/√K with the waste-gate valve in the fully open and fully closed position.

An increase in the mass flow rate factor could be observed when the waste-gate valve is open, confirming the by-pass flow contribution, since the overall mass flow rate is usually measured in the turbine characterization. Under the same conditions, the turbine overall efficiency has significantly decreased, as this quantity refers to the isentropic work of the entire mass flowing through the system (sum of the mass flow rate through the turbine rotor and the by-pass port).

3.2.2 Compressor Steady Flow Performance

As for the e-compressor, an intensive steady state characterization was performed on the compressor of the main turbocharger. In figures 3.16 and 3.17 are reported the characteristic curves.
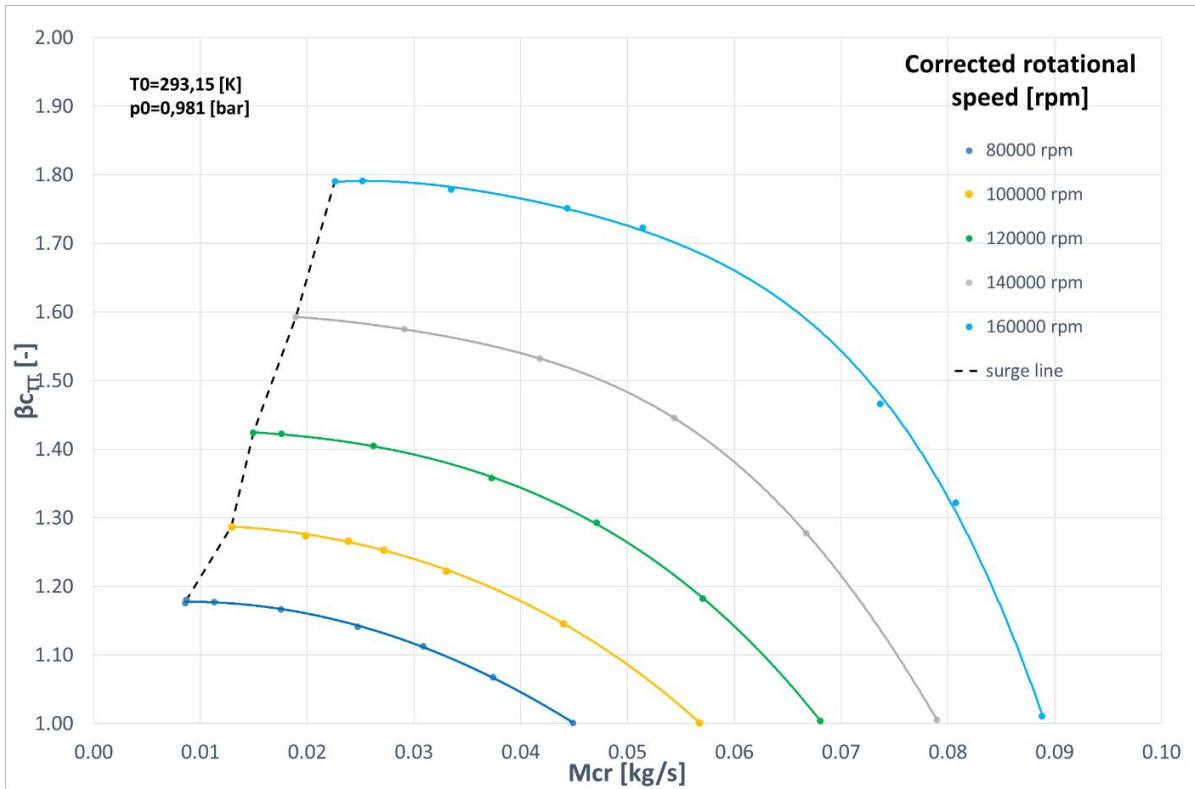
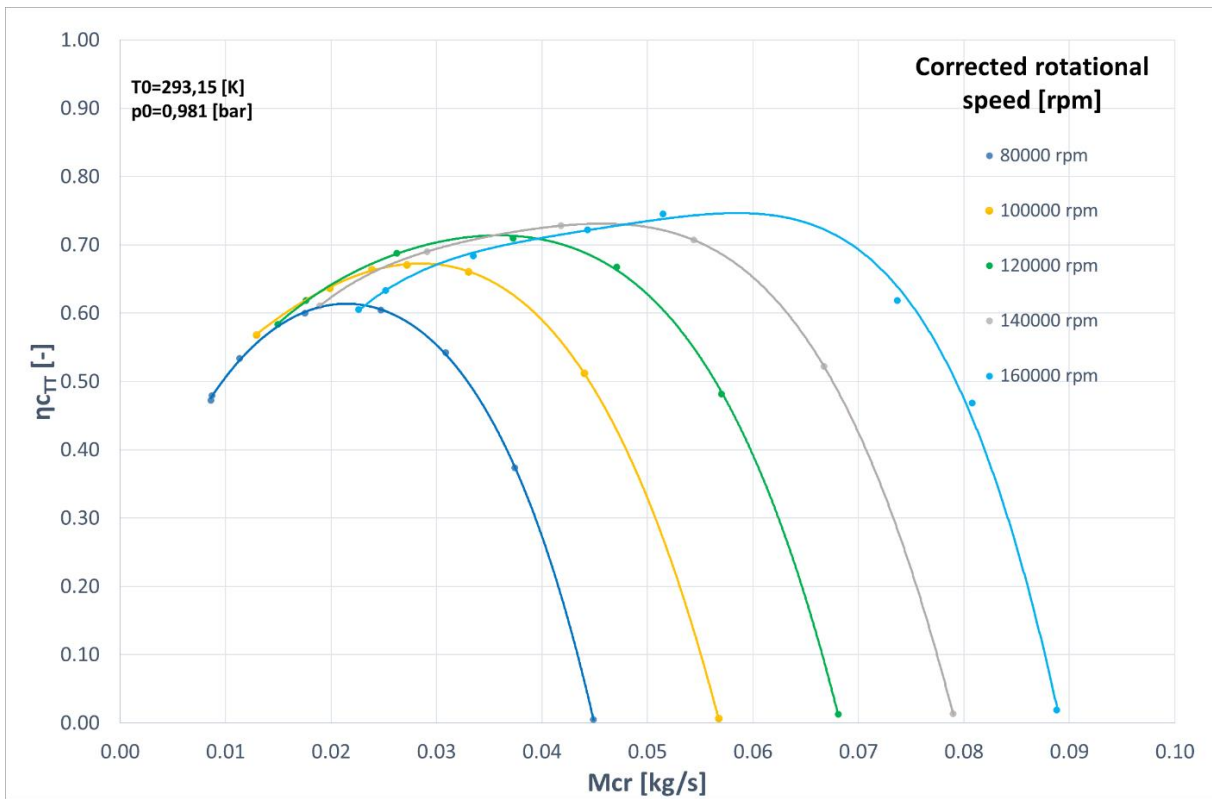*Figure 3.16 – Borg Warner compressor total-to-total pressure ratio maps*

Figure 3.16 – Borg Warner compressor total-to-total isentropic efficiency maps

3.2.3 Compressor Heat Transfer Correction

One of the biggest difficulties in turbomachinery industry is the accurate efficiency determination of its basic components, the compressor and the turbine. Understanding the phenomena affecting this efficiency determination is a key point in the field of automotive engines [60] due to the widespread use of turbochargers for downsized engines. The traditional way to calculate the turbocharger efficiency, based on a ratio of change of compressor enthalpy and isentropic turbine enthalpy from measurements of a gas stand [61], provides inaccurate results, mainly at lower speeds and powers [62].

Most of the turbocharger models in application today rely on the use of compressor maps provided by manufacturers; such maps are determined without taking into account the heat transfer that occurs from the turbine to the compressor during the normal operation of the entire engine, or in other words, these maps assume adiabatic behavior of the turbine and compressor. Nevertheless, in some operative conditions, this hypothesis is far from the reality and the evolution is diabatic. Therefore, the evolution can be represented considering the compression process in the rotor as adiabatic and locating the heat exchanges before and after the mechanical work exchange phase. The reasons for the deviations observed are mainly related to the heat exchange of the air with the metallic parts along the process, which can be produced by different mechanisms for example: a heat flux from the compressor outlet air to the compressor case and wheel caused by the excess heating up of the air due to irreversibilities occurring during the com-pression itself and an eventual external heating of the air before the compressor wheel. The second effect is clearly harmful and is caused by the temperature difference between the 'hot' turbine and the 'cold' compressor. The non-adiabatic contribution to the non-isentropic behavior of the compressor generally has some undesirable consequences; if a compressor map is obtained under adiabatic conditions (or conditions that pretend to be adiabatic), it is used to predict turbocharger performance when the turbocharger operates under real thermal engine conditions (non-adiabatic).

For example, the undesirable consequences are as follows.

- Underestimation or overestimation of the compressor isentropic efficiency if it is directly determined through the measurement of inlet and outlet temperatures.
- Underestimation of air temperature at the compressor outlet if data from 'adiabatic' compressor maps are used to predict such a variable.
- Inaccurate estimation of compressor power and therefore of turbocharger speed during turbocharged engines transient evolutions, especially at low turbocharger speed.

3.2.4.1 Heat Transfer Model Description

The model developed in recent years by the University of Genoa, here reported for the sake of completeness, relies on the assumption that the impeller outlet angle β_{2b} is strictly constant over the whole compressor map. Thus, the velocity triangle at the impeller outlet (Fig. 3. 17) can be determined referring to eq. (3.9).

$$\tan (\beta_{2b}) = \frac{c_{u2i} - u_2 \cdot \left(1 - \frac{0.63\pi}{Z}\right)}{c_{m2i}} \tag{3.9}$$

where the slip velocity is calculated with Stanitz's equation for slip factor, c_{m2i} is the meridian velocity at the impeller, c_{u2i} is the tangential velocity at the impeller and Z is the number of impeller blades. The

evaluation of the impeller outlet angle requires the determination of both tangential and meridian components of flow velocity.
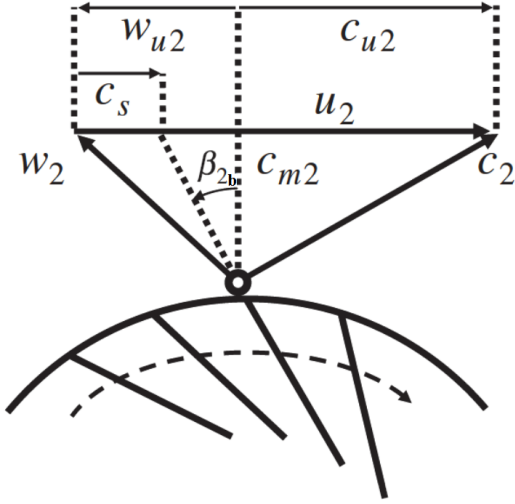

Fig. 3.17: Triangle of velocity at the impeller outlet [63]

The meridian velocity is calculated starting from compressor mass flow rate, compressor diffuser geometry and flow density at the impeller outlet. Since the latter parameter is usually not measured during experimental tests, a recovery model is necessary to step backward to the impeller outlet starting from compressor downstream measuring section. To this aim, the recovery factor for the volute (c_{pv}) and the diffuser (c_{pd}) are used.

$$c_{pv} = \frac{p_{2v} - p_{2d}}{\frac{1}{2}\rho_{2d}c_{2d}^2} \tag{3.10}$$

$$c_{pd} = \frac{p_{2d} - p_{2i}}{\frac{1}{2}\rho_{2i}c_{2i}^2} \tag{3.11}$$

The volute recovery factor is assessed through Enyon and Whitfiled correlation [64].

$$c_{pv} = 2\frac{\cos(\alpha_{2d})}{AR_v}\left(\frac{\tan(\alpha_{2d})}{RR_v} - \frac{1}{AR_v}\right) + 1 - \frac{1}{RR_v^2} \tag{3.12}$$

α_{2d} is the absolute angle at the diffuser outlet, AR_v is the volute area ratio and RR_v is the volute radius ratio. The diffuser recovery factor is calculated with eq. (3.11), in accordance with Sovran and Klomp theory [65].

The tangential velocity is calculated on the basis of the definition of work coefficient pro-posed by Sirakov and Casey [66] and Casey and Fesich [67] under the hypothesis of absence of swirl upstream the compressor inlet.

$$c_{u2i} = \psi_{eul}u_2 \tag{3.13}$$

where ψ_{eul} is the work coefficient. At the design point, where losses contribution is constant at different rotational speed, assuming a quasi-adiabatic compression process, the eulerian work coefficient can be calculated by subtracting the contribution of disk friction losses (indicated with subscript "df") from the real compression work (indicated with subscript "ad").

$$\psi_{eul} = \psi_{ad} - \psi_{df} \tag{3.14}$$

For the evaluation of disk friction losses, the empirical correlation proposed by Daily and Nece [68] is used. Since the compression process is generally diabatic, apparent work coefficient has to be considered.

$$\psi_{app} = \frac{\Delta h_{Cap}}{u_2^2} = \frac{\Delta h_C + q_c}{u_2^2} = \psi_{ad} - \psi_q \tag{3.15}$$

where ψ_q is a coefficient defined according to [66]. Under the hypothesis that heat flux is mainly due to temperature difference between the compressor and the lubricant casing, the heat exchange can be calculated referring to eq. (3.16).

$$Q_c = K \, \Delta T \tag{3.16}$$

where K is a conductive coefficient. Therefore, the heat transfer coefficient can be expressed with eq. (3.17).

$$\psi_q = \frac{k'_c \Delta T}{\phi_{T1} \rho_{T1} a_{T1}^3 M u_2^3} \tag{3.17}$$

Where a is the speed of sound, Mu the tip speed Mach number. The term $k'_c = K/D_2^2$ is strictly constant throughout the map for a fixed turbocharger unit, since it depends only on geometrical terms. Even if k'_c is usually quite difficult to be determined, it can be used as a convergence coefficient for the whole map, starting from a first guess value.
Finally, the adiabatic work coefficient can be calculated and the adiabatic efficiency can be obtained.

$$\psi_{ad} = \psi_{ap} - \psi_{df} - \psi_q \tag{3.18}$$

$$\eta_{C,ad} = \frac{\Delta h_{C,is}}{\psi_{ad} u_2^2} \tag{3.19}$$

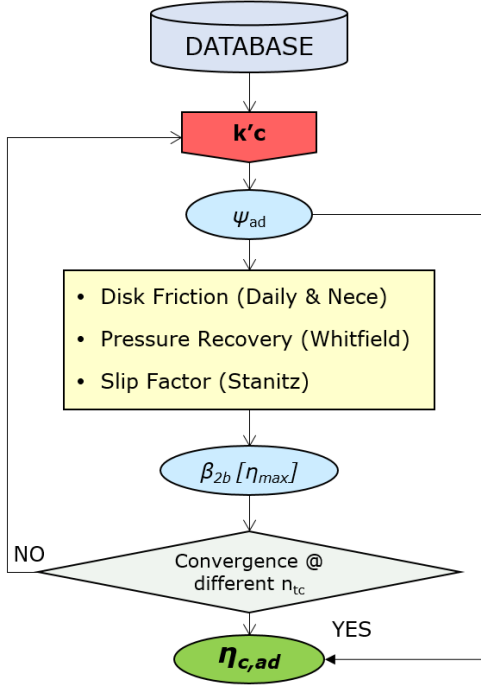In Fig. 3.18 the model flow chart is reported.

Figure 3.18 – Model flow Chart [57]

3.2.4.2 Heat Transfer Model Results

In Figure 3.19 the comparison between the experimental data and the heat transfer correction model results is presented. A good behavior of the model can be observed, the deviation is minimized with the increase of the compressor mass flow rate. At the lower value of the corrected rotational speed (80000 rpm) the efficiency measured is underestimated of more than the 10%, value that decreases to 5% at 100000 rpm and that can consider negligible for the higher rotational speed, perfectly in accordance with the theory reported above: the impact of heat transfer is less important at high rotational speed since the temperature difference between the compressor and the turbine side decreases and compressor efficiency curves tend to progressively approach the adiabatic curves. Referring to the isentropic compressor efficiency (equation 3.4) the heat flux from the turbine cause an overestimation of the compressor outlet temperature T_{T2} that determine a decrease in the compressor efficiency due to the non adiabaticity of the process.
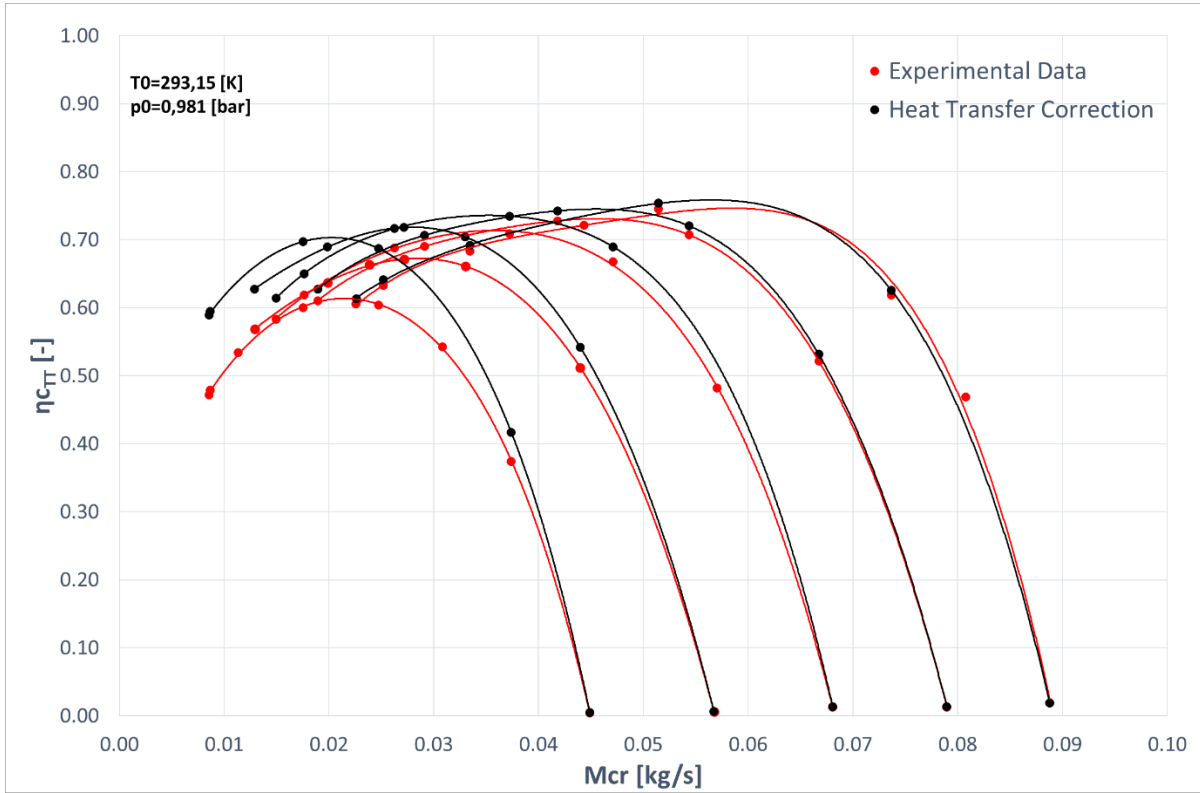
Figure 3.19 – Borg Warner compressor total-to-total isentropic efficiency maps. Comparison of experimental data end heat transfer correction model results

3.3 Twin Stage Boosting System Transient Characterization

3.3.1 Control system

This paragraph analyzed the hardware and software control systems installed and programmed to carry out the transient tests experimental campaign. The system is composed by an electronic actuator, which allows the adjustment of the position of the waste-gate valve to modulate the turbine power; the electric motor is commanded by a control unit on the CAN bus; a by-pass throttle valve placed in parallel to the e-compressor.

Due to the absence of the engine control unit to link these components, Arduino hardware platforms were used with relative modules that allowed communication with the actuators and the e-compressor. To achieve this goal, dedicated software developed in C ++ has been developed.

3.3.1.1 Waste-gate Valve Actuator

This component is installed to control the opening of the waste-gate valve located. Usually, this valve is controlled by a pneumatic signal taken by the compressor outlet.

When the compressor discharge pressure is too high, in order to avoid operation outside the system design limits, this type of configuration open the waste-gate valve in order to reduce the power delivered by the turbine to the compressor.

In the performed tests, the waste-gate assumes the function of controlling the power generated by the turbine.

50

In this regard, it is necessary to use an electronic component, controllable from a PC, which controls the valve position. To achieve this, the OEM supplied a component (Fig. 3.19), called "1000M.000168-638", which is used in new generation vehicles for flexible control of the waste-gate valve.

Figure 3.20 – 1000M.000168-638 waste-gate valve actuator

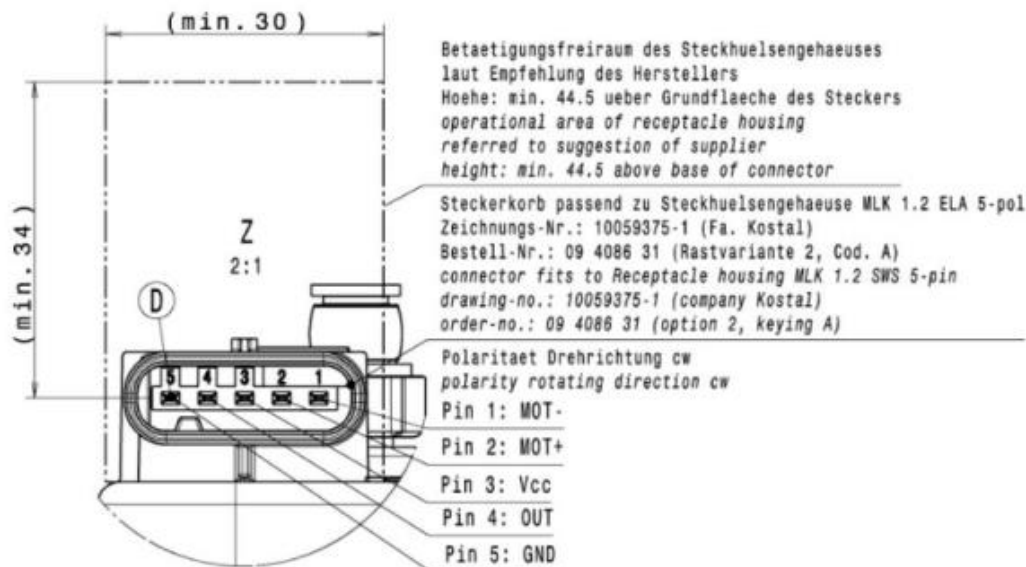In figure 3.20 it is also possible to identify the connection pins with the control system, the details of which are shown in figure 3.21.

Figure 3.21 – 1000M.000168-638 pinout

The actuator is driven by a 12V DC electric motor which is modulated in PWM (Pulse width modulation) [69] for the opening speed, and the position feedback is provided by a potentiometric position sensor. To move the valve, it is necessary to be able to supply a duty cycle of 12V at the electric motor. In addition to this, it is necessary to read in real time the position of the valve from the potentiometer in order to correct the duty cycle. Moreover, it is necessary to adjust the direction of the supply voltage to open or close the valve. For this purpose, it was decided to program an "Arduino Leonardo" electronic board connected to a "Cytron 10A 5-30V Dual Channel DC Motor Driver" power module (figure 3.22).

Figure 3.22– Arduino Leonardo (on the left) and Cytron 10A 5-30V dual channel DC motor driver (on the right)

In figures 3.23 the connection diagram between Arduino, the Cytron power supply module, the power supply and the electric motor of the waste-gate valve actuator.
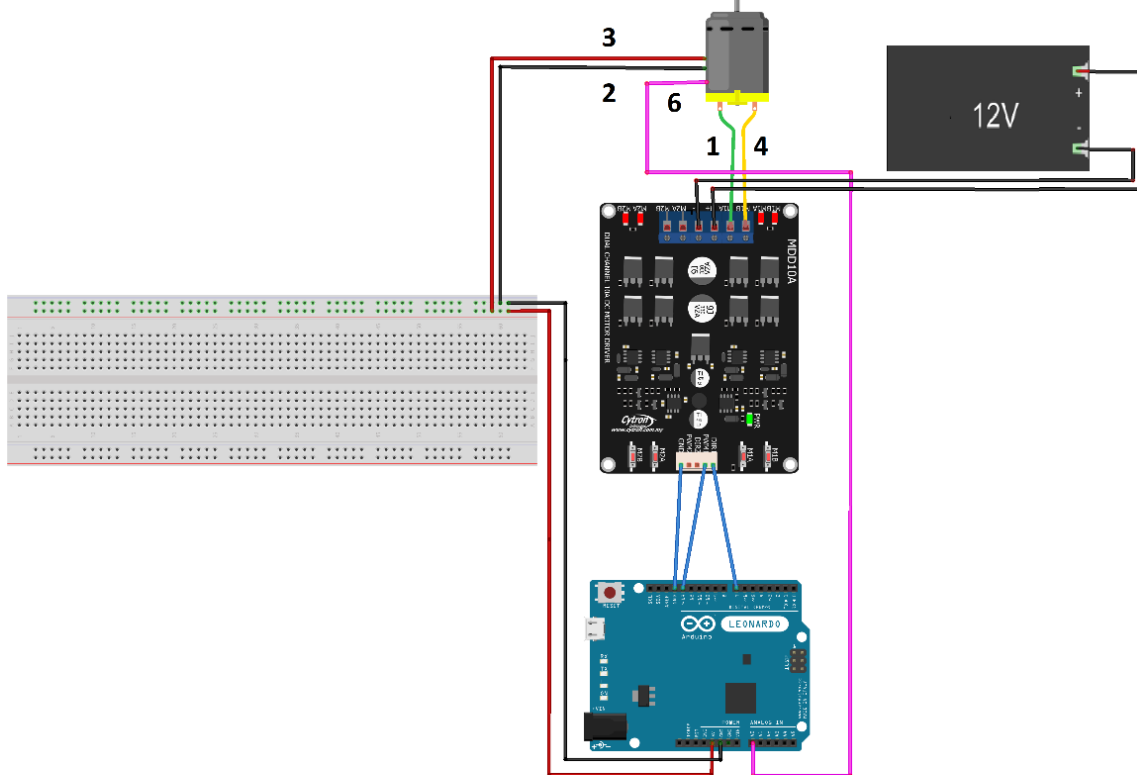

Figure 3.23 – Electric connections of the waste-gate valve control system

The details of the code developed in C ++ are reported in appendix C (C ++ code for controlling the waste-gate valve control system).

3.3.1.2 e-Compressor and By-Pass Valve

The test system also has to provide the activation of the e-compressor by the set point of the rotation speed via CAN bus. Subsequently, the bypass valve placed in parallel with the e-compressor must close once the rotation speed target has been reached. In figure 3.24 the e-compressor and the by-pass valve.

Figure 3.24 – e-Compressor and by-pass valve

On vehicle the eSC communicates with the control unit on the CAN bus exchanging messages of 8 bytes written in hexadecimal code. Basically, the messages exchanged are divided into two categories, each identified by its own "ID" number: messages delivered by the control unit to the booster (ID 0x112) and messages send by the booster to the control unit (ID 0x200). The first are messages containing the instructions for the e-compressor and diagnostic information on the vehicle status; the others are messages containing diagnostic information of the e-compressor, including its internal temperature and its rotation speed. Due the absence of an engine control unit, it was necessary to replicate the ability to send and receive signals with the component on the computer.

The structure of the messages exchanged on the CAN bus is the "Standard Frame" [70].

A message in the standard format is made up of 108 bits and is structured as in figure 3.25.

Figure 3.25 – Structure of a CAN message in standard format

Of the eight elements that compose the message, the most important are: "CAN-ID", "Control" and "Data field" [71].

- "CAN-ID" contains information relating to the type of message in question. A number that identifies the type of message is written in the 11 dedicated memory bits.
- "Control" it serves to inform how many bytes of data are used in the "data" field for the message content. It is a number from 0 to 8 in decimal encoding.
- "Data" it is the most important part: it consists of 64 bits of memory into which the message content is written.

Depending on the ID, i.e. the type of message, the content that is written inside the 64 bits of the "data" field changes.

In order to understand the content of the 8 bytes of the "data" field it is necessary to have the database file provided by the component programmer which allows to understand the filling criteria and the meaning of the 64 bits.

Figure 3.26 shows the 64-bit grid of information that make up the 8 bytes of the "data" field. Writing a CAN message means fill the bits with 0 and 1 in order to compose numbers which, if properly interpreted, represent signals to be given to the component. In the present case, the filling order of the bits is the Big-Endian (Motorola) [71].
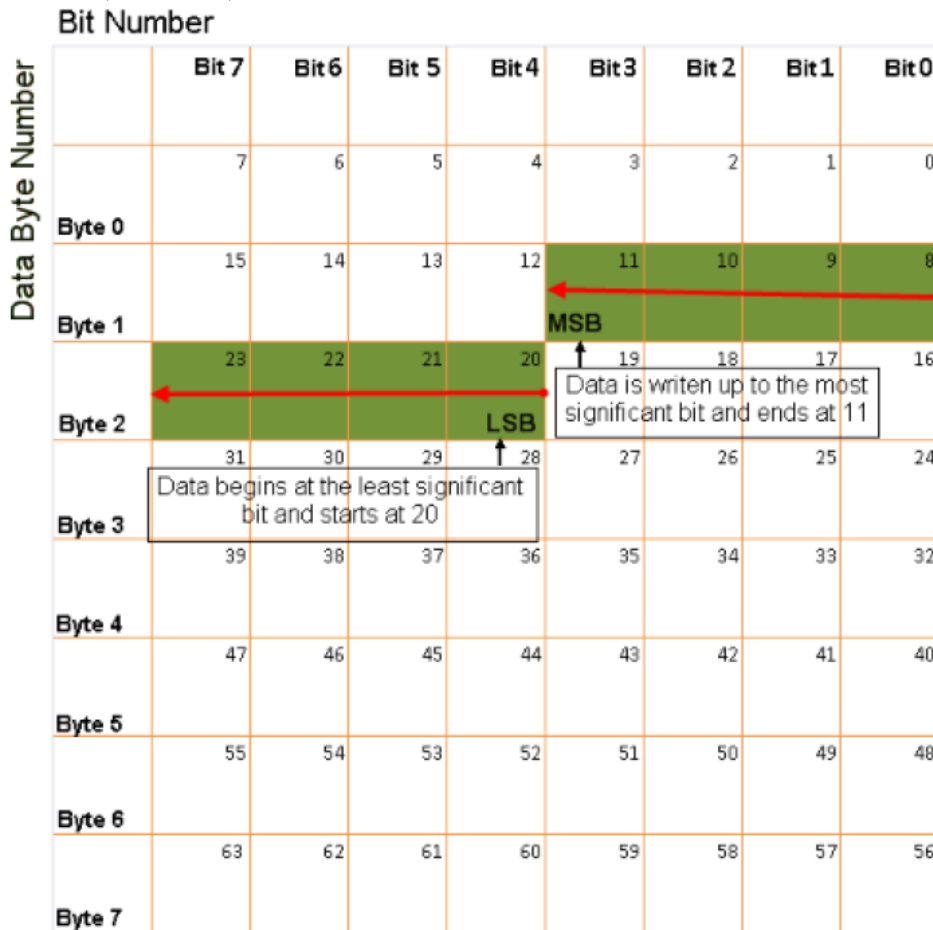

Figure 3.26 – Big-Endian (Motorola) bits filling criteria

To understand how the 64-bit grid have to be compile, refer to the ".db" database file screen which can be opened with the "Vector CANdb ++" software (Fig. 3.27).
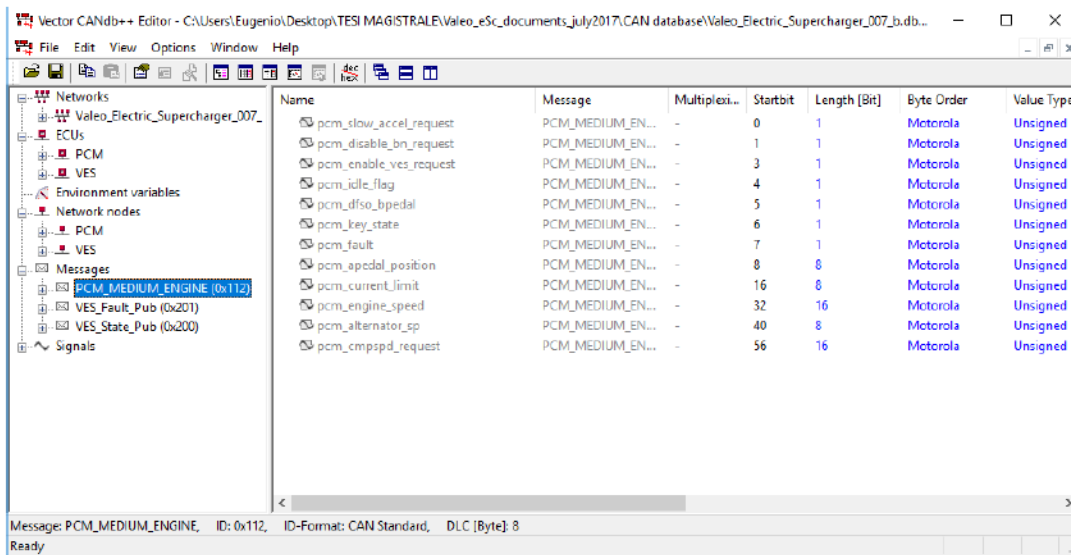
Figure 3.27 – Screen of file ".db"

Within this file there is a list of the signals that can be exchanged (sent and received) between the e-compressor and the control unit. On the left there are three types of messages, each identified by its CAN-ID:

- PCM_MEDIUM_ENGINE (0x112)
- VES_Fault_Pub (0x201)
- VES_State_Pub (0x200)

For example, the "pcm_cmpspd_request" signal is the speed set point that is requested by the control unit to the e-compressor.

Figure 3.28 is the screen that can be open clicking on the above mentioned signal, it is useful to understand how this signal is written in the 64 bits of the "data" field of the message.

The first screen on the left provides the startbit; in this case starts from bit 56, that is from the last bit of the grid presented in figure 3.26

The second screen on the right provides the criteria for translation of the speed setpoint value from decimal to binary coding.
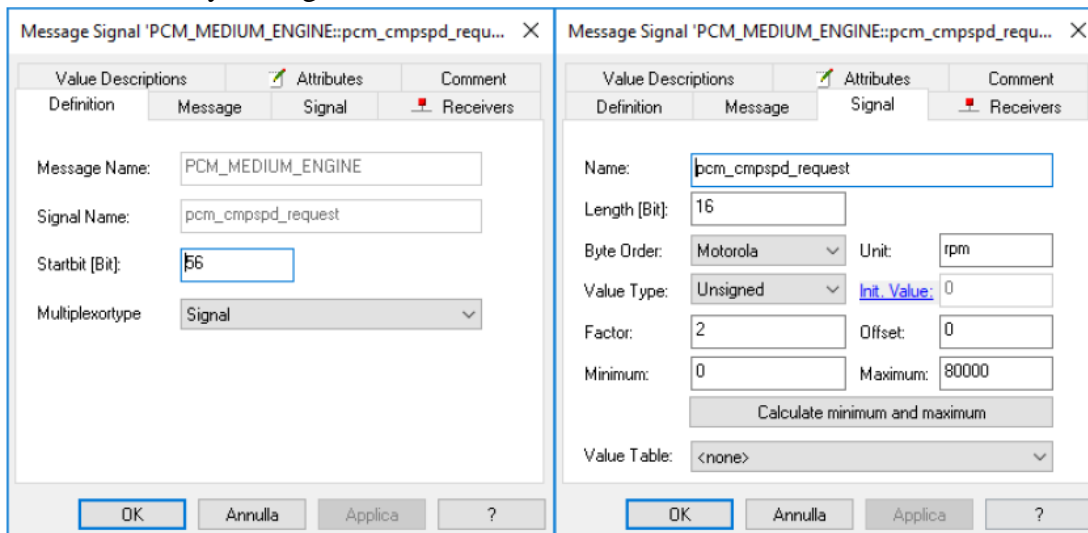

Figure 3.28 – Encoding of the pcm_cmpspd_request signal in a CAN message

To manage communications on the CAN bus, a CAN interface board (WAVGAT MCP2515) connected to an Arduino UNO board has been adopted. In figure 3.29 the diagram with the electronic connections. In particular, the two cables represented by L and H are connected to the control circuit of the e-compressor.
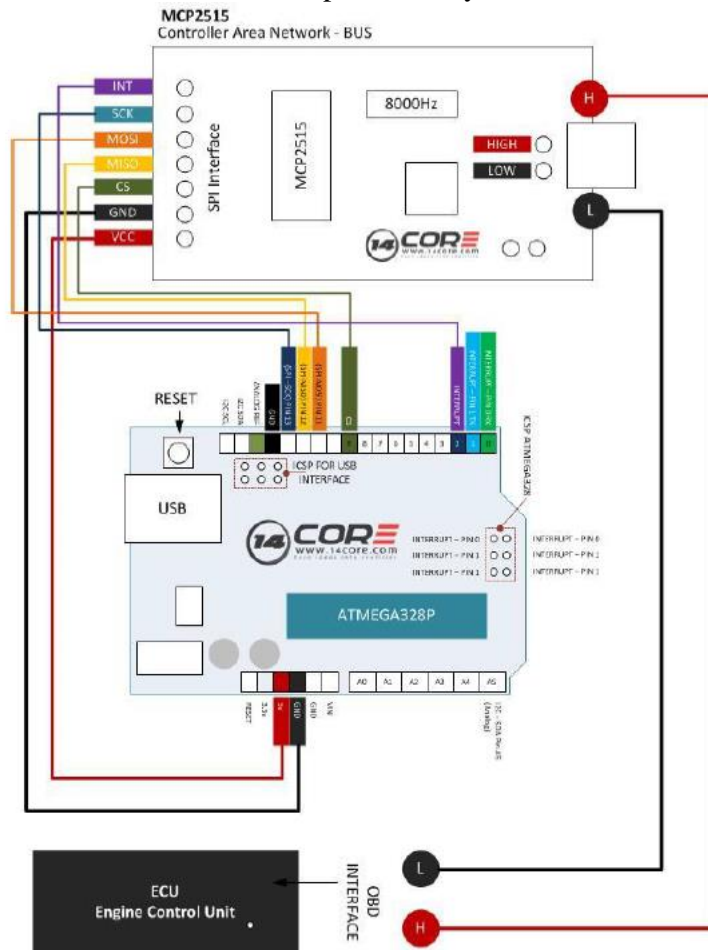

Figure 3.29 – Arduino UNO and WAVGAT MCP2515 connection diagram

A "Cytron 10A 5-30V Dual Channel DC Motor Driver" power module, like the one adopted for the control of the waste-gate valve, is connected to the Arduino UNO board is connected. In figure 3.30 the diagram with the electronic connections.
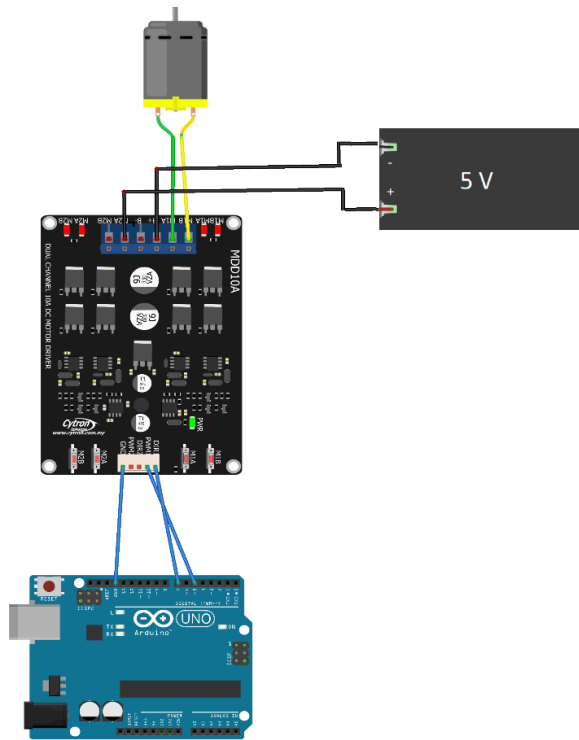
Figure 3.30 – Arduino UNO, Cytron board and by-pass valve connection diagram

Appendix D (C++ code for e-compressor and by-pass valve control system) shows the code for sending and receiving messages on the CAN bus with the above mentioned hardware.

Additionally, the code is programmed to provide an open loop PWM signal to the bypass valve once the electric compressor has reached the set speed setpoint.

3.3.2 e-Compressor electric connections

Inside the eSC is installed a variable reluctance (SR) electric motor. The reasons that pushed the manufacturer towards this solution are the simplicity and the reliability of the system due to the absence of rotor windings or permanent magnets.

Figure 3.31 shows the wiring diagram for the electric motor control. A control module and a power module are integrated in the eSC: they guarantee efficient management of the electrical power. The control module sends diagnostic messages relating to the operation condition of the eSC and receives the speed set point command signal, via the CAN bus.

The power module has the task of providing electrical energy in order to accelerate or decelerate the electric motor to the desired rotational speed.
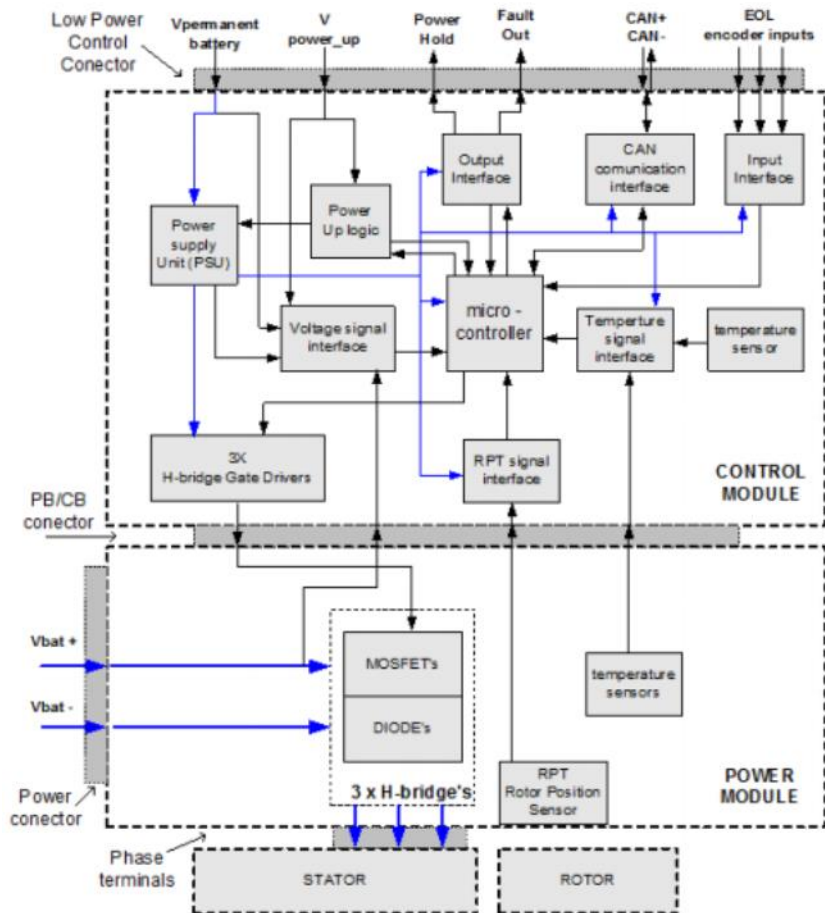
Fig. 3.31 – Block diagram of the control and power module of the e-compressor

There are two connectors on the eSC: one for the power circuit and one for the control circuit. Terminals B +/- connect the component to the battery emulator with heavy duty cables; The control connector connects the e-compressor to the CAN bus described in detail in paragraph 3.3.1.
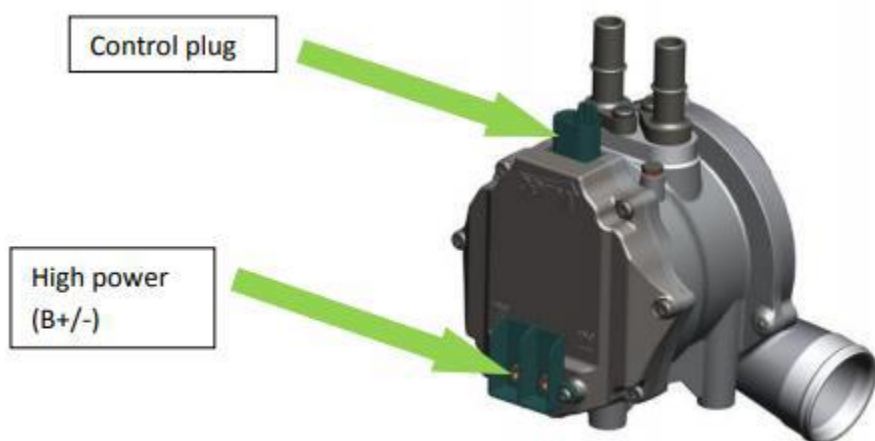

Fig. 3.32 – Power and control connectors

The diagram in figure 3.33 shows the electrical connections between the e-compressor and the battery simulator (par. 2.4.1). Moreover, it is possible to observe the power circuit (from terminals B +/-, to the poles of the emulator), and the control circuit (from the control connector to the power relay and to the CAN network).
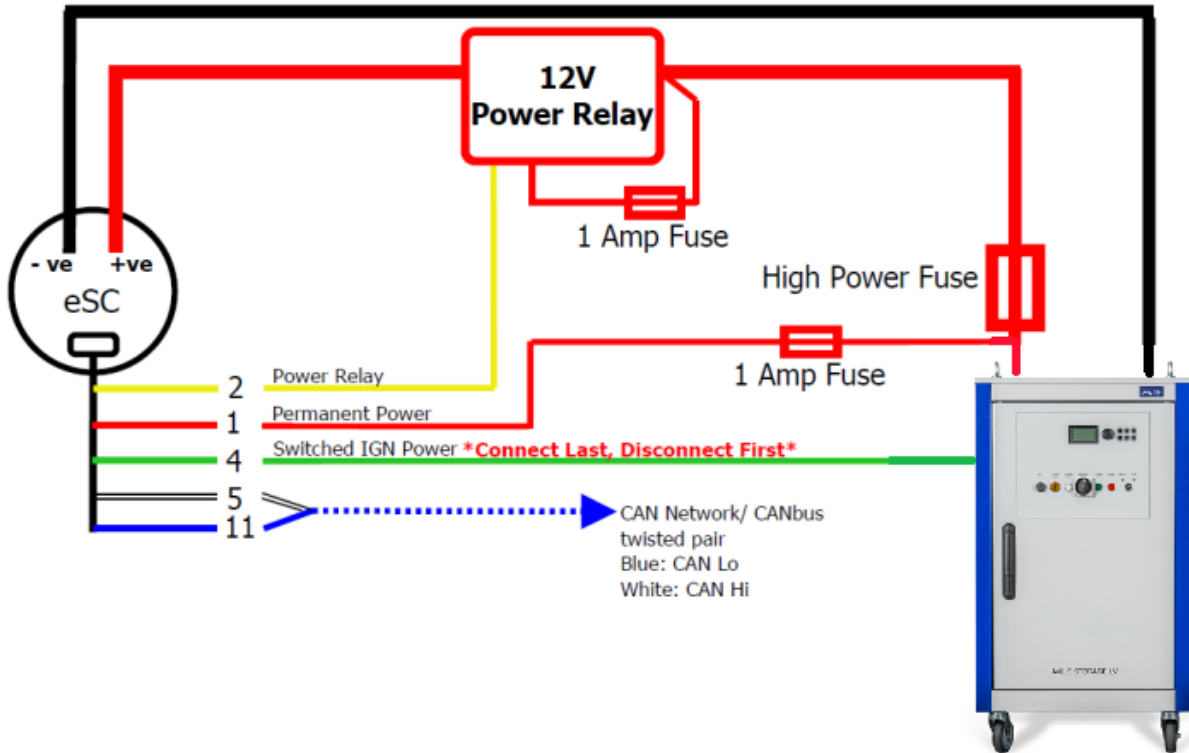

Fig. 3.33 – Electrical and control wiring diagram

3.3.3 Experimental Campaign Description

The goal of the experimental campaign is to evaluate the time reduction of the boosting system's transient response by coupling the e-compressor to the traditional turbocharger.
For both configurations considered (upstream and downstream) two different kinds of test are performed. Concerning the first kind of test, three operating points of the turbocharger are chosen accordingly to the engine operative point in terms of intake pressure, therefore compressor downstream pressure (p_2) and mass flow rate (m_c). Thus, the relative operating point of the turbocharger is determined through the performance maps.
Starting from the first operating condition, the e-compressor is driven to accelerate to a certain rotational speed level. For each rotational speed, the waste-gate valve is fixed to different positions, from fully open (100%) to fully closed (0%), regulating the power delivered to the main compressor.
The operating points, speeds and waste-gate opening positions are reported in Tables 3.1, 3.2 and 3.3.

p_2 [bar]	$\dot{M}_{cr}$ [kg/s]
1.27	0.022
1.51	0.026
1.75	0.030

Table 3.1 - Turbocharger operating points

n_{eSC} [rpm]
5000 (idle)
40000
50000
60000
65000

Table 3.2 - e-Compressor rotational speed

WG [%]
100
25
10
0

Table 3.3 - Waste-gate valve opening positions

The second kind of test is aimed to compare the transient response of the system actuating only the traditional turbocharger through the waste-gate valve position with the system's response by actuating only the e-compressor. Therefore, two different transient responses are evaluated.

Starting from the same operating conditions presented in Table 3.1 the waste-gate is driven from a fully open position to a fully closed while the e-compressor is maintained in idle condition.

Once the system has stabilized, the waste-gate valve is driven in a fully open position and kept in this position. The e-compressor is then controlled to accelerate in order to reach the same conditions obtained by the turbocharger working alone.

3.3.4 Experimental Campaign in Upstream Configuration

This section provides a detailed description of the layout and results obtained in upstream configuration.

3.3.4.1 Layout

Figure 3.34 schematically shows a top view of the plant layout in upstream configuration.
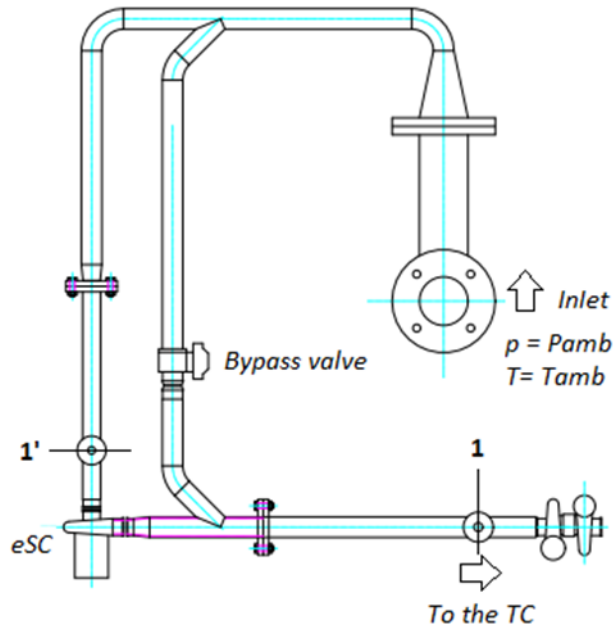
Figure 3.34 – Layout view from the top in upstream configuration

It is possible to see the positions of the various components and of the measurement stations (called 1 and 1 ') placed upstream of the turbomachinery.

The measuring stations are instrumented with hot film anemometers for instant flow measurements (par. 2.2.5.5), piezoresistive transducers with high and low response frequency (par. 2.2.3.1), and resistance thermometers for temperature measurements (par. 2.2).

In figure 3.35 an overview of the test rig set-up realized for the test in upstream configuration.

Figure 3.35 – Overview of the test rig set-up in upstream configuration

In figure 3.36 the detail of the ducts of the eSC (on the right) and of the by-pass valve (on the left), moreover the black ducts for the refrigerant inlet and outlet of the e-compressor are clearly visible, essential for the correct operation the bearings and of the electrical component. It is also possible to observe in detail the measurement instrumentation of station 1 '.

Figure 3.36 – e-Compressor and by-pass valve duct

In Figure 3.37 it is possible to see the traditional turbocharger and the detail of the measuring station 1. It is also possible to observe the electronic actuator of the waste-gate valve and the inlet of the lubricating oil of bearing case of the turbocharger.
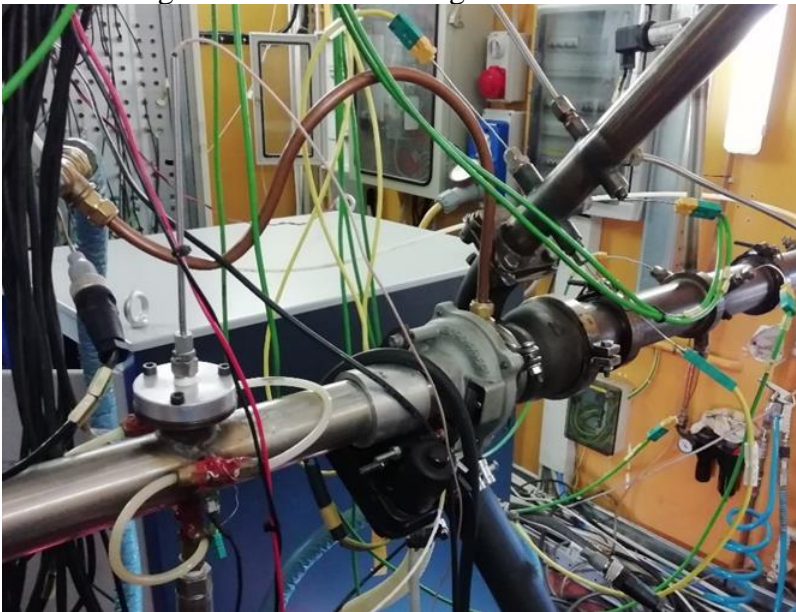

Figure 3.37 – Traditional turbocharger and measuring station 1

3.3.4.2 Results

The first layout analyzed presents the e-compressor placed upstream of the traditional one. In this section a selection of results is presented. The comments and the considerations can however be extended to all the operating conditions analyzed.

In Figure 3.38 the overall pressure ratio is presented, defined as the ratio between the downstream turbocharger pressure and the eSC upstream pressure ($\beta_{overall} = p_2/p_{1'}$). The starting point refers to p_2 = 1.75 bar and M_c = 0.03 kg/s.

In this series of data, the e-compressor target speed always goes from idle condition to 50000 rpm and the waste-gate opening position varies from 100% to 0%. A smaller value of the waste-gate valve opening means that a higher mass flow rate feeds the turbine, producing more power and therefore a higher pressure ratio at the compressor side.
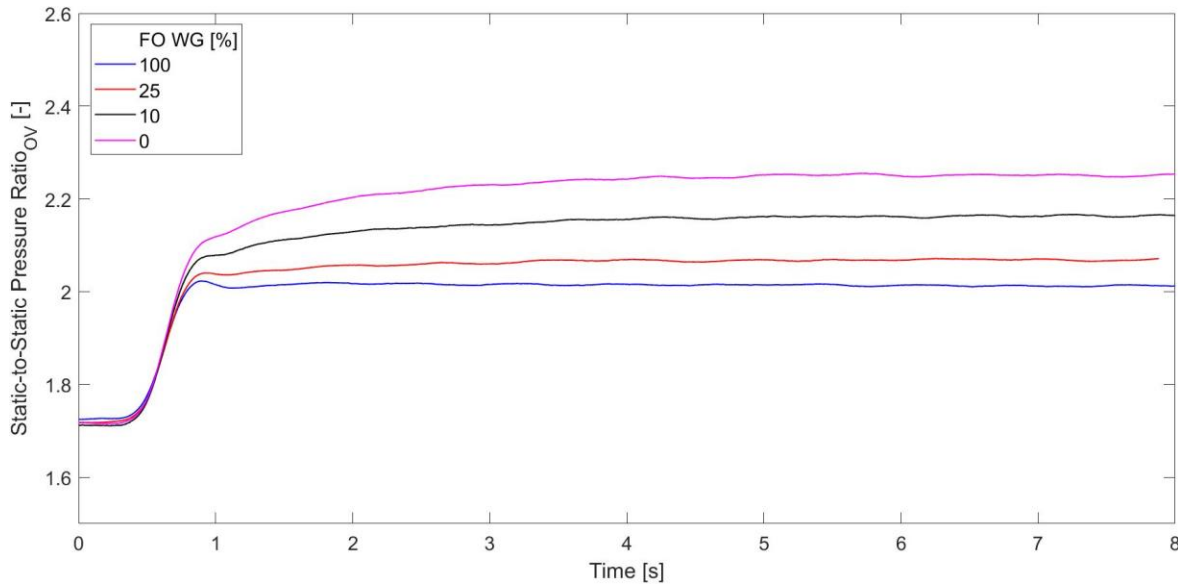

Figure 3.38 – Overall pressure ratio for different waste-gate valve positions

In order to highlight the benefit in terms of transient response of the main turbocharger, it is important to analyse the time requested by the e-compressor to reach the rotational speed target, i.e. the boost pressure required by the ECU.

In Figure 3.39 the final position of the waste-gate valve was fixed to 25%. The curves show the overall pressure ratio trend for different e-compressor SC rotational speed. The starting point refers to p_2 = 1.51 bar and M_c = 0.026 kg/s. The turbocharger works with a fixed variation, therefore the overall pressure ratio changes are due to the e-compressor acceleration.
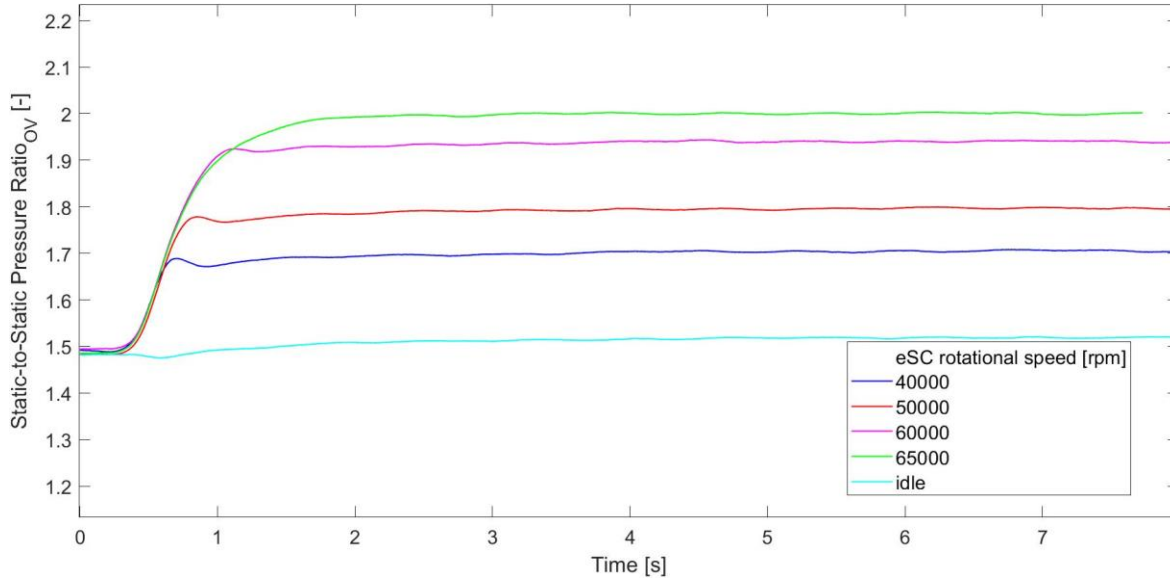
Figure 3.39 – Overall pressure ratio for different eSC rotational speed

The pressure ratio of the traditional compressor ($\beta_{TC} = p_2/p_1$), visible in figure 3.40, is represented by varying the opening of the WG and keeping the eSC rotation speed at the and of the transient fixed at 50000rpm. It can be noted that there is a decrease in the pressure ratio due to the activation of the e-compressor. This behavior is due to the fact that the e-compressor rapidly increases its pressure ratio and mass flow rate through the circuit.
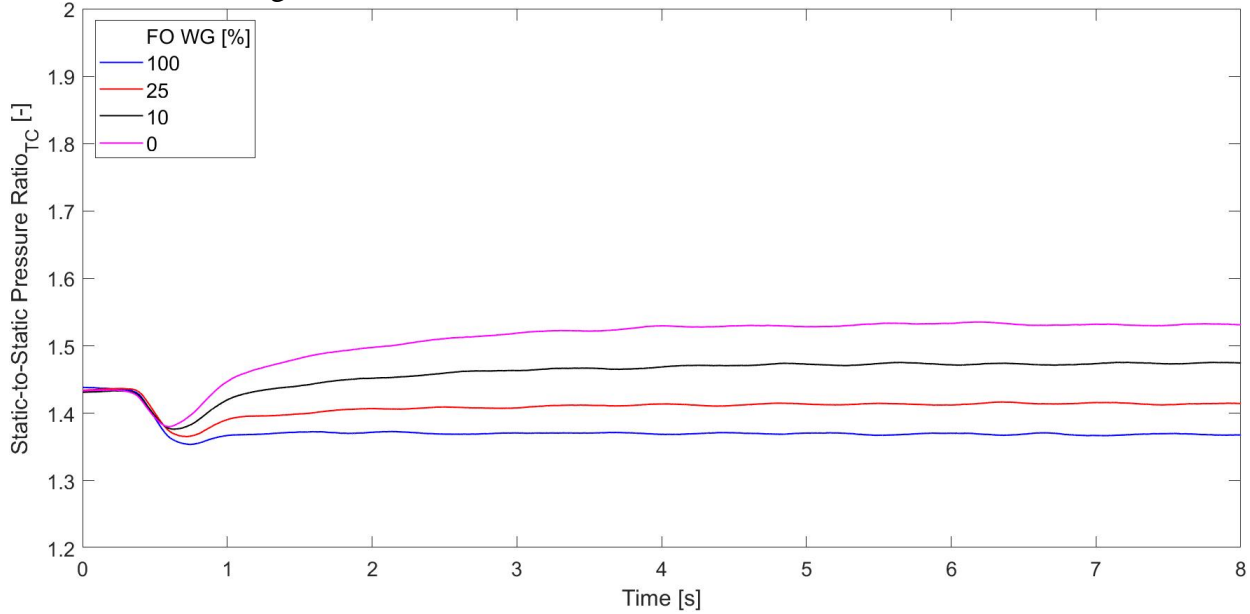

Figure 3.40 – Main compressor pressure ratio for different waste-gate valve positions

The pressure ratio of the main turbocharger can also be analyzed by varying the final rotational speed of the eSC, as shown in Figure 3.41; as in figure 3.40 it can be seen more clearly that as the rotation speed of the e-compressor increases, the pressure ratio of the main turbocharger decreases. Considering the power equation of a compressor, this phenomenon can be better understood:

64

$$P_C = M_C c_p T_{T1} \left(\beta_{TC}^{\frac{k-1}{k}} - 1\right) \tag{3.20}$$

where M_C is the mass flow rate, c_p the specific heat capacity at constant pressure, T_{T1} the total temperature at the main compressor inlet and k is the capacity heat ratio.

At the main compressor inlet the air mass flow (M_C) is incresed due to the eSC acceleration; the compressor power (P_C) at the end of the transient is kept constant due to the fixed final position of the waste-gate valve; and so a reduction of β_{TC} will be determined to maintain equality of the left and right sides of the equation 3.20.
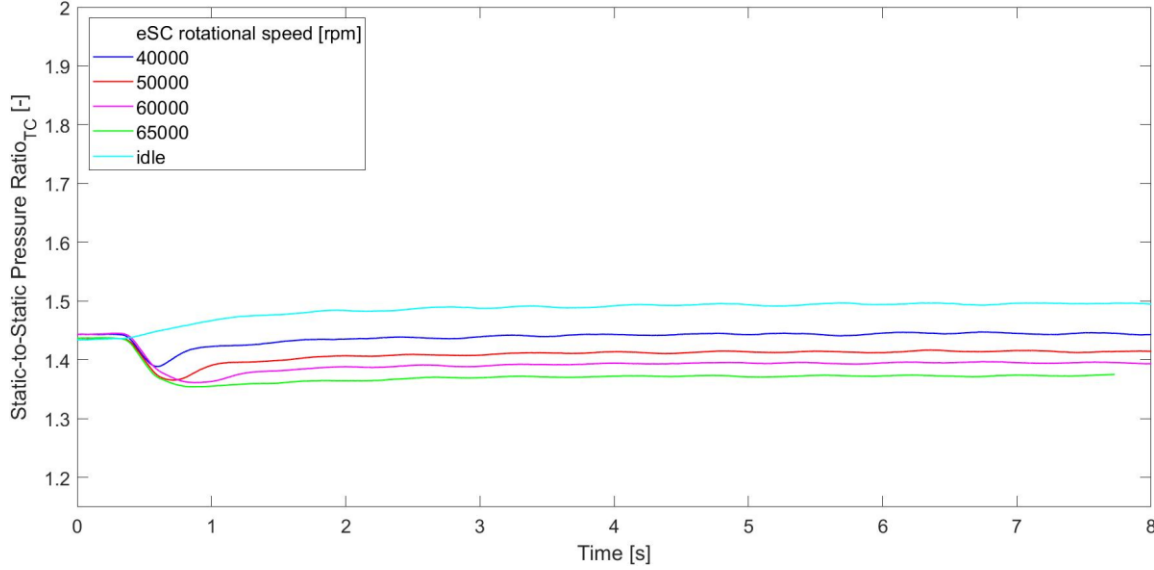

Figure 3.41 – Main compressor pressure ratio for different e-compressor rotational speed

Figure 3.42 shows the compression ratio of the e-compressor (β_{eSC}) as the fractional opening of the waste-gate valve varies. Since all the curves are perfectly overlapped the position of the main turbocharger regulation system does not affect the performance of the e-compressor.
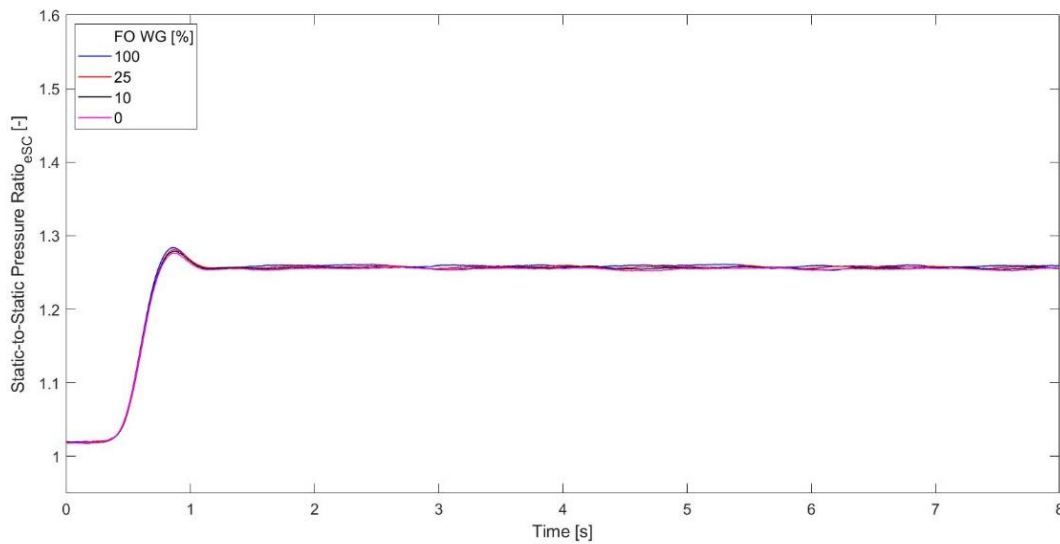

Figure 3.42 – e-Compressor pressure ratio for different waste-gate valve position

In Figure 3.43, the pressure ratio of the e-compressor is plotted against time for different rotational speed targets and the waste-gate valve kept in fully open position during all the transient operations. The increase in the pressure ratio is significant (about 1 second) confirming the good behavior of these components in the time-to-boost enhancement of the turbocharging system. The effects of different e-compressor rotational speeds can be observed: for the lower rotational speeds there is a small overshoot, probably caused by the control system.
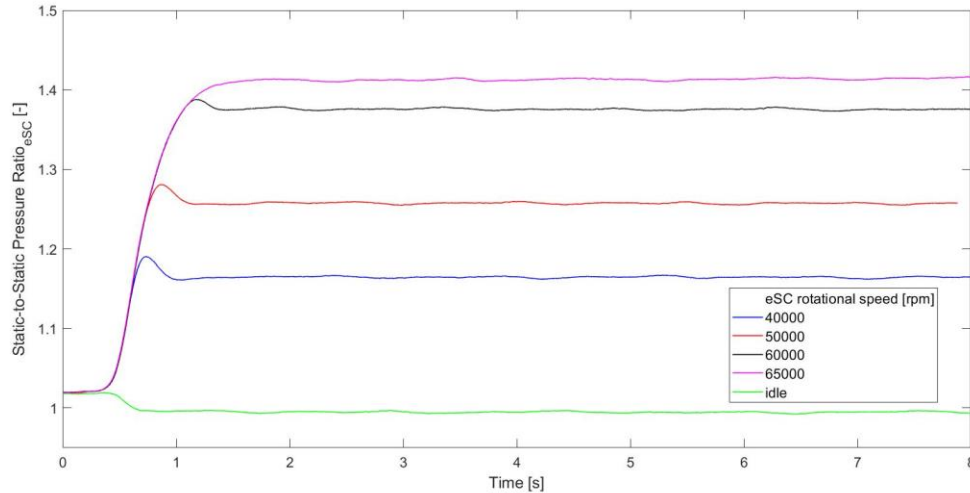

Figure 3.43 – e-Compressor pressure ratio for different e-compressor rotational speed

The results of the second type of test described in paragraph 3.3.3 are shown below: to understand the time-to-boost advantage provided by the e-compressor, it is necessary to compare the transient response of the main turbocharger and the e-compressor. In Figure 3.44, the solid line represents the transient response of the boosting system when the waste-gate valve is moved from a fully open to a fully closed position and the e-compressor is kept in idle condition. The dashed line represents another transient operation carried out to obtain the same outlet pressure (i.e. engine intake pressure); the boost is provided exclusively by the e-compressor, the waste-gate valve remains in the fully open position. An important improvement in the time required to reach the final condition could be observed when the e-compressor is required to adjust the final pressure, in other words with the activation of the e-compressor the turbo-lag could be reduced by several seconds. Furthermore, the same pressure can be reached with a lower contribution from the traditional turbocharger, this allows the waste-gate valve to be kept in a more open position, reducing the engine backpressure, an important objective for increasing engine efficiency. Furthermore, actuating this control strategy of the whole boosting system it is possible to reduce the light-off times of the after-treatment systems thanks to a greater quantity of gas passing through the waste-gate.
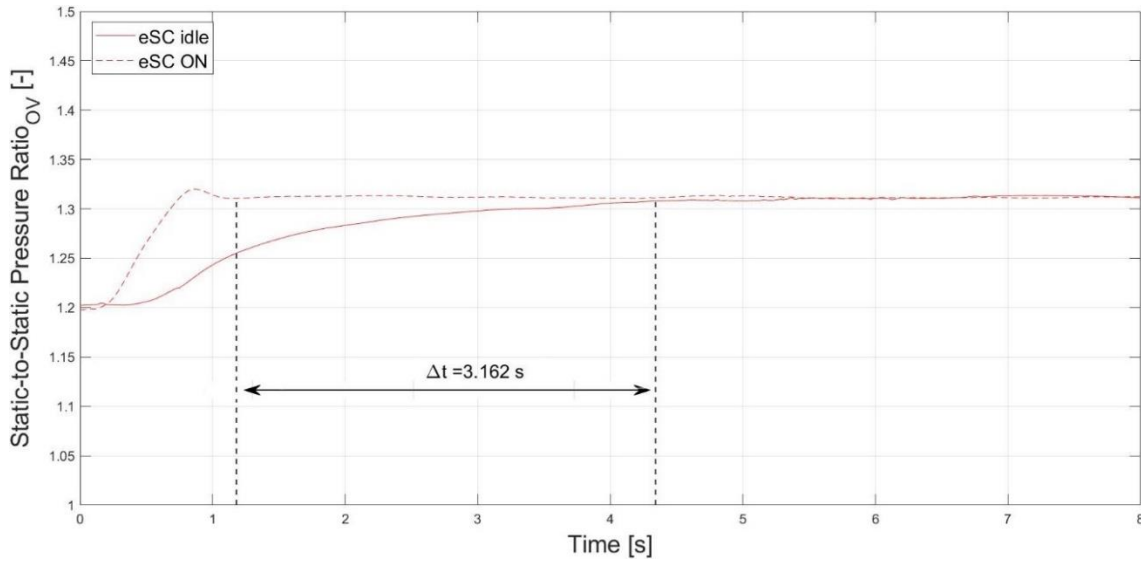
Figure 3.44 – Transient trend of the overall pressure ratio with and without the e-compressor activation

The last analysis reported here on the experimental characterization of the upstream layout transient response of the boosting system aims to highlight the path of the transient operation on the e-compressor map. The path can be divided into two parts: first the mass flow increases rapidly and then the pressure ratio increases to the value corresponding to the target rotational speed of 60000 rpm, in the case reported in Figure 3.45. A good agreement is evident in the level of rotational speed achieved during transient operation with respect to the steady state characterization. This result is very important for extending the $\lambda=1$ region of the engine map, a major challenge for modern spark ignition engines. A fast transient response with path like the one shown in Figure 3.45 avoids scavenging strategies. Scavenging strategies are usually adopted to improve the time-to-boost in turbocharged engines avoiding unstable operating condition of the compressor by increasing the air mass flow rate thanks to an increase in the overlap of the intake and exhaust valves; this method results in a lean air fuel mixture with a strong reduction in the conversion efficiency of the three way catalytic converter [72].
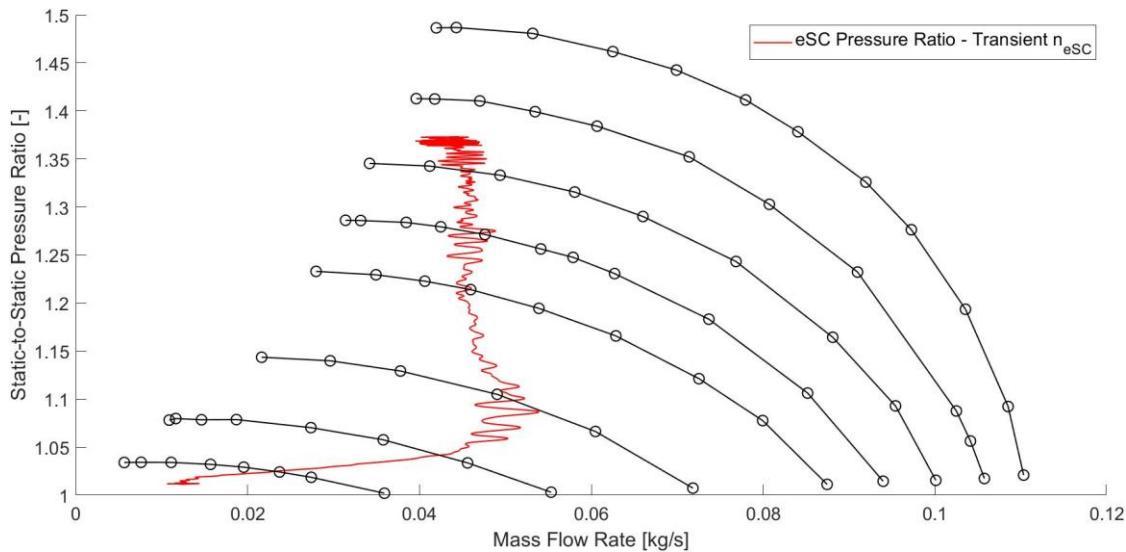

Figure 3.45 – Pressure ratio versus mass flow rate during acceleration on the e-compressor performance map

3.3.4 Experimental Campaign in Downstream Configuration

Similarly, to paragraph 3.3.3, in this section the layout and the main results of the experimental campaign carried out in downstream configuration will be presented.

3.3.4.1 Layout

As regards the downstream configuration, visible in figures 3.46 and 3.47, it can be immediately observed that it required a more complex set-up due to the plant constraints imposed by the laboratory and by the measuring stations. For this reason, a comparison between the response times of the 2 layouts will not be immediate, but the results will provide the basis for the 1D model described in chapter 4 which has precisely this objective. Therefore, a two-level configuration has been adopted: an upper one relating to the traditional turbocharger and a lower one for the e-compressor and the bypass valve.

Figure 3.46 – Overview of the test rig set-up in downstream configuration

Figure 3.47 – Overview of the test rig set-up in downstream configuration

Figure 3.48 shows the detail of the e-compressor installation in the downstream configuration; furthermore, the measurement stations of the component, the bypass valve and the refrigerant liquid pipes can be seen.
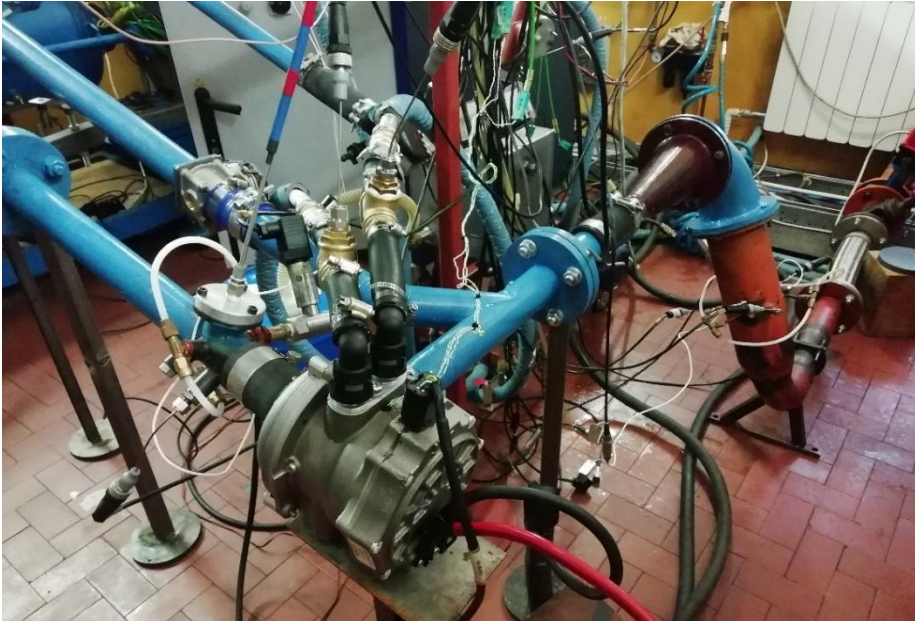
Figure 3.48 – Detail of the e-compressor installation in downstream configuration

3..3.4.2 Results

The tests carried out in the upstream configuration were similarly repeated in the downstream configuration; in this case the electric compressor is located downstream of the traditional compressor. Unfortunately, due to installation positioning issues, it wasn't possible to maintain the same lengths and volumes as the previous configuration, leading to not comparable time-dependent results.

In figure 3.49 the overall pressure ratio is plotted for different waste-gate valve position and in figure 3.50 the overall pressure ratio is plotted for different value of eSC rotational speed target. As in the upstream configuration a smaller value of the waste-gate valve opening or a higher value of the e-compressor rotational speed means that more energy is provided to the boosting system and therefore a higher pressure ratio at the compressor side.
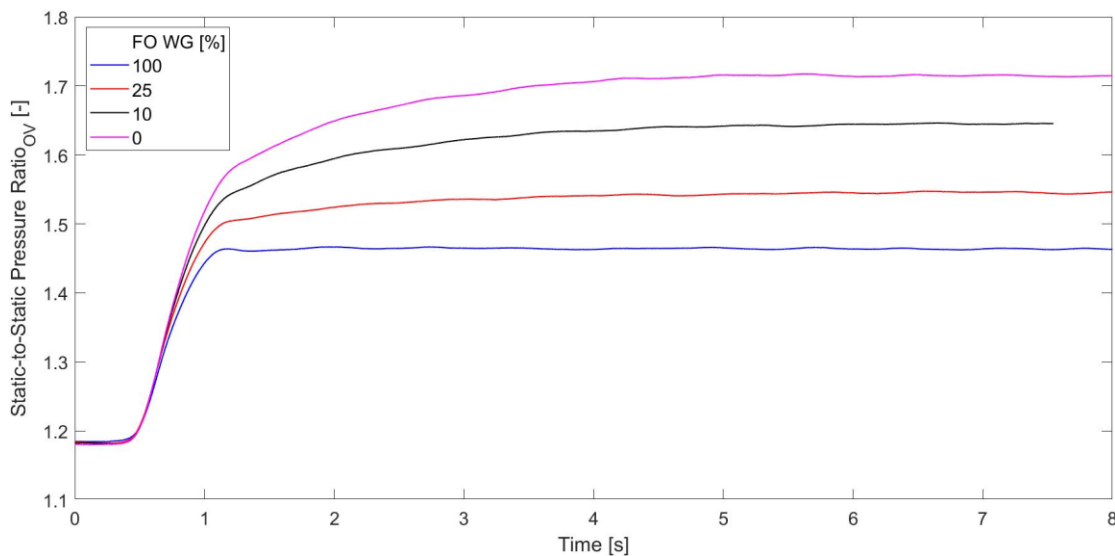

Figure 3.49 – Overall pressure ratio for different waste-gate valve positions
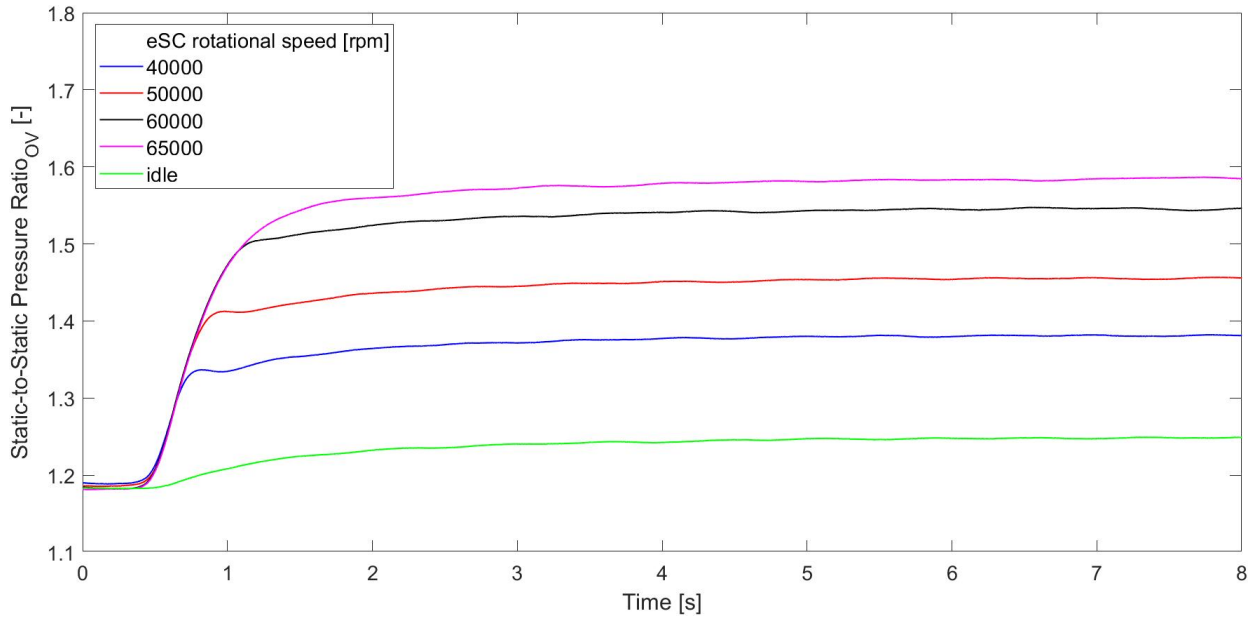
Figure 3.50 – Overall pressure ratio for different eSC rotational speed

The plot of the pressure ratio of the components shows no quantitative differences from upstream configuration. Refer to paragraph 3.3.5 for a more detailed comparison.

In figure 3.51 the transient response with and without the eSC actuation is reported. The downstream configuration seems to be a slightly worse in terms of time to boost (about 0.4 seconds) than the upstream one but must be pointed out that length and volume are increase significantly. A more detailed comparison in terms of time-to-boost will be addressed in chapter 4.
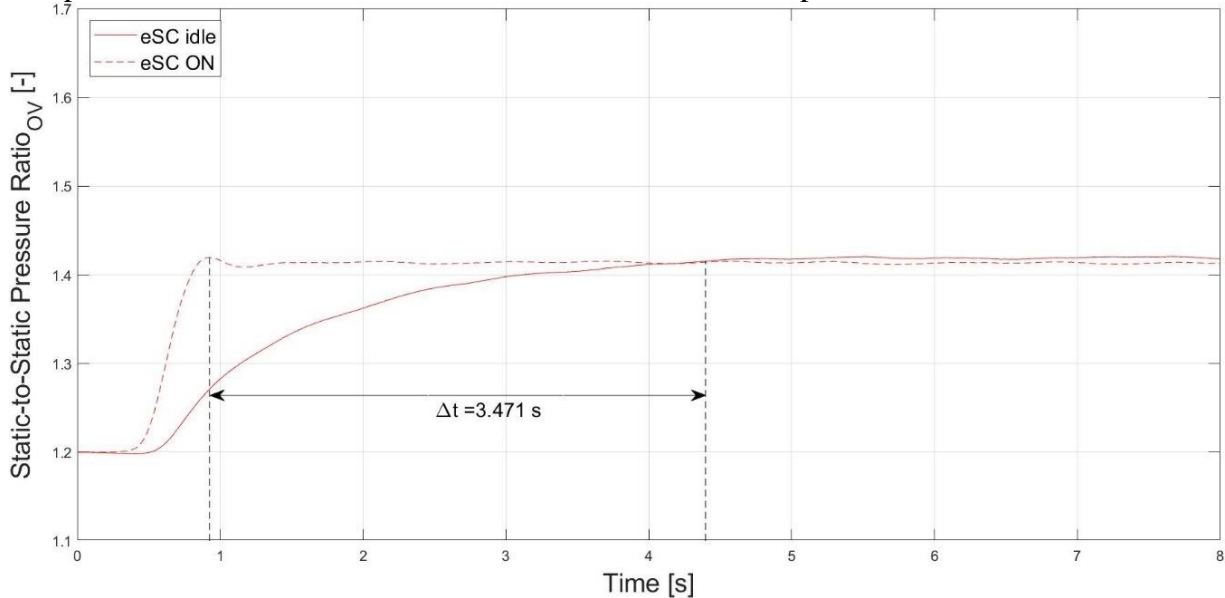

Figure 3.51 – Transient trend of the overall pressure ratio with (dotted lines) and without (continuous lines) the e-compressor activation

3.3.5 Upstream-Downstream Comparison

The comparison between the two layouts has to be split into two categories: overall performance in terms of system outlet pressure and transient response of the boosting system.

As previously stated, the not negligible difference in layout volumes makes it impossible to compare the two systems without introducing an error.

On the other hand, by analyzing the compression ratio of the e-compressor in the two different system configurations (reported in Figure 3.52), it can be observed how, with the same e-compressor rotational speed, different results are obtained. In the upstream case, at the compressor inlet there is air at ambient pressure, in the downstream case at the compressor inlet there is compressed air. The corrected rotational speed remains constant in both application, but the corrected mass flow rate (Eq. 3.3) decreases due to the increase of the inlet pressure. Therefore, moving on the same iso-speed if the corrected mass flow rate decrease the pressure ratio has to decrease as shown in figure 3.52.
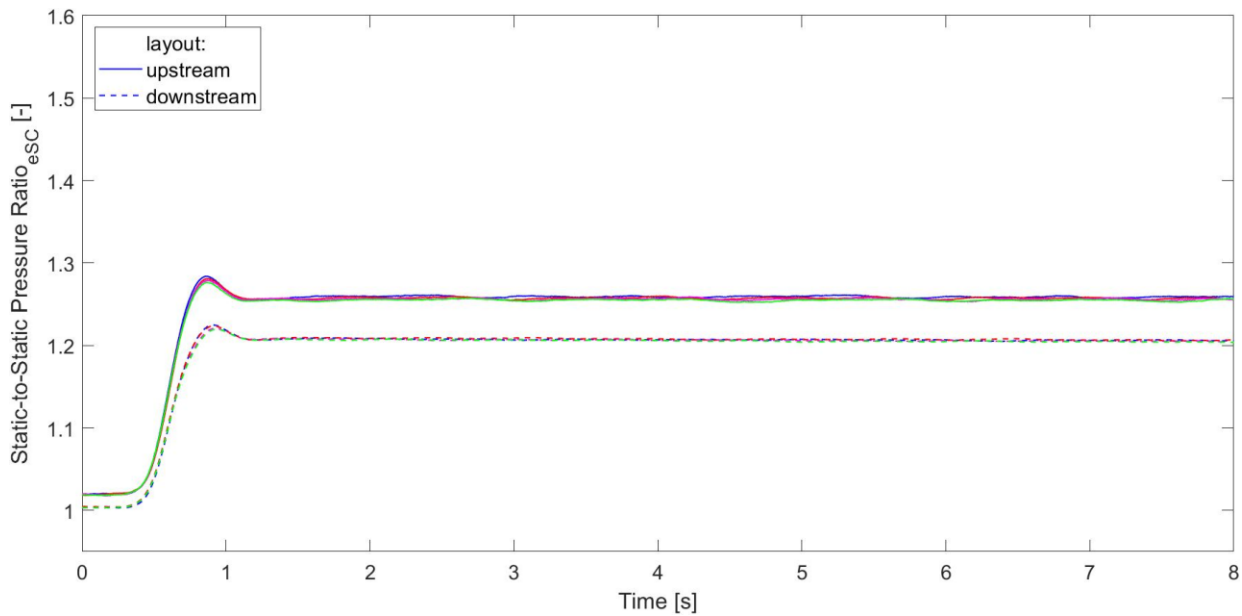

Figure 3.52 – e-Compressor pressure ratio comparison in upstream (continuous lines) and in downstream (dotted lines)

In Figure 3.53 the main turbocharger compression ratio in both analyzed configurations is presented. The turbocharger operating point is p=1.75 bar and m=0.03 kg/s, while the eSC speed is 50000 rpm. In the downstream configuration, at equal waste-gate valve openings, the compression ratio is higher since it is feeding fresh air at ambient temperature. Instead in the upstream configuration the inlet pressure is higher, causing a lower pressure ratio.
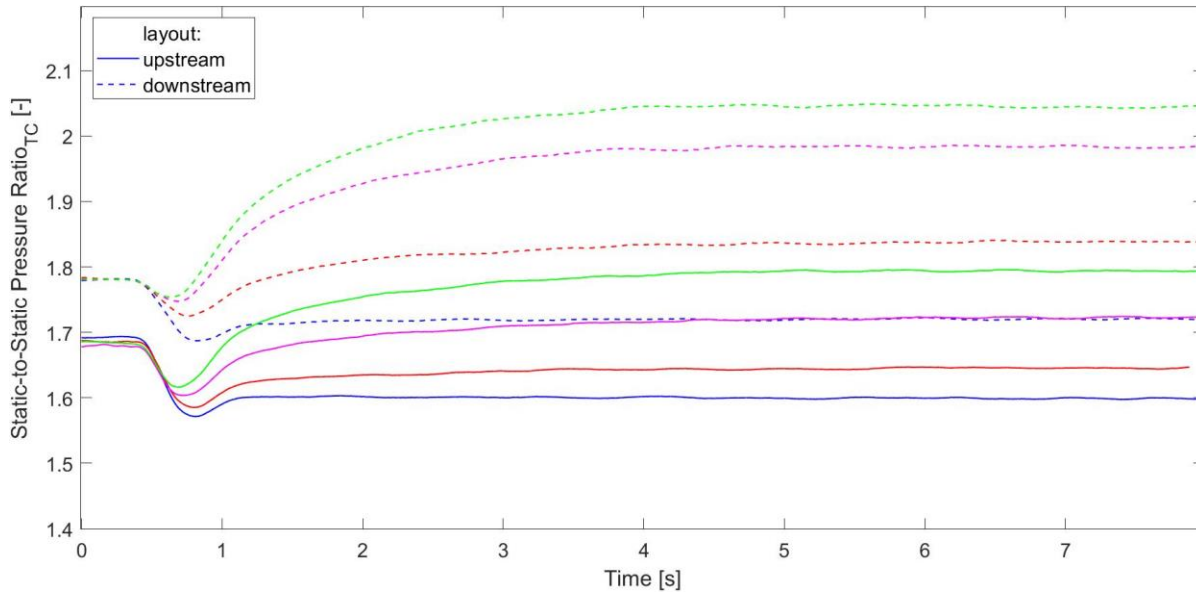
Figure 3.53 – Main turbocharger pressure ratio comparison in upstream (continuous lines) and in downstream (dotted lines)

Instead, by analyzing the overall pressure ratio, there are some noticeable differences between the two configurations. In figure 4.54 the comparison between upstream and downstream layouts is shown. The data was obtained with an eSC target speed of 40000 rpm and imposing a waste-gate percentage opening of 0%, 10% and 25%.

The performance of the downstream configuration is remarkably higher than the upstream one at all tested conditions. The reason for this difference has to be found in the higher energetical content of the flow entering the eSC since it has been previously compressed by the main turbocharger. and its control logic that fix the rotational speed to the desired target, and not the absorbed power.
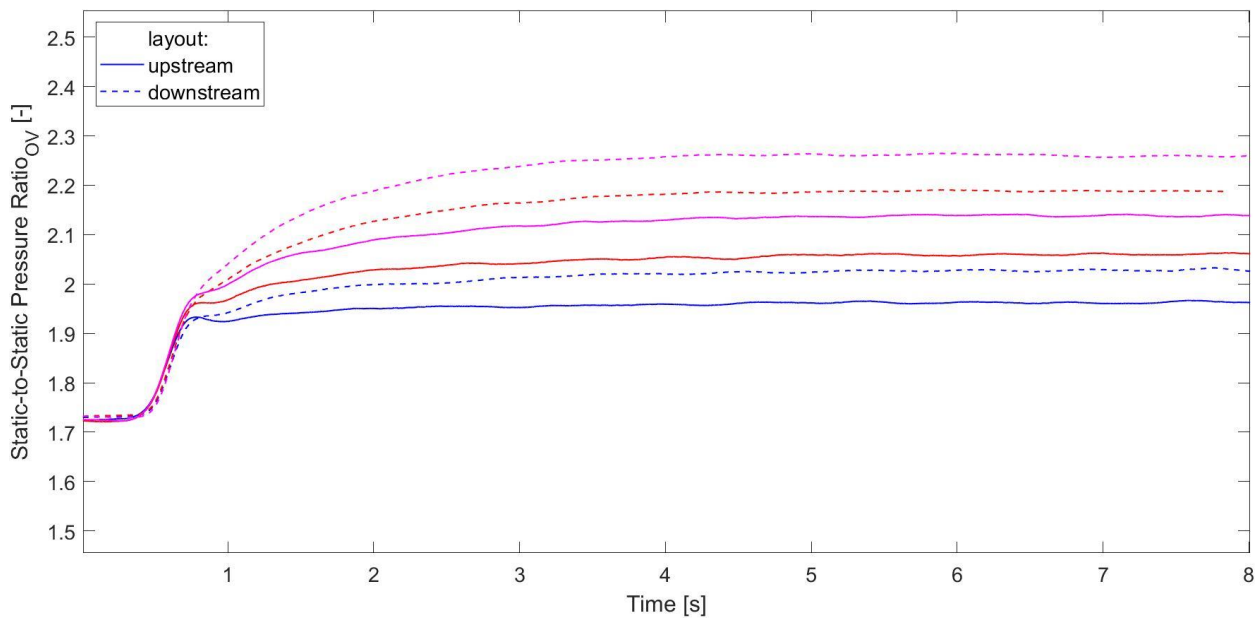

Figure 3.54 – Comparison of the overall pressure ratio in upstream (continuous lines) and in downstream (dotted lines)

4. 1-D Model

The aim of this activity is to create a tool that can replicate the testing facility results with a high degree of accuracy, becoming a reference for the further development of advanced models. As previously stated, the limiting factor of the experimental campaign is the impossibility of setting up an identical volume for the upstream and the downstream layouts, making the two configurations not comparable in terms of transient response. The flexibility and absence of physical constraints of a computer-based model allow redesigning the experimental layout, creating the possibility to compare the results.

The requirements to build such a model are precise experimental data to rely on, as well as an accurate characterization of all involved components.

The parts used in the following model that sought a high level of attention are both e-compressor and main turbocharger performance maps and the throttle valve installed at the downstream compressor outlet.

GT-Power is the market-leading engine simulation software developed by Gamma Technologies and is used by every major OEM for the design and development of their engines and components.

4.1 GT-Power description

GT-Power is part of the GT-Suite Solver, which includes dedicated models for the automotive electrical, braking, cooling, control, etc. systems, fully covering the engineering needs in the vehicle design and testing.

The software is divided into two main programs: GT-ISE, which is dedicated to the model construction, and GT-POST, which constitutes the actual solver and post-analysis tool.

At its core, the GT-Power solver is based on the 1D solution of the fully unsteady, nonlinear Navier-Stokes equations. The program is completed by adding thermodynamical and phenomenological model solvers to capture the effects of combustion, heat transfer, turbulence and engine and tailpipe out emissions [73].

This combination of solvers guarantees for great accuracy on both macro level quantities such as airflows, torques, etc., as well as acoustic studies or emission specie concentrations anywhere in the system.

In the following a brief overview of GT-Powers base workings will be made, especially pointing out the turbocharger-related models.

4.1.1 Conservation laws

The starting point for studying the process of internal combustion engines and any fluid-based energy system are the fundamental notions of thermodynamics, fluid dynamics and heat transfer, summarized by the conservation laws. The equations will be presented in the differential local form.

- Continuity Equation

$$\frac{\partial \rho}{\partial t} = -\nabla(\rho \vec{u}) \tag{4.1}$$

- Energy Equation

$$\rho c_p \left(\frac{\partial T}{\partial t} - \vec{u} \cdot \nabla T \right) = k \nabla^2 T + \dot{q} \tag{4.2}$$

- Momentum Equation

$$\rho\left(\frac{\partial \vec{u}}{\partial t} - \vec{u} \cdot \nabla \vec{u}\right) = -\nabla p + f + \mu \nabla^2 \vec{u} + \frac{\mu}{3} \nabla(\nabla \cdot \vec{u})$$

(4.3)

The fundamental equations form a coupled system of 5 nonlinear PDE in 6 variables. Further assumptions are therefore needed to complete the model. The constitutive relations are used to bind some of the variables in order to close the equations system. An example of it are the ideal gas law, the definition of specific heats, or a thermodynamic process equation.

4.1.2 Model discretization

Discretization is the splitting of the flow system into small sub-volumes to improve the model's accuracy. For each sub-volume the conservation equations are solved inside or at the boundaries of the volume itself, depending on where the required variables are stored. Figure 4.1 shows the location of the variables: scalar variables, being thermodynamic volume properties, are stored at the center of the sub-volume, while vector variables such as velocity or mass flux are stored at the volume boundary.
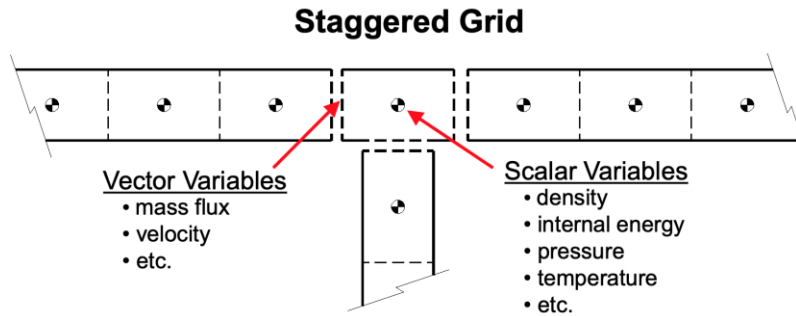

Figure 4.1 − Sub-volume discretization method

By determining the sub-volume dimensions, a compromise has to be made between model speed and accuracy. If smaller volumes are chosen, the model accuracy increases consistently. Note that beyond a certain limit, further reducing sub-volume size does not bring additional advantages, leading only to a longer computing time.
GT-Power provides guidelines to create a swift and accurate model, dividing it into a macro and a micro-level.
The macro level includes all physical objects such as pipes, bends, tapers, valves, and so on.
A new part has to be inserted whenever one of the following cases is presented:
- area discontinuity;
- bend;
- significant change in wall characteristics such as roughness, temperature, wall material or external heat loss.

The micro-level of discretization consists of splitting single macro parts into multiple sub-volumes. As previously stated, too smaller volumes can lead to long simulation periods without having real benefits. GT-Power suggests for example, in the case of an engine model for general performance analysis, the intake and exhaust systems discretization length has to be respectively 40% and 50% of the cylinder bore. In case of a detailed acoustics analysis the discretization length can be halved.
In the following thesis, 30 mm is the chosen discretization length.

74

4.1.3 Solution method

GT-Power model uses an explicit method to calculate the solution at each time step. The solution is based on the state of the system at the initial time t_0 and is calculated for a new time t_1 using the conservation equations. The new time must be close enough to the initial time to ensure the solution is stable and accurate, therefore a maximum time step is determined by applying the Courant method. The explicit solver remains stable by choosing its time steps such that the Courant number is less or equal to 0.8, where the Courant number is defined as:

$$COURANT\# = \frac{\Delta t}{\Delta x} \, (|u| + c) \qquad\qquad (4.4)$$

Where:
- Δt is the suggested time step [s];
- Δx is the discretized element length [m];
- u is the fluid velocity [m/s];
- c is the speed of sound [m/s].

The time step is calculated for each sub-volume and then the smallest one is then applied to the entire system.
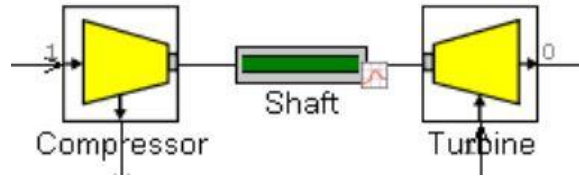
4.1.4 GT-Power turbocharger model

Figure 4.2 − GT-Power turbocharger assembly

The turbocharger is modeled by coupling three basic templates already present in the GT-Power library: compressor, turbine and shaft (shown in Figure 4.2). The program offers the possibility to extend the model complexity by adding a wastegate model, a variable geometry turbine model, or a twin-scroll turbine model. In the studied case, the model was kept at its simplest, defining only a compressor element with an imposed rotational speed. Therefore, only this component will be described from now on.
The compressor operating point is based on the performance maps generated from the steady-state flow test. The required data include speed, mass flow rate, pressure ratio and efficiency. The compressor map data must be entered into GT-Power in the "corrected" form, resulting in consistent input data to allow accurate comparison of points.
Speed and mass flow rate are corrected referring to temperature and pressure as shown in Equation 3.1 and 3.3.
GT-Power does not directly use raw map data for simulation, requiring it to be "pre-processed" before. During the preprocessing of the compressor map, the data is interpolated between the entered points and extrapolated to various speeds, up to rpm = 0 and pressure ratio = 1. An example of a pre-processed map is reported in Figure 4.3.
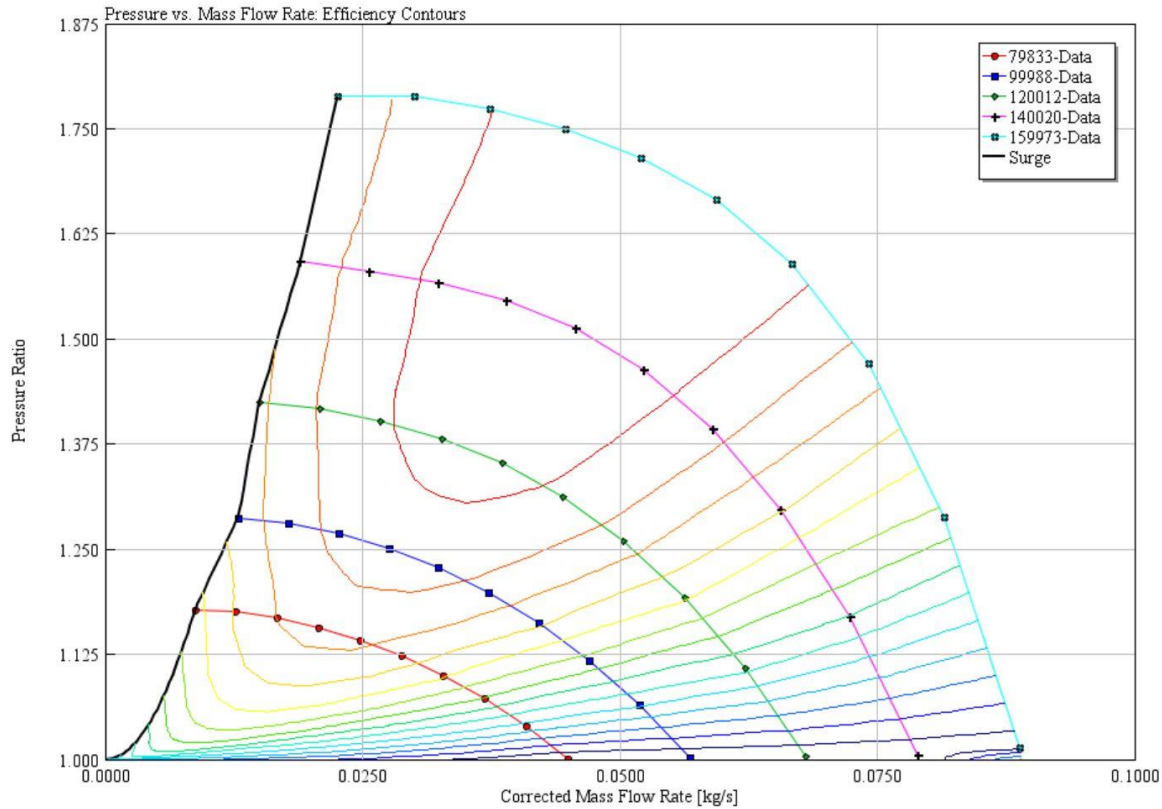
Figure 4.3 − BW preprocessed plot

4.1.4.1 Map processing during simulation

The component performance is determined from lookup maps. At each time step the program executes a series of commands to define the operational point of the machine.

The pressure ratio across the compressor is known from adjacent components and the corrected speed is also known from the attached shaft or speed boundary and the inlet temperature.

Mass flow rate and efficiency are determined from the map based on pressure ratio and speed and imposed, affecting the pressure ratio, the compressor power and speed for the next timestep.

The turbocharger speed is usually determined by evaluating the compressor and turbine power and the attached shaft inertia. In our case, the rotational speed was imposed and therefore not derived from the compressor map.

4.2 Definition and validation of the model components

4.2.1 Throttle Valve Characterization

The throttle valve regulates the compressor operating point and the absorbed power by changing the external characteristic of the circuit.

Its fluid dynamics function is therefore to link the pressure to the compressor outlet pressure and the mass flow rate. If this single component is poorly described, the whole model loses reliability, creating mismatching results between the experimental data and the modeled ones. Accordingly, to the presented assumptions, a test was conducted to characterize the valve.

The valve characteristic is expressed through the discharge coefficient c_d:

76

$$c_d = \frac{\dot{m}}{\rho \, A_{ref} \sqrt{\dfrac{2\left(p_{T,in} - p_{s,out}\right)}{\rho}}}$$

(4.5)

Where:

- $\dot{m}$ is the measured mass flow rate,
- ρ is the air density at the valve inlet,
- A_{ref} is the reference area,
- $p_{T,in}$ is the inlet total pressure,
- $p_{s,out}$ is the outlet static pressure.

This expression is derived by relating the actual mass flow rate to the mass flow rate discharged by an ideal nozzle which expands at the same inlet ad outlet conditions.

In Figure 4.4 the experimental setup is shown. The common system layout has been modified bypassing the turbocharger and therefore directly connecting the compressor feeding line with the relative outlet. This configuration allows taking advantage of the preexisting line to feed the valve with an arbitrary mass flow rate, which is regulated with the installed pressure reducers.

The mass flow rate is acquired with the already installed thermal mass flow meter, described in paragraph 2.2.5.3. The inlet pressure and temperature are measured using the usual turbocharger outlet measurement station, commonly referred to as Station 2 and enlightened in the picture with a green circle. The outlet pressure is acquired through the pressure station installed on the compressor outlet line.
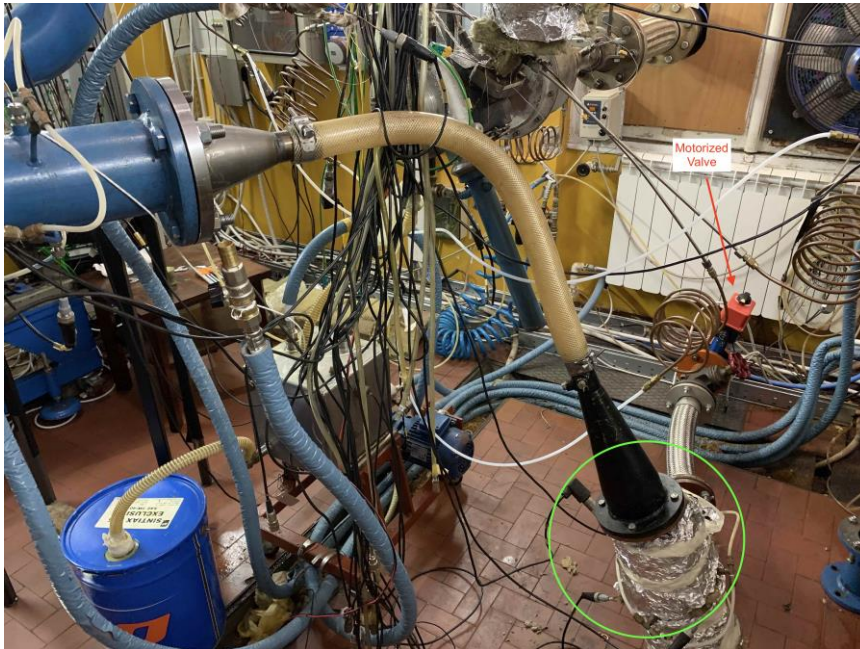

Figure 4.4 – Experimental layout

The acquisition has been carried out by regulating the valve inlet pressure and by gradually closing the valve. For each valve angle has been made three different measurements that were averaged afterwards.

Particular attention has been paid to the pressure level at each opening angle, tying to maximize it in order to reduce the measurement error as far as possible.

Following the error propagation theory, the uncertainty of a general function is:

$$\delta f = \sum_{j}^{k} \left| \frac{\partial f}{\partial x_j} \right|_{x_j = x_{j0}} \delta x_j \tag{4.6}$$

If applied to the discharge coefficient equation, it shows a strong dependence from the pressure error, especially for high opening angles. This tendency is attributable to the installed pressure transductor, which has a fixed error on the full-scale of 0.1%. When the valve is near the fully open position the pressure in the piping is next the atmospheric one, leading to a measured relative pressure close to zero. Therefore, the fixed error of the sensor has a major influence on the measure itself.

The testing facility is equipped with many relative pressure sensors with full scale varying from 0.35 bar to 4 bar. The 0.35 bar ones could be the best candidate to be used in this measure, but as the valve closes the inlet pressure has to consequently rise to have enough high mass flow to not incur in an error increase at the thermal mass flow meter.

The chosen pressure transductor has a full scale of 2.5 bar, allowing a modest error with the opened valve and enough high scale to measure up to 80° of valve closing.

The resulting discharge coefficient is plotted in Figure 4.5 as a function of the valve angle. Note that 0° corresponds to a fully open valve condition.

The number of acquisitions was thickened towards the highest angles because it is the usual operating range of the studied system and therefore the highest resolution is mandatory.
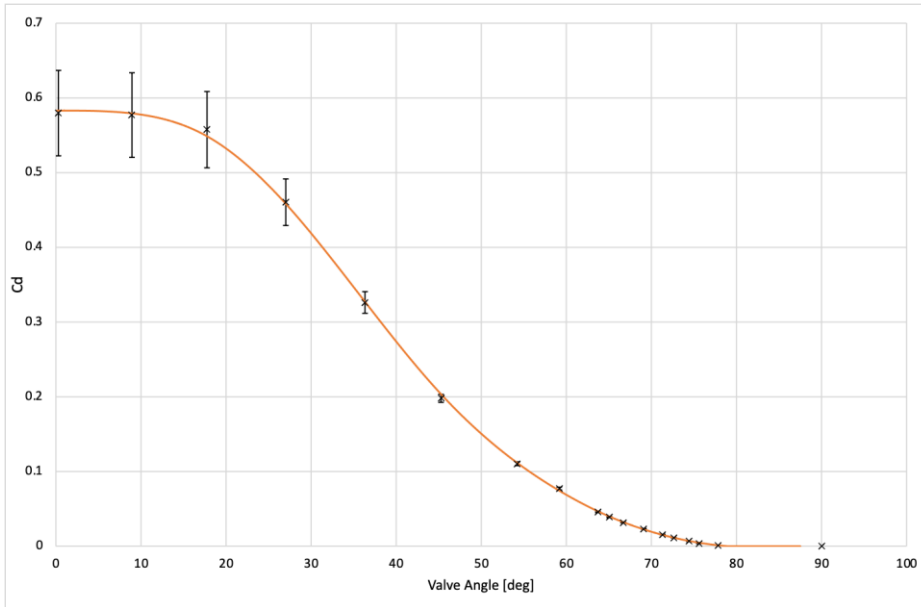

Figure 4.5 – Discharge coefficient - valve angle

4.2.2 Main Compressor and e-Compressor Performance Maps Validation

Before building the actual upstream and downstream models, the traditional compressor and the eSC performance maps were tested with a dedicated model. This step was necessary to uncover possible

mistakes that occurred during the performance map fitting or data corruption during the actual map acquisition at the testing facility. The model came also in hand to test and verify the butterfly valve characterization.

Two identical models, one each for every component, were created since the compressor outlet line was the same during both turbocharger's map acquisition campaign. An example is shown in Figure 4.6.
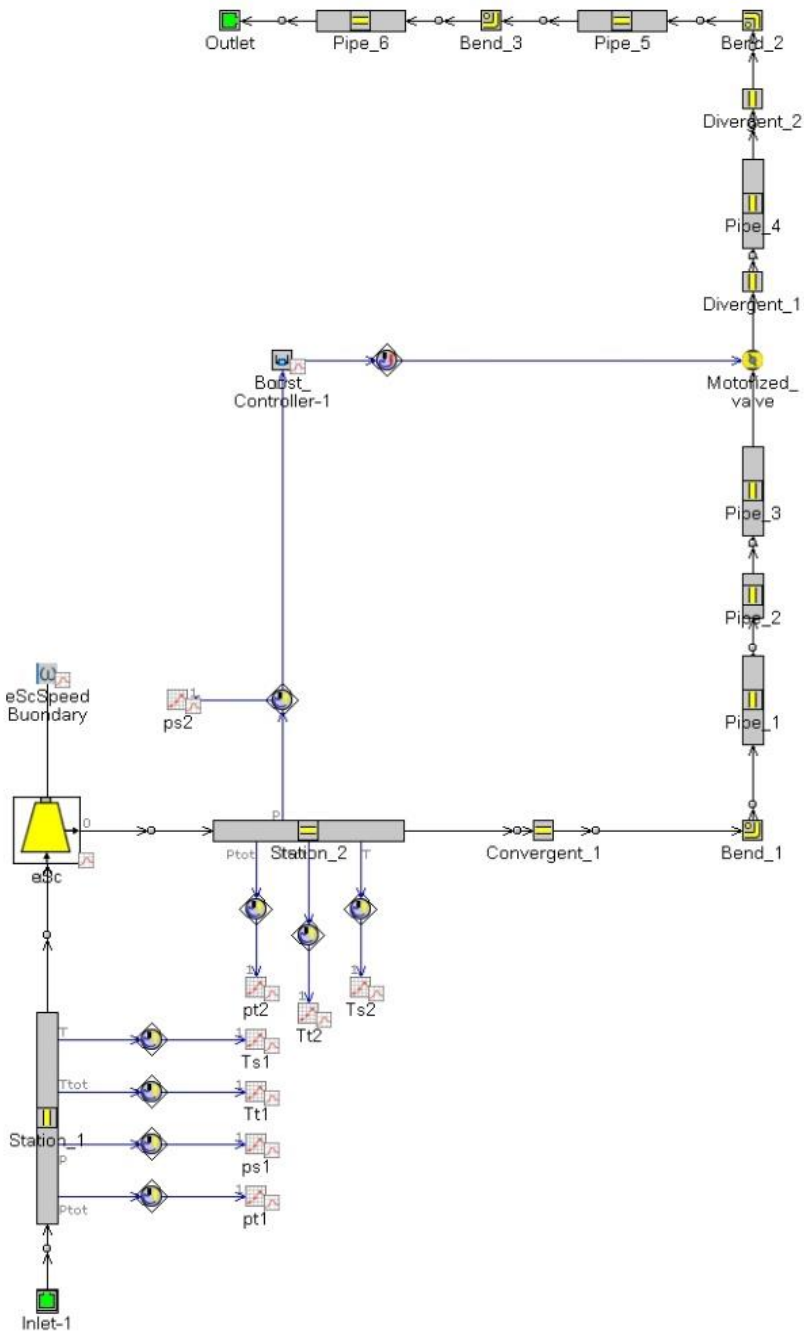

Figure 4.6 – Performance map testing model

The model is mainly composed of the compressor outlet line with the adding of the upstream compressor measuring station, Station 1. The compressor feeding line was not included since its dimensions and volumes are not significant for this step.

The pressure losses are also neglected because the measuring stations used during the throttle valve characterization are installed at both ends of the line and therefore the characterization itself contains implicit information about the section losses.

As system inlet boundaries are set the static pressure and total temperature, measured at Station 1 during the testing. The outlet boundaries are defined with the atmospheric pressure and ambient temperature.

In the compressor component, indicated in Figure 4.6 as "eSC", is loaded the performance map, along with information about the reference data used to define the corrected values.

The map preprocessing is automatically carried out by the program, but to ensure good quality is better to previously perform a map fitting since the experimental data are usually not consistent through all constant speed curves and also no information about the preprocessing goodness is given.

The map verification is carried out similarly as the map acquisition during the experimental activity. The motorized valve is moved by a PID controller who measures the static pressure at Station 2 and compares it to the target one, regulating the valve angle accordingly to the generated error signal. The target conditions are of course the ones acquired during the experimental activity. The simulation for each operating point runs until the error between the target pressure and the imposed one is lower than 0.01%.

The results of a complete map verify is shown in Figure 4.7. The Figure presents a comparison between the data acquired in the testing facility, indicated with a dot, and the relative model result. Moreover, for each experimental data the measurements uncertainty bars are reported to ensure that the modeled counterpart is within a delimited boundary.

As shown in the Figure, a slight mismatch between calculated and measured data especially for the operating points located near the surge line. This disagreement is caused by several aspects, including the curve slope, the measurement error during the valve characterization and the not perfect curve fitting. The curve slope near the surge line is almost null or even positive. This means that for slight variations of the pressure, the mass flow rate, and therefore the operating point, can change drastically. Adding this condition to the tiny but unavoidable measurement error introduced in the valve characterization, brings to a certain degree of uncertainty when operating the pressure ratio to obtain the desired operating point. Furthermore, also a slight variation in the curve fitting can lead to a non-negligible error, especially if combined with the previous considerations.
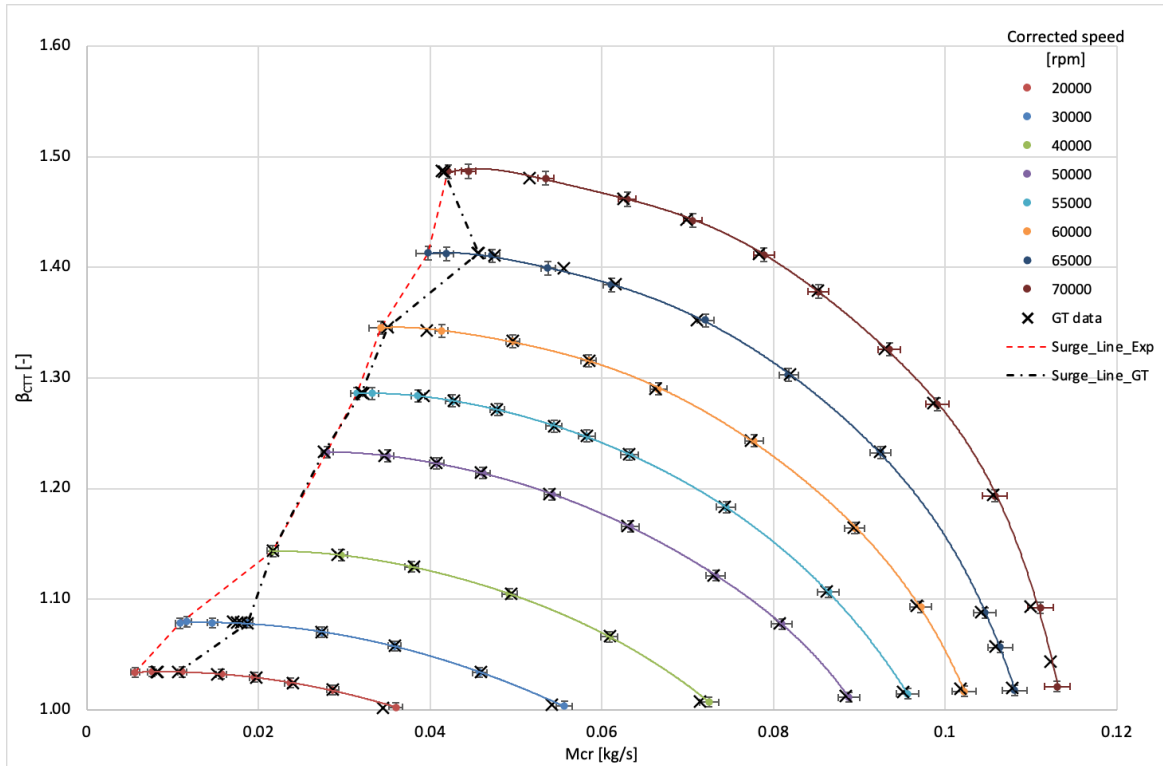
Figure 4.7 – Check results on e-compressor map

As the curve slope is the most difficult problem to overcome, requiring the absolute perfection in terms of curve fitting and valve modeling, a second method has been introduced to overcome this obstacle. Instead of chasing a target pressure, the PID is set to match a target mass flow rate. In this case, the curve slope is strongly supporting the model accuracy, leading to tiny errors in pressure ratio even with a not accurate mass flow input.

The results on both performance maps using this method are in good agreement, showing pressure ratio errors below 0.5% compared to the acquired data.

The following figures (4.8 and 4.9) show the model goodness of both e-compressor and main compressor pressure ratio-corrected mass flow rates maps.
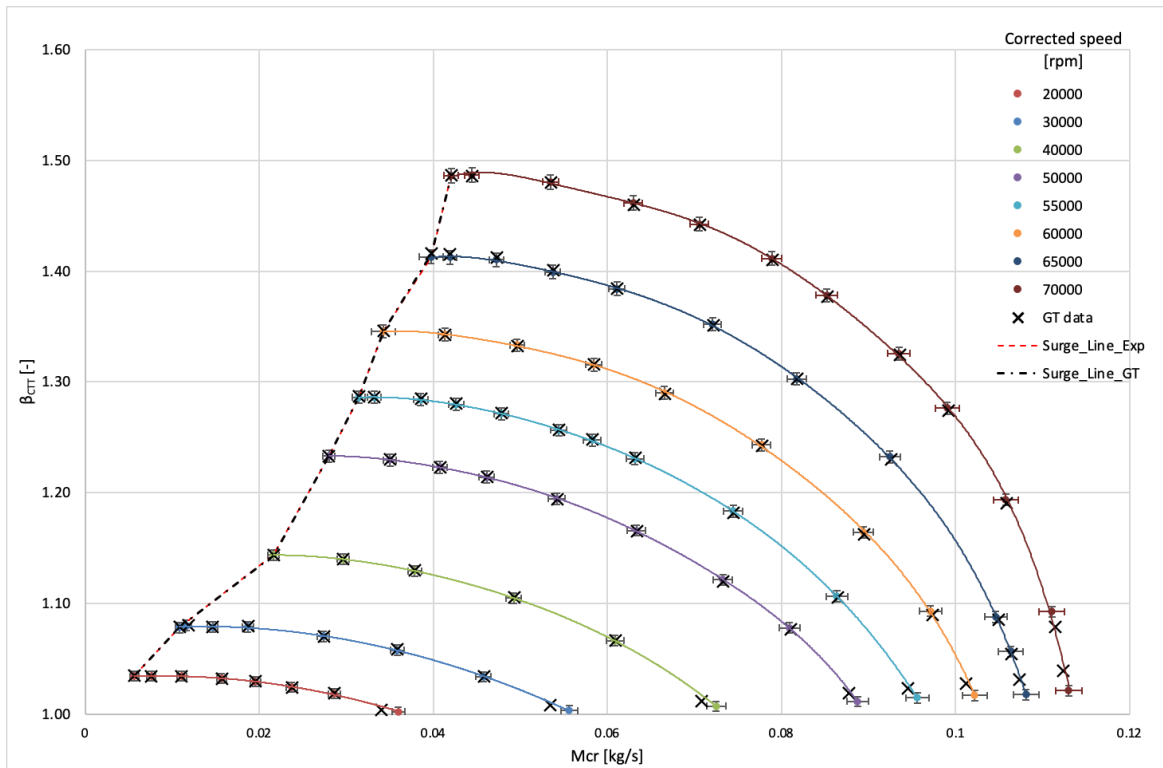
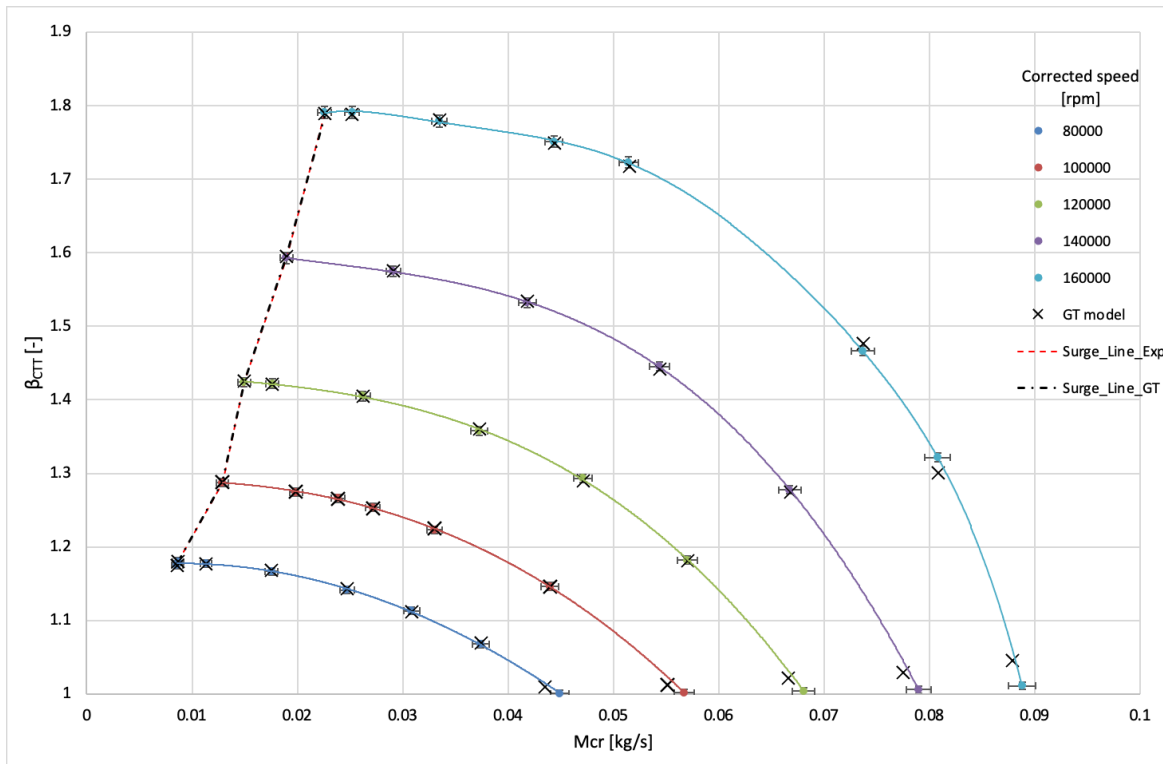*Figure 4.8 – e-Compressor performance map check with mass flow rate targeting*

Figure 4.9 – Main compressor performance map check with mass flow rate targeting

Once the pressure ratio and the mass flow rate were proved to be accurate for each operating point, the maps were refined by adjusting the efficiency multiplier to have also good degree of precision on the outlet temperature. A 0.98 multiplier was set for both maps, guaranteeing an error equal to ± 1°C.

4.3 Upstream model

The model is built following the dimensions of the UNIGE testing facility to ensure that the system transient response of the acquired data and the modeled one is comparable.

The materials and their properties are defined through the GT-Power libraries, as well as the air composition. The measurement stations are placed exactly in the same position as in the testbench, especially to avoid mismatching temperature due to heat transfer.

Since the experimental campaign was not specifically performed with a model activity in mind, some data were not acquired in the first place and therefore a few simplifications are taken in the model development.

The inlet boundaries are set to the total pressure and temperature acquired at the Station 1'. It was not possible to assume the ambient pressure as the inlet boundary because as the layout was installed in the testing lab, no friction losses evaluation was carried out.

The inlet section of the layout up to the Station 1' is therefore modeled with the absence of pressure losses. In the section between the e-compressor and the main compressor the pressure losses are also neglected for the same reason. Even if this approximation is not preferable at the e-compressor outlet, since it could modify the operating point of both e-compressor and main compressor, the layout dimensions suggest that the expected losses are indeed negligible.

The bypass valve characteristic is also unknown, but, accordingly with his purpose during the tests, his properties are not strictly essential. It is modeled with a linear characteristic, with a loss coefficient of 1 at the fully open position and is assumed that in the fully closed position forms a perfect seal. In Figure 4.10 the bypass valve discharge coefficient is presented.
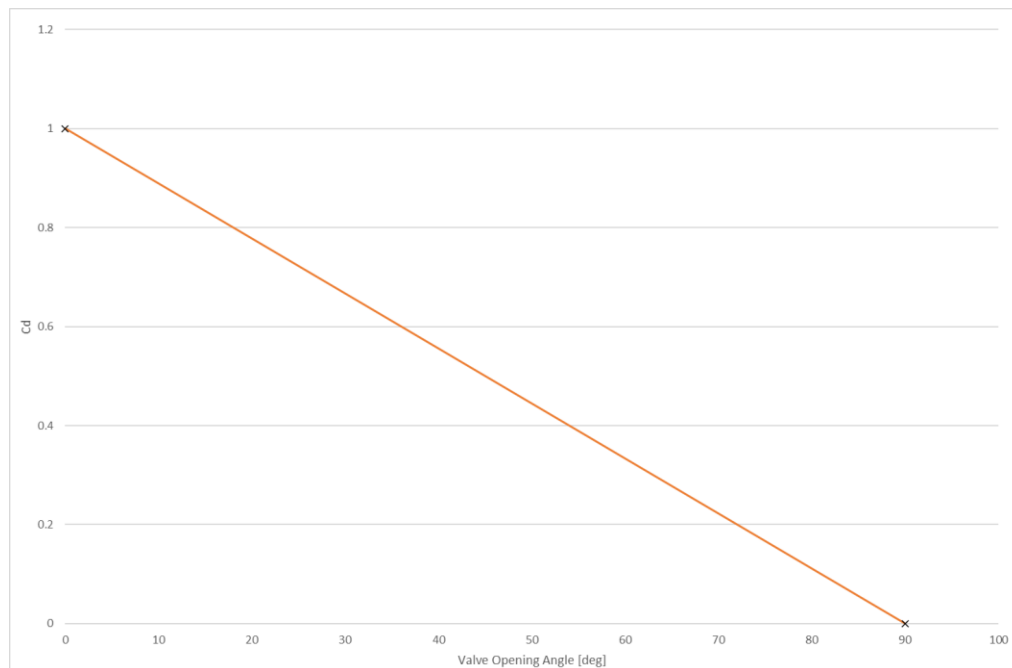

Figure 4.10 – Bypass valve discharge coefficient

The outlet section is the same as the one used to characterize the motorized valve downstream the main compressor. In Figure 4.11 is shown the complete upstream configuration model.
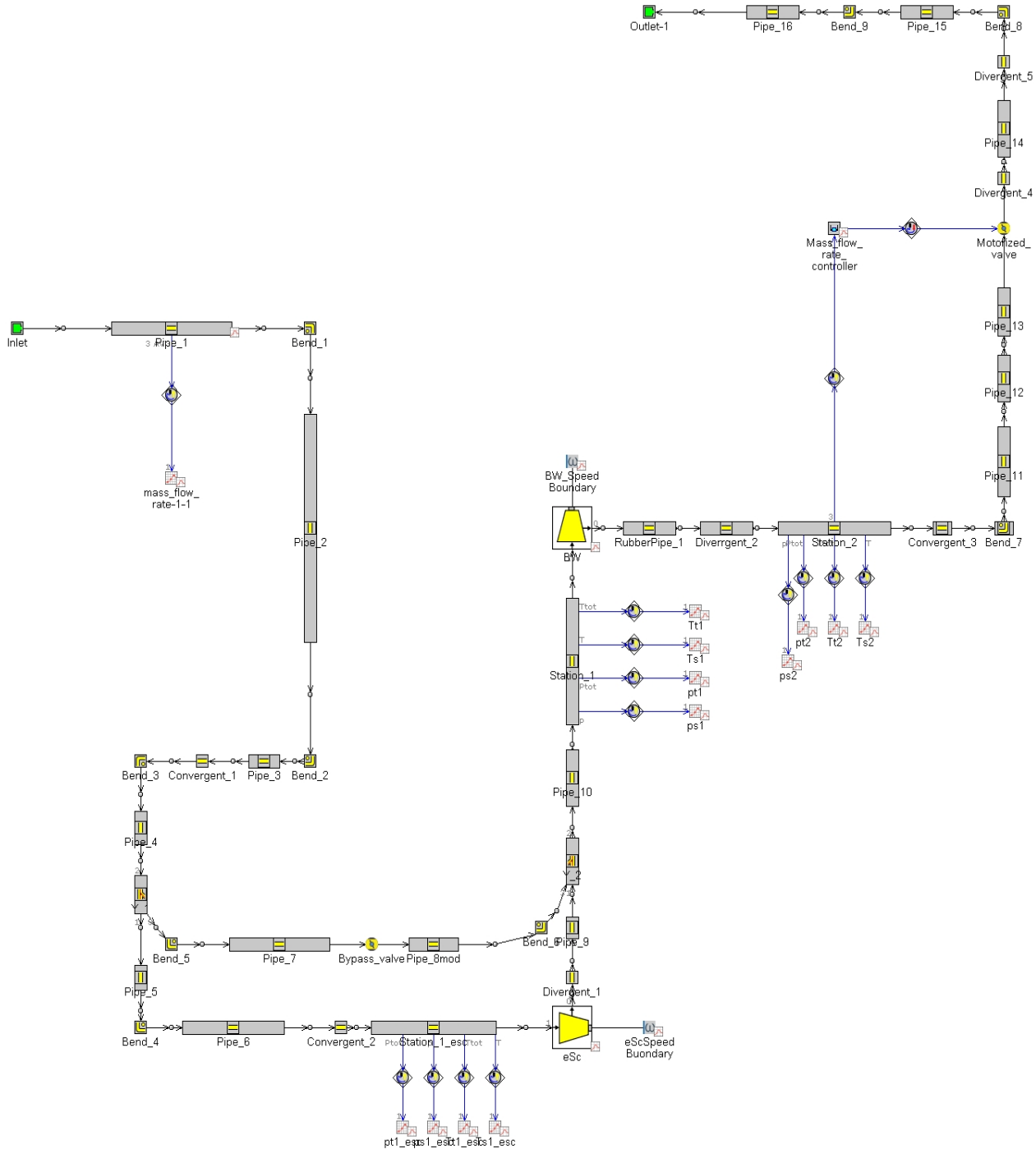

Figure 4.11 – Upstream configuration model

4.3.1 Upstream model validation

Before testing the system transient response, the model is checked to ensure that all pressures, temperatures and mass flow rates are replicating the testing lab results. Since all the data acquired during the campaign are derived from a transient response, only the end of run results, which correspond to a steady state of the system, are taken as reference.

Note that in this condition, according to the high response transductors data, the pressure and the mass flow rate values are indeed steady by the time of the data acquisition.

The validation is carried out by imposing a target mass flow rate to the PID controller which operates the valve. The valve position is stored and then applied to the relative transitory tests. The resulting pressure levels are used in this case as verification parameter. To ensure a high-quality model, all the experimental points are taken as reference.

In Figure 4.12 is presented a comparison between the UNIGE operating points and the GT-Power model ones. The data are relative to the main turbocharger operating point with $p_2 = 1.51$ bar and $M_c = 0.026$ kg/s. The points are figured on the main compressor performance map to show the ability of the model to follow the testing facility data trough different operating conditions. A little error is still accepted because of the difficulties faced in the temperature measurement during the transitory, as well as the pressure and mass flow instrumental measurement errors.
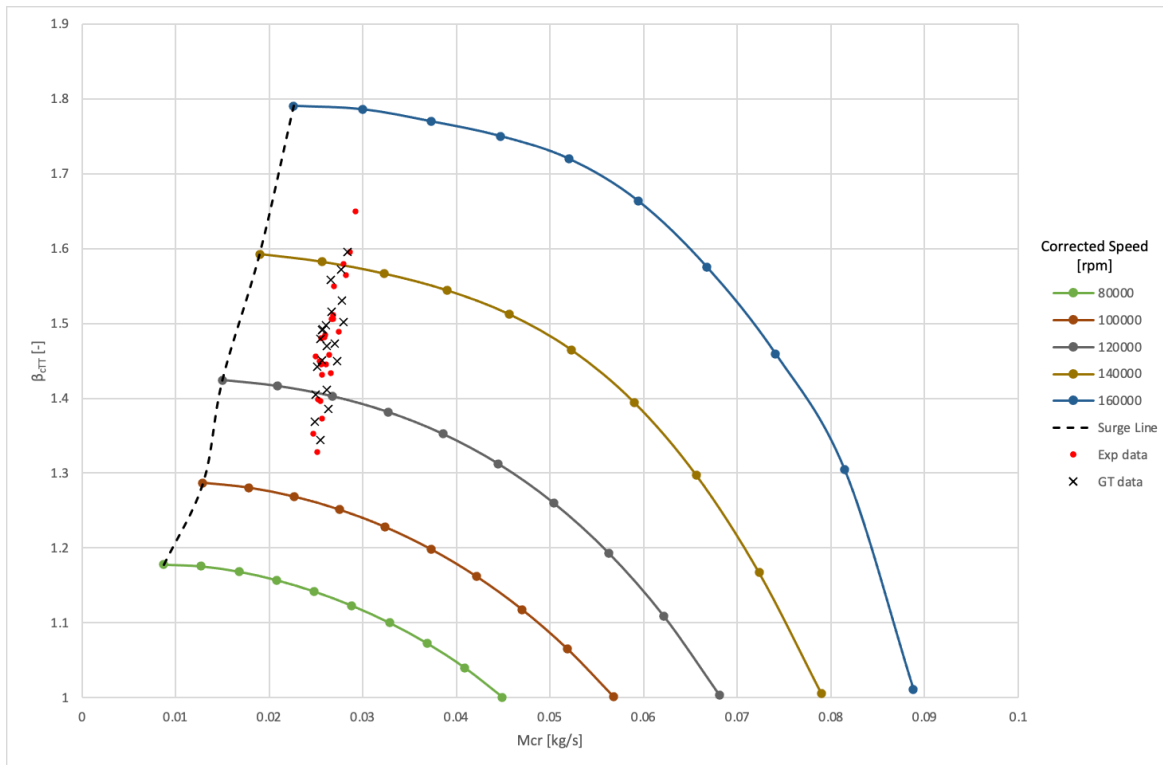
Figure 4.12 – Upstream model operating points

4.3.1.1 Heat transfer

The validation procedure is also used to determine the heat transfer in the section located between the e-compressor and the main compressor and the one downstream between the main compressor and the measuring Station 2. Without a correct heat exchange model, the flow temperature at the inlet of the main compressor would be incorrect, leading to an incorrect evaluation of the pressure and therefore to a bad

interpolation of the characteristic curves. The error will eventually spread also to the Station 2, leading to unrealistic pressure and temperature conditions.

Unfortunately, the thermistors used during the experimental campaign are characterized by a low frequency response, therefore the temperature measured during the transitory could not be accurate. During the model calibration this handicap is taken into account by considering the results between an error of ±2°C as valid.

The Nusselt equation for turbulent heat transfer, presented in Equation 5.3, is taken as reference.

$$Nu = 0.036 \, Re^{0.8} \, Pr^{0.3} \tag{4.7}$$

The constant term is than modified carrying out a parametric study during the validation to match the measured temperature.

At first only Station 1 is considered and the heat transfer equation is corrected with a factor of 1.4, leading to a constant term of 0.05. Once a correct main compressor inlet temperature is imposed, the section downstream the turbocharger is then studied and the Nusselt equation applied to this part is corrected with a factor 2.5.

4.3.2 Upstream model in transient conditions

In the experimental campaign the transitory is produced by regulating the waste-gate position and the e-compressor target speed. However, in order to replicate the same procedure in the model, a full knowledge of the dependence of the turbocharger turbine characteristic from the waste-gate position would be necessary. Being this type of data not available, the speed acquired during the experimental campaign is directly imposed to the main compressor.

During the testing to the motorized valve is imposed a predefined angle, which is evaluated during the model validation run by averaging the resulting angle from the main compressor operating point stationary runs. This procedure emulates the one used in the testing laboratory, but it also introduces a minor error to the starting and ending pressure due to the valve characteristic curve uncertainty.

The bypass valve is closed simultaneously with the start of the e-compressor speed ramp, taking 0.15 seconds to pass from the fully open to fully closed position.

4.3.2.1 e-Compressor speed controller

During the experimental tests, to the e-compressor has been given a target speed by the user, but the actual control is assigned to the internal e-compressor logic of which no data or knowledge is available. The first tests were made by imposing a linear speed ramp. This assumption resulted too simple and not able to replicate the pressure behavior at all different speed ramps. Therefore, to ensure that the pressure trend is well matched, it is assumed that the e-compressor controller is a PID type. In the GT-Power library there is already a PID component, which requires as input the controller characteristic coefficient and other data such as the target signal and the maximum speed ramp. The target speed is imposed accordingly to the conducted test and the maximum speed ramp is set to 400000 rpm/s^2 as indicated by the manufacturer.

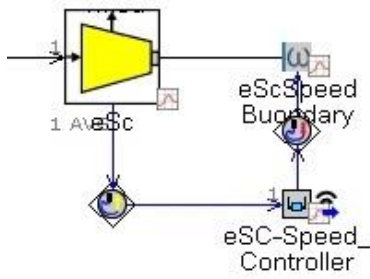In figure 4.13 is shown the e-compressor speed controller assembly.

Figure 4.13 – PID controller assembly

The speed signal is acquired directly from e-compressor and sent to the controller, which provides an input signal to the e-compressor speed boundary.

The controller calibration is done by setting the proportional, integral and derivative gains as variables and varying it parametrically. As target signal of the calibration is set the transient pressure at the station 2. Using a signal derived from the actual speed is not the ideal procedure to ensure an optimal calibration, but the eSC speed was unfortunately not acquired during the tests on which this thesis is based. Future experimental activity will be set to acquire the actual e-compressor speed and the PID calibration will be corrected.

Several combinations of the three parameters were tried in order to predict the parameter influence on the outlet pressure as shown in Figure 5.13. In this case the reference test characteristics were initial pressure 1.51 bar, waste-gate fully open and e-compressor target speed 50000 rpm.
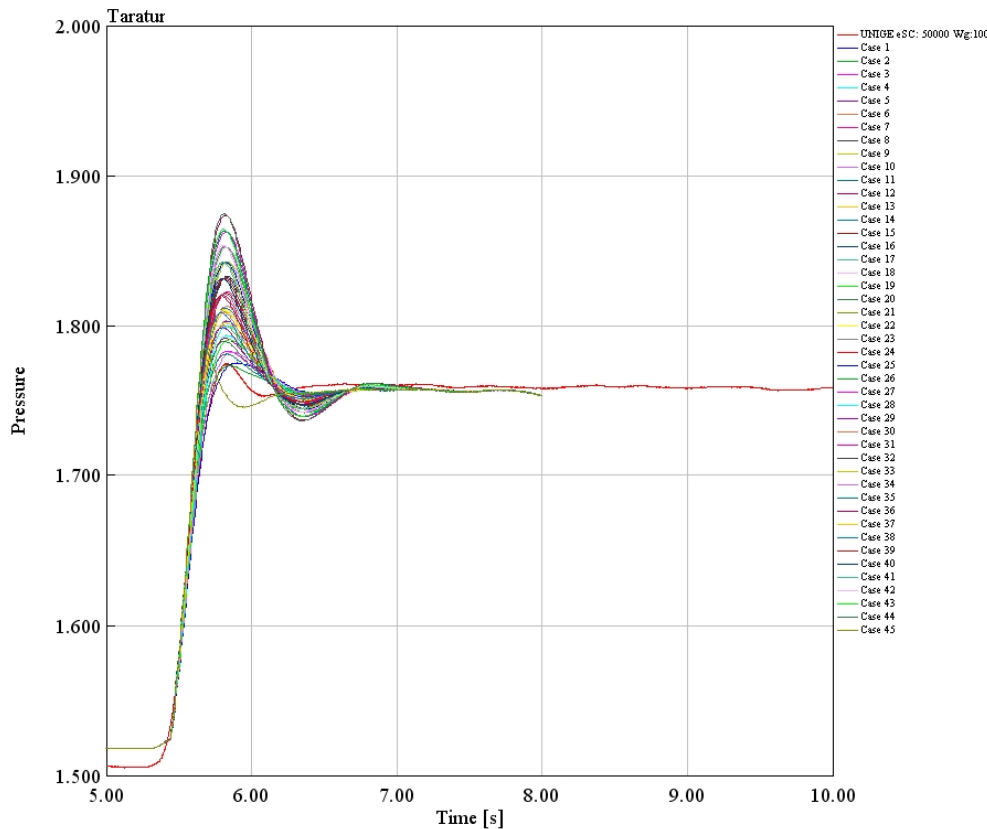

Figure 4.14 – Iterations for PID calibration

Eventually the combination reported in Table 4.1 has turned out as ideal for the studied condition.

Proportional Gain	0.75
Integral Gain	10.5
Derivative Gain	0.15

Table 4.1 – PID coefficients

However, during the validation of the new coefficients on a different operating point with an e-compressor target speed of 60000 rpm, the resulting pressure trend showed a mismatch between the experimental data and the modeled ones. The results shown in Figure 4.15 denote an excessive pressure curve slope of the modeled data, meaning that the e-compressor imposed acceleration is too high.
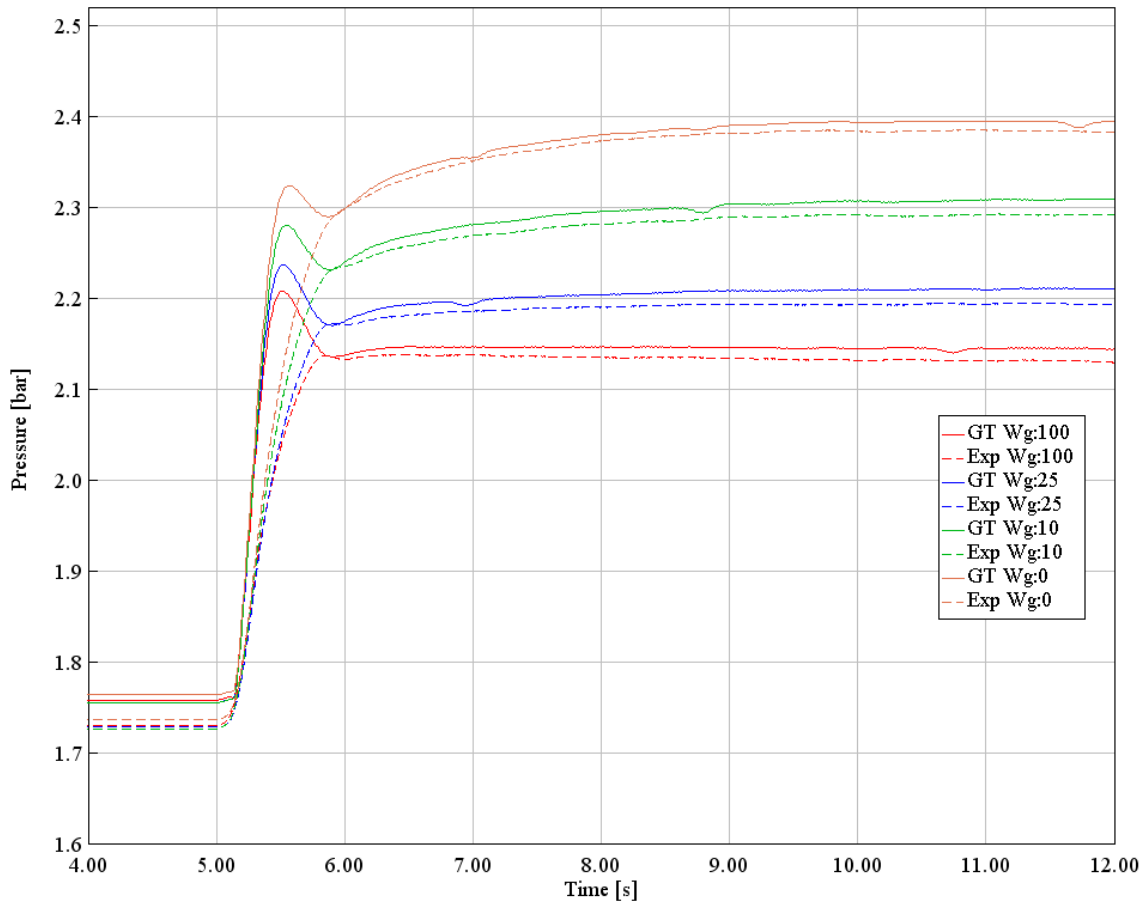
Figure 4.15 – Outlet pressure trend with wrong PID set-up

Therefore, further investigation has been conducted, varying the PID coefficients by starting from the previously obtained ones. This procedure has been applied to tests with an e-compressor target speed of 40000 rpm and 60000 rpm. A linear dependence of the proportional and derivative coefficients of the PID from the target speed is detected: the e-compressor controller evaluates the maximum speed slope

88

depending on the imposed speed, reducing it for increasing values. The following equations (4.8 and 4.9) present the coefficients dependence from the e-compressor target speed.

$$proportional\ gain = \ -0.000005 * n_{target} + 1 \tag{4.8}$$

$$integral\ gain = -0.00045 * n_{target} + 33 \tag{4.9}$$

These equations are applied to all presented results, showing the goodness level of the PID calibration.

4.3.3 Upstream model results

In this section a comparison between the modeled transient response and the acquired one will be presented. The parameter used as reference is the static pressure at the system outlet, commonly referred as p_{S2}. All experimental conditions have been tested giving optimal results, but only a few will be here presented.

The Figures 4.16-18 show the results of the first test typology, whose testing procedure is fully explained in chapter 3. Starting from the chosen main turbocharger operating condition, the e-compressor is commanded to accelerate to a certain speed. For each speed the waste-gate valve is moved to different positions, going from fully open (100%) to fully closed (0%). A smaller closing angle causes a higher mass flow to evolve in the turbine which increases the machine power output, providing a boost to the compressor therefore causing a higher output pressure.

The starting pressure, as well as the ending one, slightly differ from the experimental data. The error source is to be found in several aspects like the valve discharge coefficient, which is inevitably affected from an instrumental error, or the zero pressure loss assumption. However, the difference is of the same order of magnitude (hundredths of bar) of the measurement error of the experimental data, therefore the results are highly acceptable.

Moreover, as figures 4.16-18 show, the modeled pressure spike at the end of the ramp is not perfectly matching with the experimental one. By analyzing the measured pressure data, this fluctuation's cause is to be found in the e-compressor speed ramp since for increasing speeds the spike tends to flatten out and eventually to disappear, as it has been noted while calibrating its PID controller. Nevertheless, being the calibration based on a parameter deriving from the speed and not on the e-compressor speed herself, it is fair to assume that the procedure is affected by an inherent error. An experimental activity aimed to measure the instant e-compressor speed during a transitory is mandatory if a more precise model is needed.
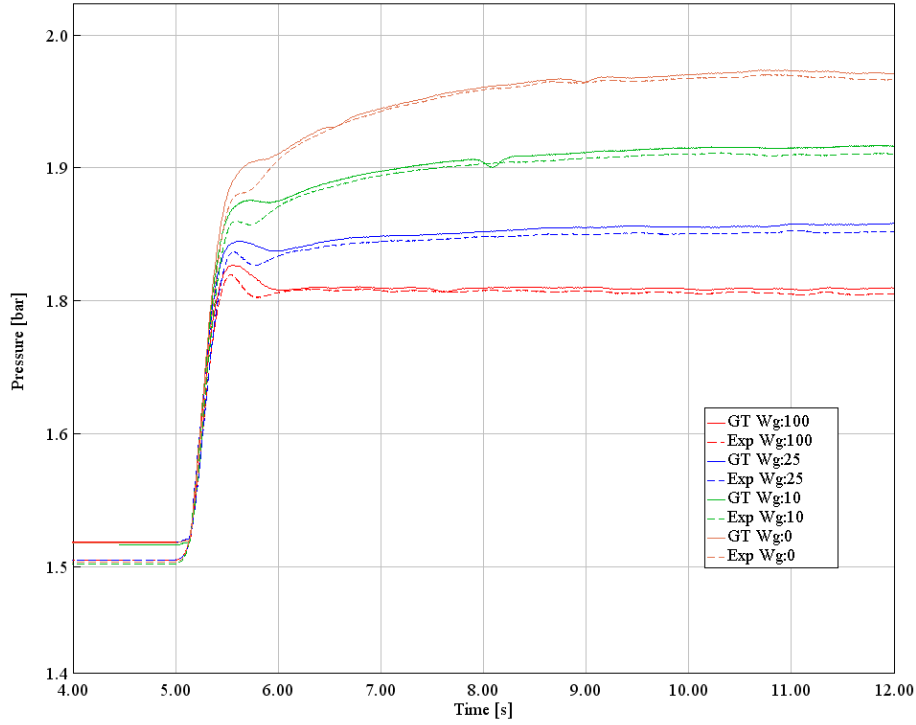
Figure 4.16 – Ps$_2$ trend with initial condition p =1.51 bar and M$_c$=0.026 kg/s. e-compressor target speed: 50000 rpm
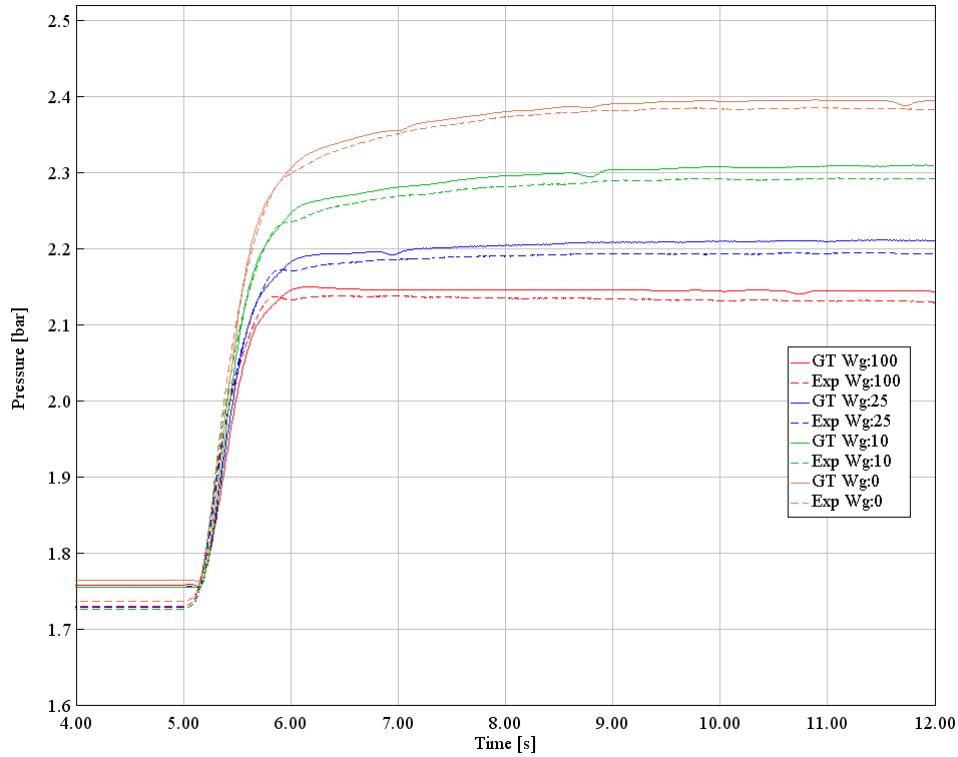

Figure 4.17 – Ps$_2$ trend with initial condition p=1.75 bar and M$_c$=0.03 kg/s. e-compressor target speed: 60000 rpm
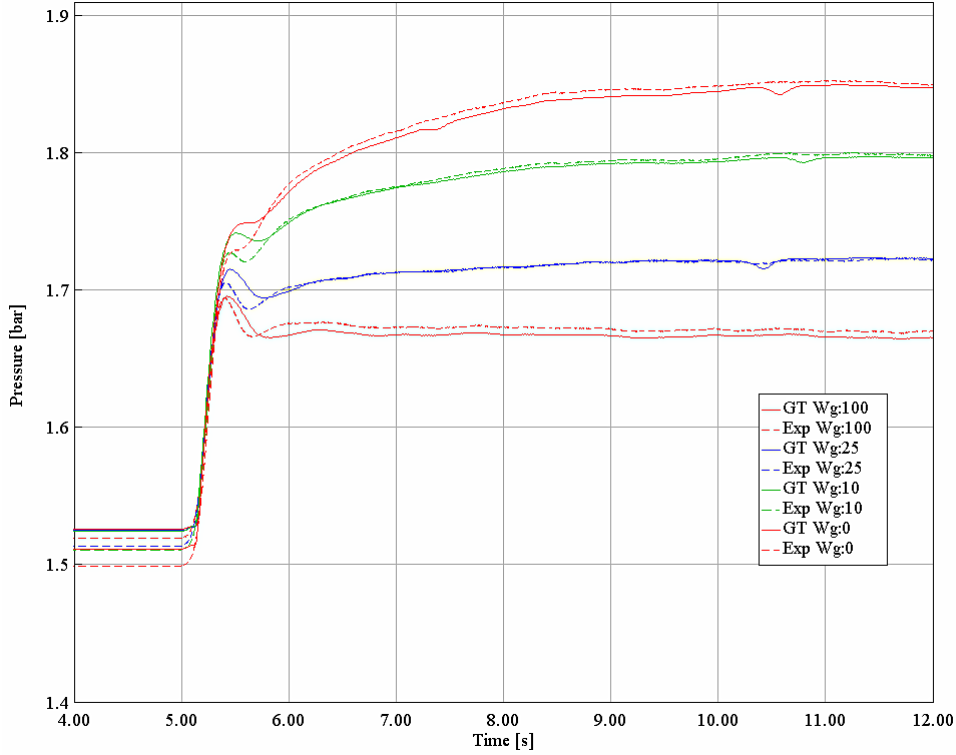
Figure 4.18 – Ps$_2$ trend with initial condition p=1.51 bar and M$_c$=0.026 kg/s. e-compressor target speed: 40000 rpm

In order to demonstrate the goodness level of the model, in Figure 4.19 is shown a comparison on the mass flow rate at the e-compressor outlet. The initial operating point is p =1.51 bar and M$_c$ = 0.026 kg/s and the e-compressor target speed is 50000 rpm. The experimental mass flow rate and the modeled one show a quasi-perfect agreement, especially towards the ending point.

At the beginning of the run the experimental data acquired with the hot film anemometers are unfortunately unusable due to the low speed of the air in this operating condition, therefore a comparison

in this condition is not possible. Anyways the thermal mass flow meter measurements confirm that the model mass flow rate at the beginning of the simulation is indeed correct.
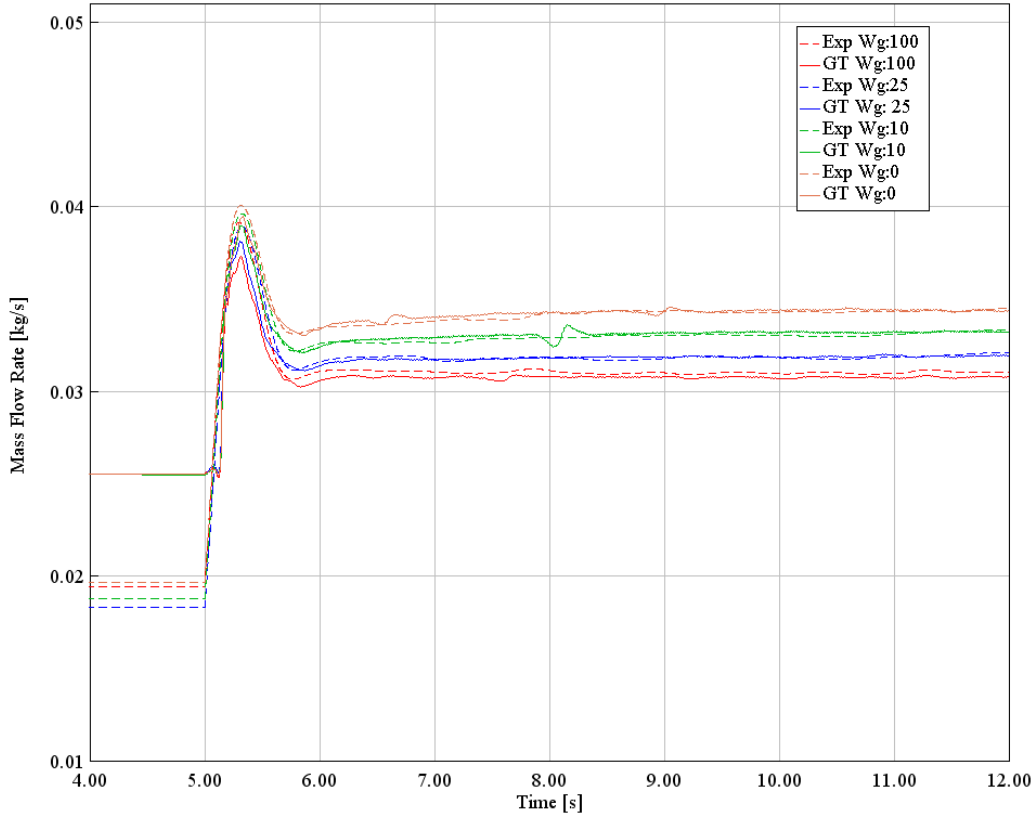

Figure 4.19 – Mass flow rate at e-compressor outlet

In Figure 4.20 is presented a comparison of the second testing typology, already described in chapter 3. The transient response of the system is at first achieved actuating only the traditional turbocharger through the waste-gate position. Secondly the system response is studied by actuating only the eSC. As stated by the experimental activity and then confirmed by the model, the pressure rise time operating the e-compressor is significantly lower than operating the waste-gate valve on the traditional turbocharger.

In order to match the experimental data, the applied PID coefficients are the ones calculated for a 60000 rpm speed ramp even though the imposed speed is 44000 rpm, resulting in a less steeper pressure curve. This fact suggests that the traditional turbocharger installed at the e-compressor outlet avoids to benefit the full potential of the transient response.

Subsequently it is fair to assume that the transient response of the downstream layout with analogue starting and ending conditions is expected to be faster since no component is situated between the e-compressor and the outlet station. This hypothesis is confirmed in the following work.
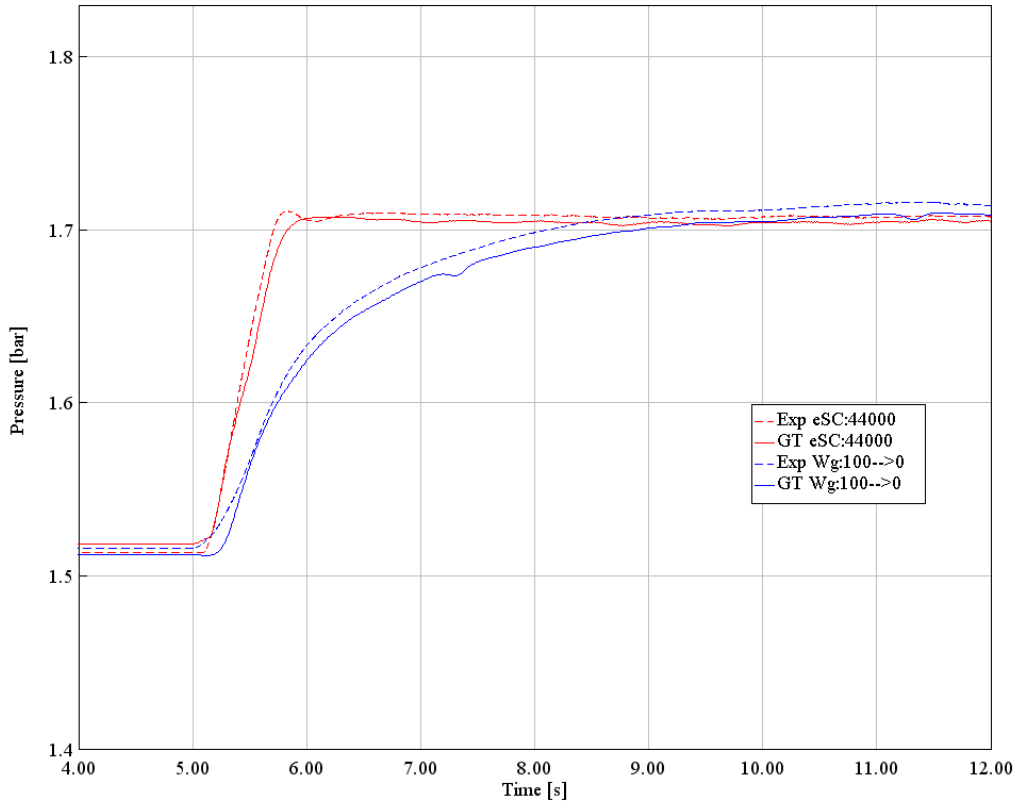
Figure 4.20 – System response in terms of ps_2 with two different actuations

4.4 Downstream model

Like the upstream model, the downstream one is built following the exact dimensions of the testing setup. Also in this case the experimental activity lacks the complete data lineup required to create a model without introducing some approximations.

The experimental layout required the installation of a heat exchanger at the main compressor outlet to prevent high temperatures at the e-compressor inlet since the component is very likely to overheat. GT-Power's library provides several heat exchanger models, however all of them require a complete knowledge of the internal and external dimensions, which are unknown in this case.

Therefore, the component is modeled as a simple pipe, with a diameter corresponding to the exchanger inlet and outlet diameters and a length equal to the exchanger one, in order to roughly maintain the same volumes.

Furthermore, only the inlet temperature of the heat exchanger was acquired during the experimental activity, avoiding to evaluate its performance. Since the component was not actively cooled with forced water, its impact on the line heat exchange rate is overlooked.

Instead, the pressure drop caused by the exchanger geometry is indeed considered. The pressure levels measured at the main compressor outlet, Station 2', and the e-compressor inlet, Station 1', are used to impose a concentrated load loss in the system.

An orifice component is placed in the analyzed section as highlighted in Figure 4.21.
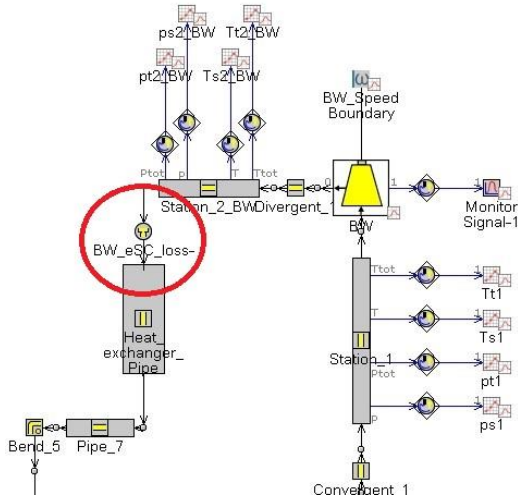
Figure 4.21 – Orifice component

The orifice is the standard component which GT-Power uses to connect all parts, guaranteeing the mass flow continuity as shown in Figure 4.21 by the grey dots in between each connection. If a pressure loss needs to be introduced, the orifice discharge coefficient can be modified to model it. The coefficient is calculated with the same equation used to define the motorized valve characteristic, Equation 4.5.

All the available data are used to evaluate the coefficient and the mean value of the results is then applied in the model. The orifice discharge factor in the downstream model is set to 0.25.

Regarding all the components in common between the two models, they are all exported from the upstream layout and their characterization is untouched, as well as for the performance maps.

As for the heat transfer, the coefficients found for the upstream configuration are applied to the downstream one. In between the two compressors the Nusselt constant multiplier is set to 1.4, while in the section after the e-compressor it is set to 2.5.

In Figure 4.22 is shown the complete downstream configuration model.

Figure 4.22 – Downstream configuration model

4.4.1 Downstream model validation

The model validation is carried out with the same procedure as for the upstream model: the valve is closed accordingly to the mass flow rate target and the pressures are used as validation parameter. In Figure 4.23 the results are presented as operating points on the e-compressor performance map.
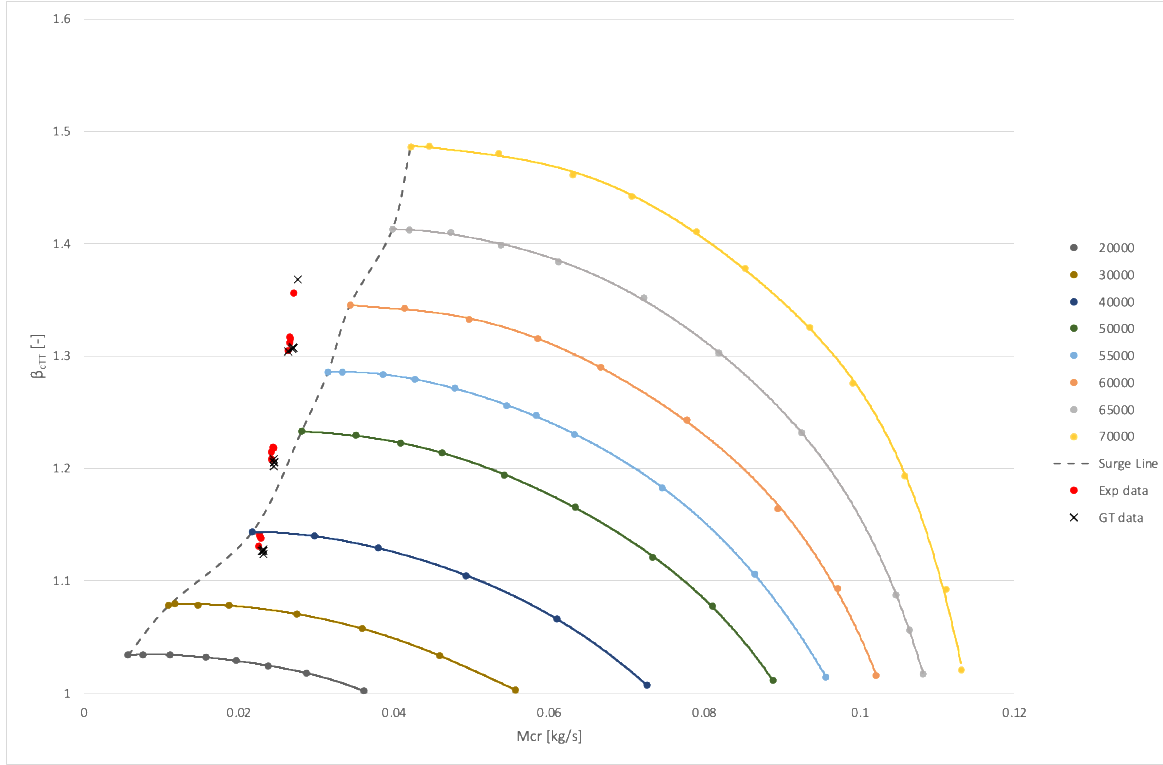

Figure 4.23 – Downstream model operating points

The mean error of the compression ratio between the experimental data and the GT-Power model ones is around 0.05 (c.a. 1%). Note that these values are highly acceptable since the experimental measurement error is of the same order of magnitude. In addition to that it has to be considered that the heat exchanger influence on the e-compressor has been overlooked, causing an average inlet temperature increase of 5°C. As a result the inlet pressure is slightly underestimated, implying another relatively small source of error in the total-to-total evaluation.

From figure 4.23 it is possible to highlight another great quality of the model. As shown by the tested operating points, the compressor works beyond the surge line defined during the steady state experimental campaign. From an experimental point of view this condition is achievable since the surge condition is an instability characteristic of the whole system and not only of the compressor itself. The studied system is completely different from the one used to evaluate the performance maps and it allows an increased field of operation.

Even if the model does not have any information after the surge line, the GT-Power map extrapolation feature automatically evaluates the possible operating conditions and, as proved by the data comparison, it provides good results.

4.4.2 Downstream model in transient conditions

Like for the model validation, also the transient response testing procedure is analogue to the upstream model one. The same PID has been applied during the simulation, proving the goodness of its calibration. Moreover, also the same operating points of the main turbocharger are used as starting points.

4.4.3 Downstream model results

In the Figures 4.24 and 4.25 are presented two comparisons in terms of outlet pressure between the experimental data and the downstream model ones.
In Figure 5.24 the initial operating point is $p = 1.27$ bar and $M_c = 0.022$ kg/s and the e-compressor target speed is 65000 rpm, while in Figure 4.25 the run starts from $p = 1.51$ bar and $M_c = 0.026$ kg/s conditions and the e-compressor accelerates up to 50000 rpm.
Giving the fact that the model required a higher degree of approximation in respect to the upstream one, the results are still very acceptable. A small error trough all pressure levels is detected, however the general pressure trend is precisely replicated.
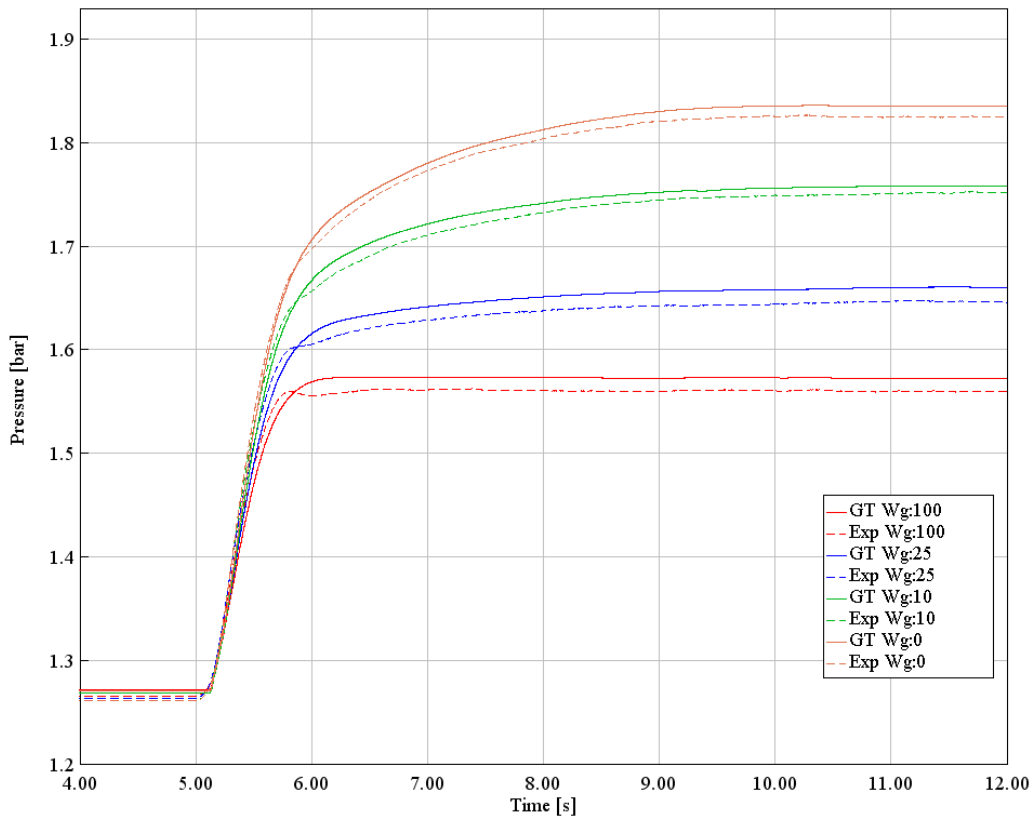

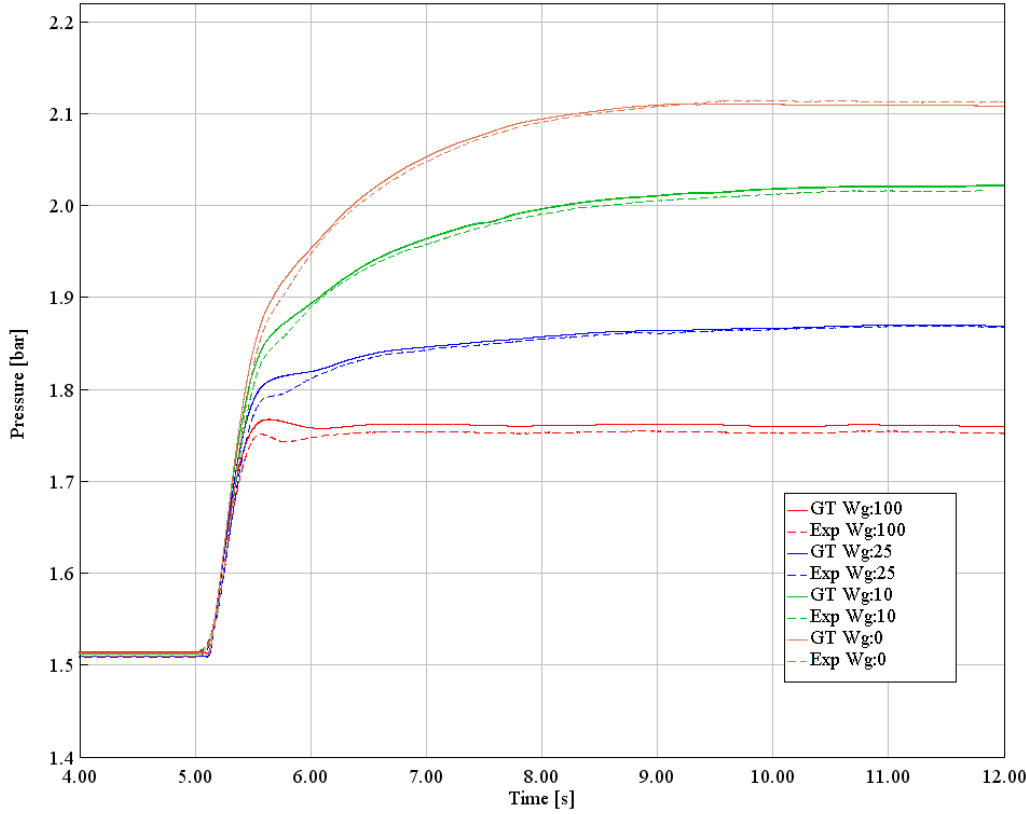*Figure 4.24 – Ps$_2$ trend with initial condition p=1.27 bar and m=0.022 kg/s. e-compressor target speed: 65000 rpm*

Figure 4.25 – Ps₂ trend with initial condition p=1.51 bar and m=0.026 kg/s. e-compressor target speed: 50000 rpm

In Figure 4.26 is presented a comparison of the second testing typology. At first the system response is studied by closing the waste-gate valve and then the test is redone accelerating only the e-compressor to 54500 rpm. The pressure rise caused by the e-compressor transitory is precisely replicated as shown in figure 4.26.

In this case the PID coefficients are evaluated with the Equation 4.8 and 4.9.

Furthermore, it was not possible to replicate the traditional turbocharger transitory due to overspeed issues. In order to maintain the same system operating points in terms of outlet pressure and mass flow rate in both layouts, the downstream model required a higher main turbocharger pressure ratio since more pressure losses are introduced in the system by the longer piping length. But, given the fact that a certain mass flow is required, the only available option has been to raise the main turbocharger speed. By performing the waste-gate transitory tests, the speed raised above the 160000 rpm threshold of the given main compressor maps, resulting impossible for the model to evaluate the traditional compressor operating conditions.
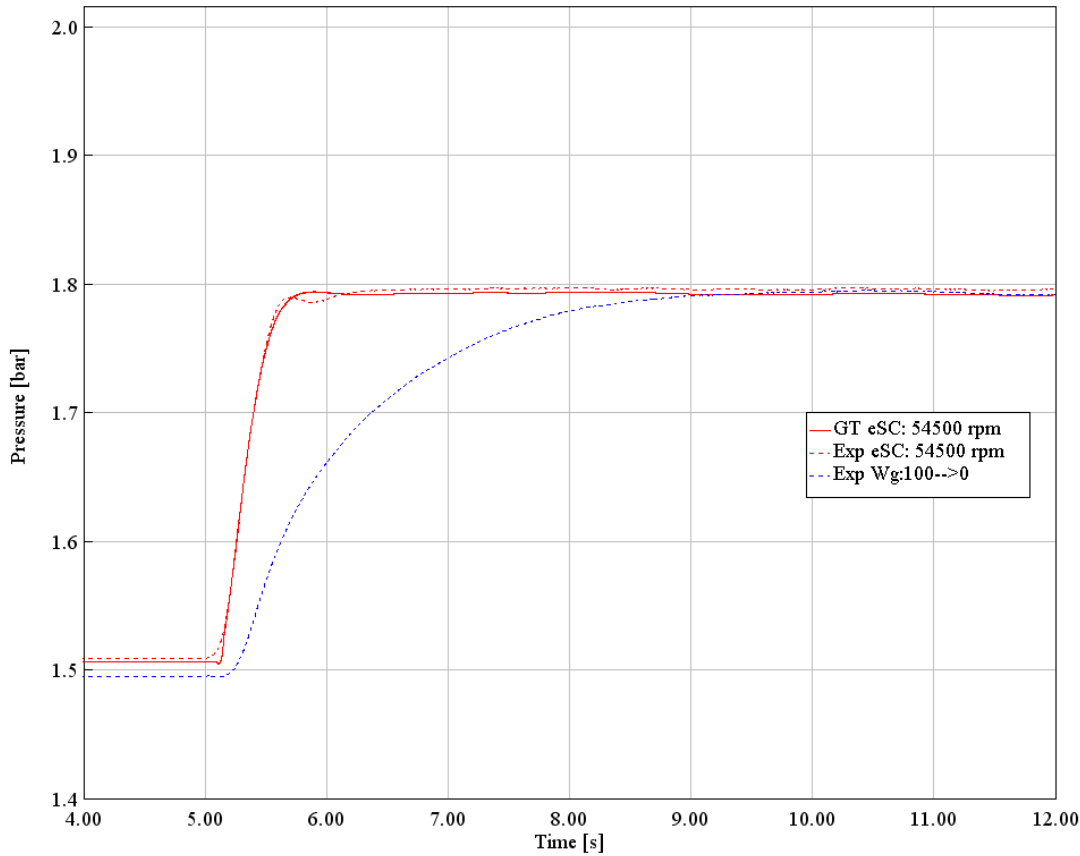
Figure 4.26 – System response in terms of ps₂ with two different actuations

4.5 Reduced volume downstream model

The main purpose of the developed models is their ability to overcome the space restrictions that limit the testing facility in order to compare the transient response of the two layouts.

As previously stated, the downstream configuration required longer connections to be installed at the laboratory. Following the systems dynamics theory, a bigger volume between the turbocharger and the e-compressor means that it is required a longer time to reach the same pressure level with the same input. Therefore, the experimental results allowed no comparison since the downstream model was in disadvantage due to the installation layout.

The downstream model developed with GT-Power, instead, allows downsizing the piping without having any issues.

A second model has been constructed, maintaining the same volume in between the compressors as the one in the upstream configuration. In order to keep the model as realistic as possible, most of the components found in the original downstream configuration has been re-used. The bypass piping has been also maintained to eventually replicate the Y-shaped junction effects on the flow.

In figure 4.27 is shown the downsized downstream model. In order to have the same volume as the upstream configuration, the Pipe_6 shown in the figure is dimensioned to the needs, while the other component dimensions are untouched.

The boundary conditions are the same as for the downstream model and the heat exchange coefficients are not modified. Note that a reduced volume will eventually lead to higher temperatures at the e-compressor inlet, exposing it to the risk of overheating. For the modeling purpose this aspect does not

influence the compressor performance and reliability, but in a real application this should be considered by introducing an intercooler.
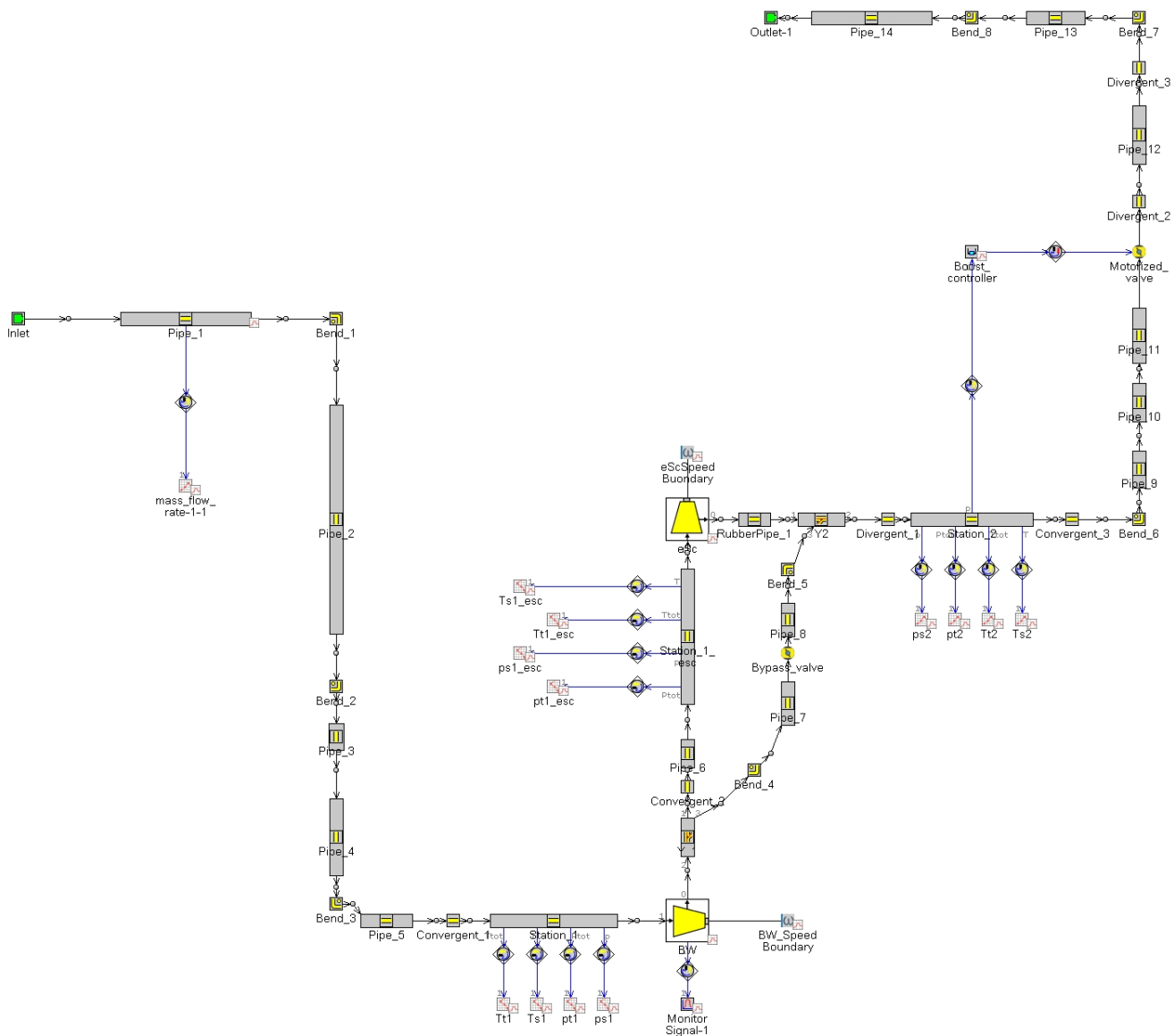

Figure 4.27 – Downsized downstream layout

4.5.1 Reduced volume downstream model results

In Figure 4.28 is presented a comparison between the original downstream layout, drawn in blue color, and the reduced volume configuration, pictured with a red line. The reference operating point of the main compressor is p =1.51 bar and M_c = 0.026 kg/s.

Moreover, the reduced volume model required a lower e-compressor target speed to achieve the same end of run pressure. The reason is to be found in the main compressor speed transitory, which is imposed the same for the two models. However, since the reduced volume model is characterized by less pressure losses, the effect of a higher main compressor speed is an outlet pressure increase, and so a lower e-compressor speed is needed. The same reason is responsible for a higher initial pressure.

As for the response time reduction, a 0.2 seconds difference has been evaluated between the two pressure spikes. Note that this value is only indicative, since the correct measuring procedure would be taking the first stable point of both curves as reference. However, this could not be done since the pressure curve is still influenced by the imposed speed of the main compressor, resulting in a partial invalidation of the pressure profile. A more accurate result could be delivered by creating a turbine model coupled with the compressor and therefore making the model results independent from the experimental one.
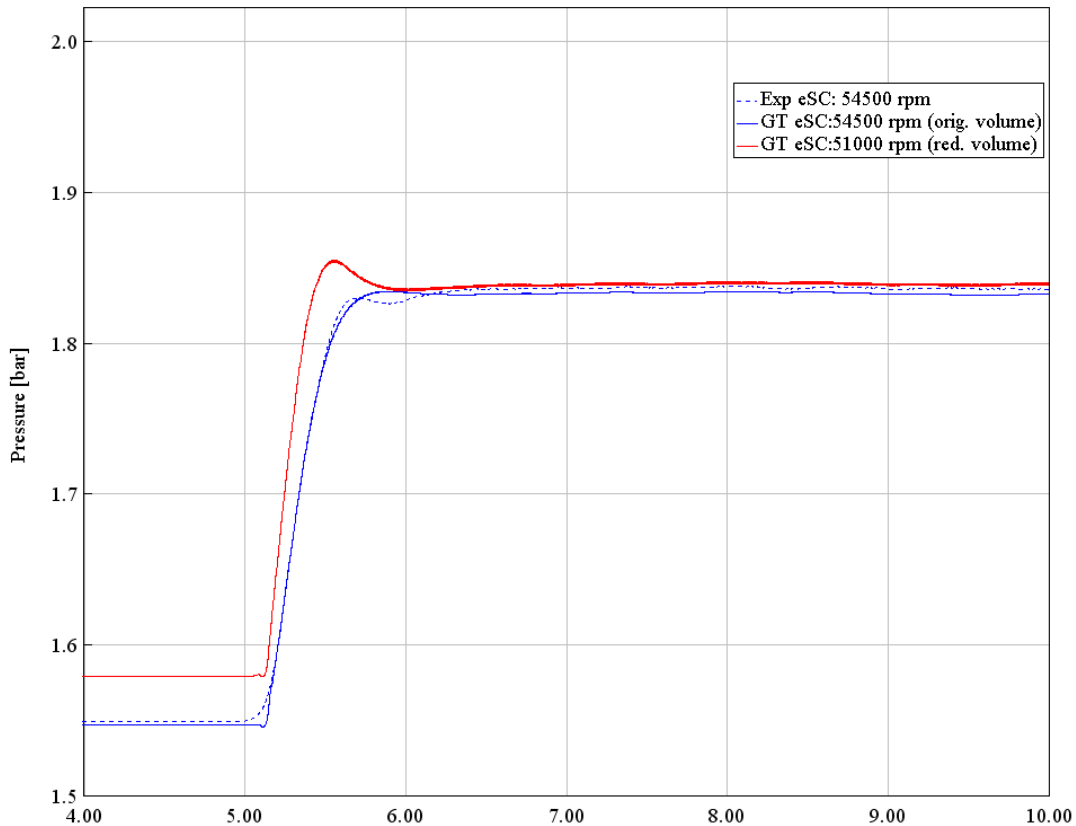

Figure 4.28 – Downstream models comparison

Finally, in Figure 4.29 is presented a comparison between the upstream and downstream configuration. The same initial operating point of the main compressor is taken as reference (p = 1.51 bar and M_c = 0.026 kg/s). As for the downstream model comparison, it has to be made clear that the comparison is limited by imposing the experimental BW speed, therefore not allowing to deliver a perfectly accurate result. However, several considerations can be made from the following outcome. At first, it is clear that the downstream configuration response outperforms by a significant amount the upstream one. In fact, a 0.6 seconds difference has been measured between the relative spikes.

Secondly, in order to have the same pressure output, the e-compressor imposed speed is slightly lower for the downstream configuration, 41000 rpm, in respect to the upstream one, 44000 rpm. In the upstream layout, the main compressor, being installed after the e-compressor, constitutes a limiting factor for the system response due to its high inertial resistance. In addition to that it is highly plausible that it constitutes a not negligible pressure loss. Both these aspects consequently demand a higher e-compressor boost and therefore a higher speed.
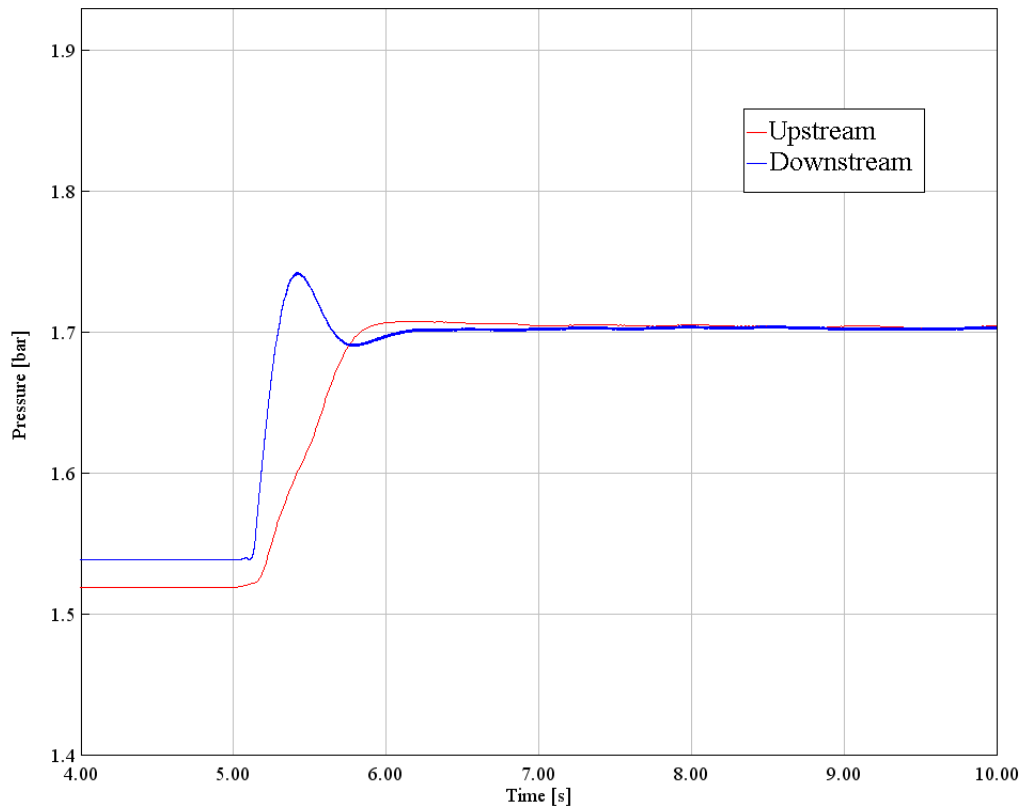

Figure 4.29 – Same volume upstream and downstream layouts comparison

5. Conclusion

The reduction of CO_2 emissions imposed by the European Commission for passenger cars has prompted the automotive industry to develop technological solutions to limit exhaust emissions and fuel consumption, without compromising vehicle performance and drivability.

Vehicle hybridization is a key solution to achieve these goals in the short/medium term, allowing for a limited engine range and thus a limited optimized turbocharger behavior.

In this rapidly developing scenario, it follows that boosting technology will become increasingly relevant as a key technology for spark ignition engines, to improve efficiency, reduce fuel consumption and pollutant emission when electric drive is switched off. Under such conditions, new combustion concepts are likely to require very high boost pressures with unprecedented efficiency demands and challenging transients.

An innovative turbocharging technique is studied in the thesis: an e-compressor coupled in series with a traditional turbocharger in two different layouts, upstream and downstream is studied. In upstream configuration the e-compressor is placed above the traditional turbocharger and in downstream the e-compressor is installed after the traditional turbocharger. All the components have been characterized both in steady and transient state. A new concept for the steady state characterization of electrically assisted compressor has been developed designing a proper driving system to overcome the limits imposed by the electric motor in terms of working time. Moreover, during the thesis an experimental technique to evaluate the time to boost of a twin stage hybrid boosting system have been developed showing some important advantages of this technology. Here are reported the most important goals that can be achieved thank to the adoption of this boosting system:

- In spark ignition engines, this system allows stable transient operations without the adoption of scavenging strategies, that strongly reduce the three-way catalyst efficiency.
- When the e-compressor is activated it is possible to reach the same intake pressure with a more open waste-gate valve position, thanks to this behavior a lower backpressure is imposed to the engine, improving the efficiency of the entire powertrain. Moreover, keeping the waste-gate in a more open position the heating time of the three way catalyst could be significantly faster.
- The modeling and experimental activities confirms that both the upstream and downstream layouts reduced the time-to-boost if compared to a traditional turbocharging system.
- The model demonstrates that the downstream configuration offers the best performance in terms of transient response and overall boost: a smaller volume between the two compressor units improves the promptness of the system.

Moreover, this thesis can provide interesting insights to deepen different aspects, about both experimental and modeling activities.

The experimental activity can be extended evaluating the improvement in the e-compressor performance provided by an increase of the power supply voltage to 48 V, almost the standard for light duty vehicles.

Other important information can be provided by the boosting system installed in the propulsion system on an engine test bench in order to evaluate, not only the time-to-boost, but analyzing directly at the time-to-torque of the whole propulsion system.

The modelling activity can be enhance with the integration of the proposed hybrid boosting system on an engine model in order to evaluate the propulsion system performance and the pollutant emission taking

into account different control strategies of the boosting system on the basis of the battery residual energy. Eventually the system could be integrated on a vehicle model in order to evaluate its impact on driving cycles emissions.

References

[1]   "Worldwide harmonized Light vehicles Test Procedure (WLTP)," UNECE Wiki.

[2]   "Global real driving emissions (RDE)", UNECE Wiki.

[3]   "Official Journal of The European Union L 175", 7 July 2017.

[4]   L. Guzzella, A. Sciaretta, "Vehicle Propulsion Systems", Springer; 2013.

[5]   D. Cardoso, O. Fael, A. Espìrito-Santo, "A review of micro and mild hybrid systems", Energy Reports 6 385–390; 2020.

[6]   M. Nikowitz, "Advanced Hybrid and Electric Vehicles", Springer International Publishing; 2016.

[7]   A.D. Padula, M.S. dos Santos, O.I. Benedetti Santos, D. Borenstein, "Liquid Biofuels: Emergence, Development and Prospects", Springer-Verlag London; 2014.

[8]   Y. Zongyu, S. Sibendu, "Fuel property effects on knock propensity and thermal efficiency in a direct injection spark-ignition engine", Applied Energy; 2019. DOI:10.1016/j.apenergy.2019.114221

[9]   J. Zhao, Q. Xi, S. Wang, S. Wang, "Improving the partial-load fuel economy of 4-cylinder SI engines by combining variable valve timing and cylinder-deactivation through double intake manifolds", Applied Thermal Engineering; 2018. https://doi.org/10.1016/j.applthermaleng.2018.05.087

[10]   L. Teodosio, D. Pirello, F. Berni, V. De Bellis, "Impact of intake valve strategies on fuel consumption and knock tendency of a spark ignition engine", Applied Energy; 2018. DOI:10.1016/j.apenergy.2018.02.032

[11]   Z. Zheng, H. Feng, B. Mao, H. Lui, M. Yao, "A theoretical and experimental study on the effects of parameters of two-stage turbocharging system on performance of a heavy-duty diesel engine", Applied Thermal Engineering; 2018. https://doi.org/10.1016/j.applthermaleng.2017.10.044.

[12]   H. Stoffels, S. Quiring, B. Pingen, "Analysis of Transient Operation of Turbo Charged Engines", SAE International Journal of Engines; 2010. https://doi.org/10.4271/2010-32-0005.

[13]   O.R. Sandoval, M.V. Fonda, V.R. Roso, R.B.R. da Costa, R.M. Valle, J.G.C. Baeta, "Computational technique for turbocharger transient characterization using real driving conditions data", Energy; 2019. DOI: 10.1016/j.energy.2019.07.152.

[14]   K. Zinner," Supercharging of internal combustion engines: Fundamentals, calculations, examples" Springer-Verlag; 1978.

[15]   T. Albin Rajasingham, "Two-Stage Turbocharging: Modeling and Analysis", Advances in Industrial Control; 2021. DOI: 10.1007/978-3-030-68010-7_12.

[16]   M. Keller, S. Severin, K. Kluge, M. Gunther, S. Pischinger, D. Abel, T. Albin, "Setup and Control of a Two-Stage Turbocharged Gasoline Engine with Low Pressure EGR in a Prototype Vehicle", IFAC-PapersOnLine; 2020. DOI: 10.1016/j.ifacol.2020.12.2673.

[17]   Q. Tang, J. Fu, J. Liu, B. Boulet, L. Tang, Z. Zhao, Comparison and analysis of the effects of various improved turbocharging approaches on gasoline engine transient performances, Applied Thermal Engineering (2016). https://doi.org/10.1016/j.applthermaleng.2015.09.063.

[18]   C.A. Rinaldini, S. Breda, S. Fontanesi, T. Savioli, "Two-Stage Turbocharging for the Downsizing of SI V-Engines", Energy Procedia; 2015. DOI: 10.1016/j.egypro.2015.12.077.

[19]   Q. Tang, J. Fu, J. Liu, B. Boulet, L. Tang, Z. Zhao, "Comparison and analysis of the effects of various improved turbocharging approaches on gasoline engine transient performances", Applied Thermal Engineering; 2016. https://doi.org/10.1016/j.applthermaleng.2015.09.063

[20]   H. Dong, Z. Zhao, J. Fu, J. Liu, K. Liang, Q. Zhou, "Experiment and simulation investigation on energy management of a gasoline vehicle and hybrid turbocharger optimization based on equivalent consumption minimization strategy", Energy Conversion and Management; 2020. https://doi.org/10.1016/j.enconman.2020.113518

[21]   M.B. Ricardo, P. Apostolos, M.Y. Yang, "Overview of boosting options for future downsized engines", Science China Technological Sciences; 2011. https://doi.org/10.1007/s11431-010-4272-1

[22]   E. Mattarelli, F. Scrignoli, C.A. Rinaldini, "Parametric Study on Electric Turbocharging for Passenger Cars", SAE Technical Papers; 2020. DOI: 10.4271/2020-01-2224.

[23]   W. Lee, E. Schubert, Y. Li, S. Li, D. Bobba, B. Sarlioglu, "Overview of Electric Turbocharger and Supercharger for Downsized Internal Combustion Engines" IEEE Transactions on Transportation Electrification; 2017. DOI 10.1109/TTE.2016.2620172

[24]   D. Zi, L. Zhang, B. Chen, Q. Zhang, "Study of the electric-booster and turbo-generator system and its influence on a 1.5 L gasoline engine", Applied Thermal Engineeri; 2019. doi.org/10.1016/j.applthermaleng.2019.114236.

[25]   B. An, H. Suzuki, M. Ebisu, H. Tanaka, Development of two-stage turbocharger system with electric supercharger, Lecture Notes in Electrical Engineering; (2013). DOI: 10.1007/978-3-642-33841-0_11.

[26]   K. Nishiwaki, M. Iezawa, H. Tanaka, T. Goto, B. An, "Development of high-speed motor and inverter for electric supercharger", SAE Technical Papers; 2013. doi:10.4271/2013-01-0931.

[27]   M. Schober, "Der neue Audi V6 TDI Motor mit einer innovative Aufladung", Leiter Entwicklung V-Motoren, Audi AG, Neckarsulm.

[28]   KAESER, "kompresory-chlazeni.cz", [Online]. Available: http://www.kompresory-chlazeni.cz/data/file/dokumenty/Kompresory-Kaeser45-75kW-CSD.pdf.

[29]   Parker, "parker.com", [Online]. Available: https://www.parker.com/literature/Finite%20Airtek%20Filtration%20Division/PDF%20Static%20Files/ZANDER%20CAT/Zander%20GL%20Series%20High%20Efficiency%20Filters.pdf.

[30]   CUSSONS TECHNOLOGY, "cussons.co.uk", [Online]. Available: https://www.cussons.co.uk/admin/resources/data-sheets/p7200-17-issue-3-1.pdf.

[31]   Summit Dynamics, Inc., "sdiohio.com", [Online]. Available: http://www.sdiohio.com/Documents/Sylvania%20Heater%20Docs/SureHeat%20Max%20Operating%20Manual%202005%2003%2003.pdf.

[32]   Unitech srl, "unitechsrl.com", [Online]. Available: http://www.unitechsrl.com/wp-content/uploads/2017/06/TF-1.pdf.

[33]   Italcoppie, "italcoppie.com", [Online]. Available: http://www.italcoppie.it/prodotto/trm200-it/.

[34]   Italcoppie, "italcoppie.com", [Online]. Available: http://www.italcoppie.it/prodotto/tcmd-it/.

[35]   Gems Sensors & Controls, "gemssensors.com", [Online]. Available: https://www.gemssensors.com/~/media/files/resources/na_english/catalogpages/catalog-h_2200series-2600series.ashx.

[36]   Kulite, "kulite.com", [Online]. Available: https://www.kulite.com/docs/products/XTEL-190.pdf.

[37]   Kulite, "kulite.com", [Online]. Available: http://www.kulitesensors.com.cn/pdf_Data_Sheets/5-31/ETL-173-190.pdf.

[38]   K. Semiconductor, "Data Sheet MINITUARE AUTOMOTIVE 5VDC OUTPUT IS PRESSURE TRANSDUCER ETL-173-190M".

[39]   ABB, "abb.com", [Online]. Available: https://library.e.abb.com/public/f0b59b01c8d5ae40c1256a0d003b84a0/15_631sd.pdf

[40] Wika, "wika.it", [Online]. Available: https://www.wika.it/dpt_10_it_it.WIKA#:~:text=ll%20trasmettitore%20di%20pressione%20differenziale,per%20condizioni%20di%20processo%20severe.

[41] PRECISION MEASUREMENT TECHNOLOGIES", pmt.com," [Online]. Available: https://www.pmt-fl.com/uploads/2017/09/precision-measurement-db-picoturnbm-e.pdf.

[42] Wika, "wika.it", [online]. Available: https://www.wika.com/en-en/flc_ac_flc_fl_flc_op.WIKA.

[43] EN ISO 5167-2, 2003, "Measurement of fluid flow by means of pressure differential devices inserted in circular cross-section conduits running full – Part 2: Orifice Plates".

[44] M.J. Reader-Harris, "The equation for the expansibility factor for orifice plates", Proceedings of FLOMEKO; 1998.

[45] ABB, "abb.com", [Online]. Available: https://library.e.abb.com/public/ee015c8c6af332ddc1257b0c00547f6c/42-14-40-EN-B-01_05.pdf.

[46] FLOMEC, "flomecmeters.com", [Online]. Available: https://flomecmeters.com/downloads/om-small-data-sheet.pdf.

[47] DANTEC DYNAMICS, "dantecdynamics.com", [Online]. Available: https://www.dantecdynamics.com/components/hot-wire-and-hot-film-probes/single-sensor-probes/fiber-film/.

[48] DANTEC DYNAMICS, "dantecdynamics.com", [Online]. Available: https://www.dantecdynamics.com/solutions-applications/solutions/fluid-mechanics/constant-temperature-anemometry-cta/minicta/.

[49] CB PIEZOTRONICS, "pcb.com", [Online]. Available: https://www.pcb.com/products?m=352C33.

[50] Brüel & Kjær, "bskv.com", [Online]. Available: https://www.bksv.com/-/media/literature/Product-Data/bp2043.ashx.

[51] G.R.A.S. Sound & Vibration, "gras.dk", [Online]. Available: https://www.gras.dk/products/measurement-microphone-cartridge/prepolarized-cartridges-0-volt/product/ss_export/pdf2?product_id=150.

[52] G.R.A.S. Sound & Vibration, "gras.dk", [Online]. Available: https://www.gras.dk/files/p/d/pd_26ca_cs4_04022010.pdf.

[53] BELL Electronics, "bellnw.com", [Online]. Available: https://www.bellnw.com/downloads/datasheet/Agilent/34980A.pdf.

[54]   National Instruments, "ni.com", [Online]. Available: http://www.ni.com/pdf/product-flyers/multifunction-io.pdf.

[55]   National Instruments, "ni.com", [Online]. Available: https://www.ni.com/pdf/manuals/375212c.pdf.

[56]   AVL, "avl.com", [Online]. Available: https://www.avl.com/-/avl-e-storage-lv.

[57]   S. Marelli, G. Marmorato, M. Capobianco, "Evaluation of heat transfer effects in small turbochargers by theoretical model and its experimental validation", Energy; 2016. DOI: 10.1016/j.energy.2016.06.067.

[58]   A. Diango, C. Périlhon, G. Descombes, E. Danho, "Application of exergy balances for the optimization of non-adiabatic small turbomachines operation" Energy; 2011. DOI 10.1016/j.energy.2011.02.035.

[59]   S. Marelli, V. Usai, M. Capobianco, G. Montenegro, A. Della Torre, A. Onorati, "Direct evaluation of turbine isentropic efficiency in turbochargers: Cfd assisted design of an innovative measuring technique", SAE Technical Papers; 2019. DOI 10.4271/2019-01-0324.

[60]   P. Olmeda, V. Dolz, F. J. Arnau, M. A. Reyes-Belmonte, "Determination of heat flows inside turbochargers by means of a one dimensional lumped volume," Mathematical and Computer Modelling; 2011

[61]   N. Watson and S. Janota, "Turbocharging the Internal Combustion Engine", London: MacMillan Publishers Ltd.; 1982

[62]   S. Marelli and M. Capobianco, "Steady and pulsating flow efficiency of a waste-gated turbocharger radial flow turbine for automotive application", Energy; 2010. DOI 10.1016/j.energy.2010.10.019.

[63]   S. Marelli, G. Marmorato and M. Capobianco, "Evaluation of heat transfer effects in small turbochargers by theoretical model and its experimental validation", Energy; 2016. DOI 10.1016/j.energy.2016.06.067.

[64]   P. Enyon, A. Whitfiled, "Pressure recovery in a turbocharger compressor volute", in Proc Inst Mech Eng Part A J Power Energy; 2000.

[65]   G. Sovran, E. Klomp, "Experimentally determined optimum geometries for rectilinear diffusers with rectangular conical or annular cross section", Fluid mechanics of internal flow; 1967.

[66]   B. Sirakov, M. Casey, "Evaluation of Heat Transfer Effects on Turbocharger Performance", Journal of Turbomachinery; 2013. DOI 10.1115/1.4006608.

[67]   P. Dalbert, M. Casey, E. Schurter, "Development, testing and performance prediction of radial stages for multi-stage industrial compressors", ASME Journal of Turbomachinery; 1988.

[68]   J. Daily, R. Nece, "Chamber dimension effect on induced flow and frictional resistance of enclosed rotating disks", J Basic Eng; 1960.

[69]   R. Jalnekar, "Pulse-Width-Modulation Techniques: A Review", IETE Journal of Research; 2015.

[70]   M. Di Natale, P. Giusto, H. Zeng, A. Ghosal, "Understanding and Using the Controller Area Network Communication Protocol", Theory and Practice, 2012.

[71]   S.A Fist, "The Informatics Handbook: A guide to multimedia communications and broadcasting", Chapman and Hall; 1996.

[72]   N. Bontemps, A. Bas, M. Ladonnet, D. Zecchetti, S. Heints, P. Davies, "Electric turbo, a key technology to achieve Eu7 hybridized powertrain (lambda 1, performance and energy efficiency)",) Internationaler Motorenkongress 2019. Proceedings. Springer Vieweg, Wiesbaden; 2019. https://doi.org/10.1007/978-3-658-26528-1_6.

[73]   Gamma Technologies, GT-Power Training - Engine Performance Analysis.

A Appendix: Test Bench Details
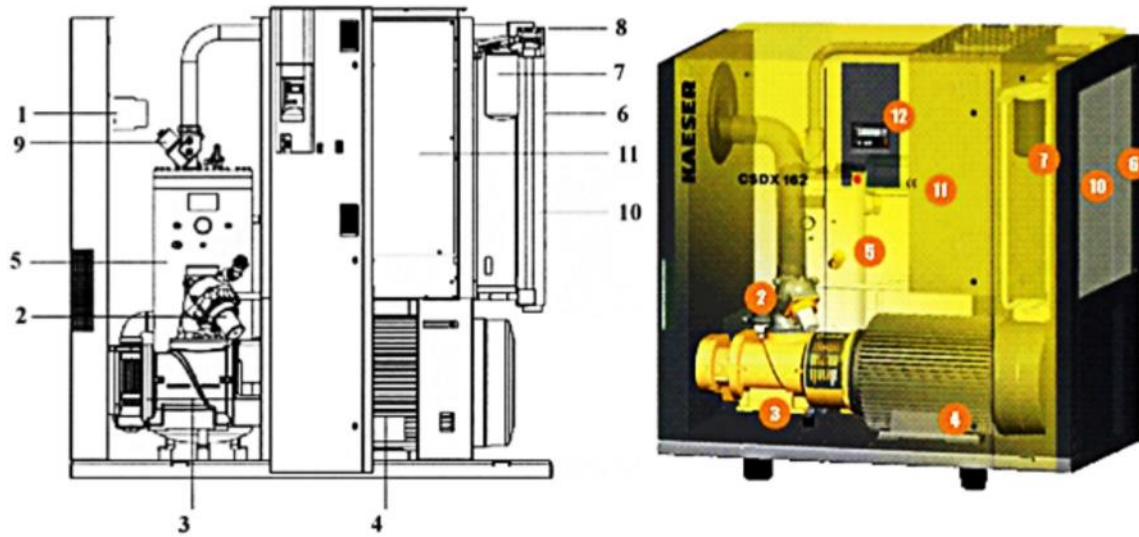
1	Inlet filter	7	Oil filter
2	Air inlet valve	8	Thermostatic valve
3	Screw compressor	9	Control valve
4	Electric motor	10	Heat exchanger
5	Air-oil separator	11	Electrical panel
6	Cooler	12	Sigma control system

Figure A-0.1 – KAESER Screw Compressor
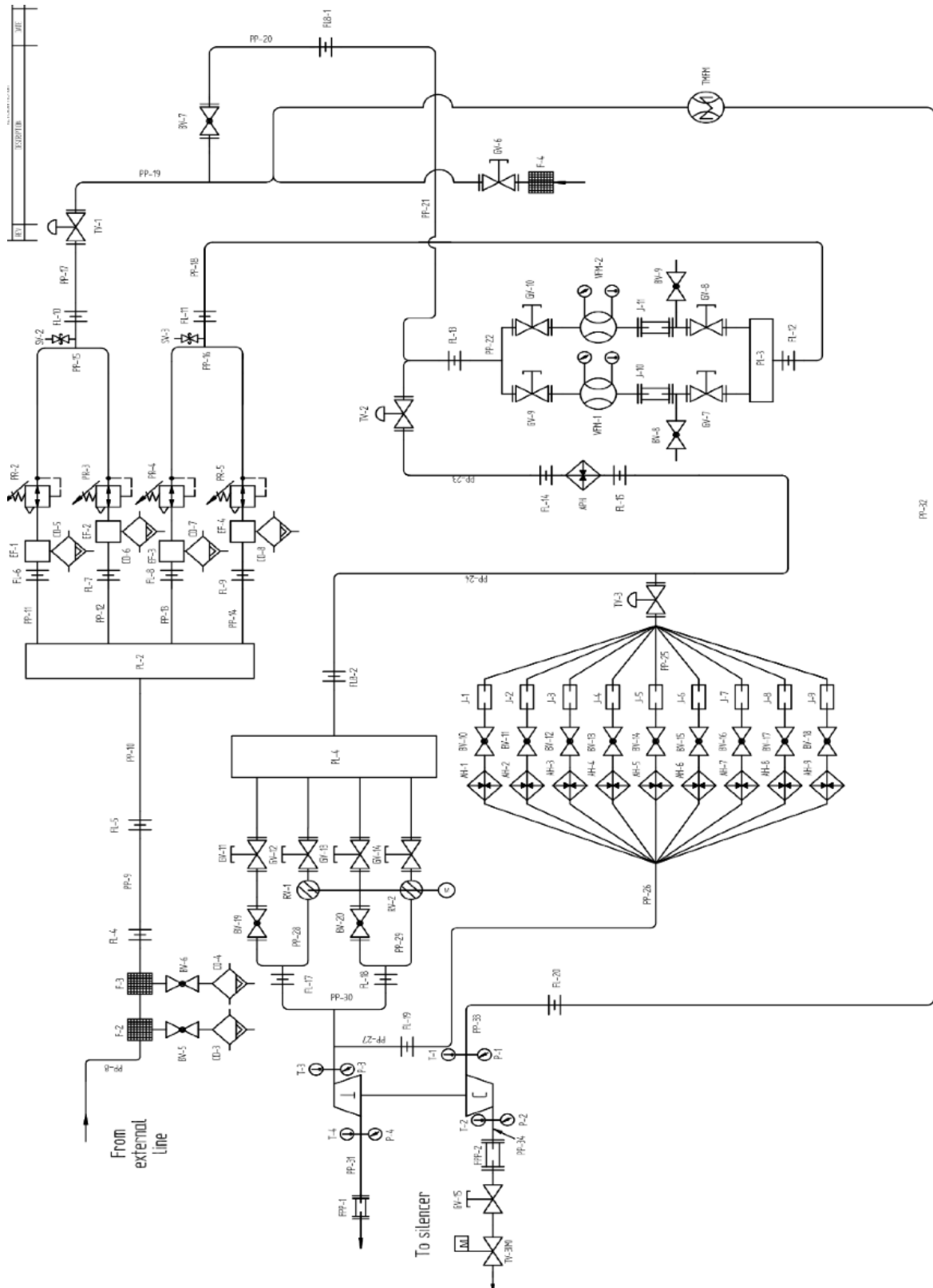
Figure A-0.2 - Lab Schematic Representation

Acronym	Significance	Symbol
AD	Air Drier	
AH	Air Heater	
APH	Air Pre-heater	
BV	Ball Valve	
CD	Condense Discharger	
EF	Empty Filter	
F	Filter	
FL	Flange	
FPP	Flexible Pipe	
GV	Gate Valve	
J	Joint	
M	Motor	
P	Pressure	
PL	Plenum	
PP	Pipe	
PR	Pressure Regulator	
RV	Rotating Valve	
SC	Screw	
SV	Safety Valve	
T	Temperature	
TMFM	Thermal Mass Flow Meter	
TV	Throttle Valve	
VFM	Viscous Flow Meter	

(M) indicates a motorized component

Table A-0.1 – Legend for Figure 2.22.2, Figure2.3, Figure2.5 and Figure 2.62.6

Figure A-0.3 – A Single Electrical Heater Element and Electro-Pneumatic Valve

B Appendix: Measuring Equipment Details

Figure B-0.1 – Pt100 Resistance Thermometers

Figure B-0.1 – K-Type Thermocouple

CODE	MANUFACTURER	MODEL	RANGE	PRESSURE CONNECTION	TEMP. COMPENS.	OUTPUT VOLTAGE	ACCURACY
7.01	Gems Sensors	2600SGA2500G3UB	0÷2.5 bar VG	G 1/4" (f)	-54÷120 °C	10V±1mV	±0.15% f.s.
7.02	Gems Sensors	2600SGA2500G3UB	0÷2.5 bar VG	G 1/4" (f)	-54÷120 °C	10V±1mV	±0.15% f.s.
7.03	Gems Sensors	2600SGA2500G3UB	0÷2.5 bar VG	G 1/4" (f)	-54÷120 °C	10V±1mV	±0.15% f.s.
7.04	Gems Sensors	2600SGA4000G3UB	0÷4 bar VG	G 1/4" (f)	-54÷123 °C	10V±1mV	±0.15% f.s.
7.05	Gems Sensors	2600SGA4000G3UB	0÷4 bar VG	G 1/4" (f)	-54÷123 °C	10V±1mV	±0.15% f.s.
7.06	Sensing & Inspection Technologies	A5076TBA2CAHOPA	0÷2.5 bar VG	G 1/4" (f)	-20÷80 °C	10V±1mV	±0.1% f.s.
7.07	Sensing & Inspection Technologies	A5076TBA2CAHOPA	0÷2.5 bar VG	G 1/4" (f)	-20÷80 °C	10V±1mV	±0.1% f.s.
7.08	Sensing & Inspection Technologies	A5076TBA2CAHOPA	0÷4 bar VG	G 1/4" (f)	-20÷80 °C	10V±1mV	±0.1% f.s.
7.09	Sensing & Inspection Technologies	A5076TBA2CAHOPA	0÷4 bar VG	G 1/4" (f)	-20÷80 °C	10V±1mV	±0.1% f.s.
7.10	Sensing & Inspection Technologies	A5076TBA2CAHOPA	0÷0.35 bar VG	G 1/4" (f)	-20÷80 °C	10V±1mV	±0.1% f.s.
7.11	Sensing & Inspection Technologies	A5076TBA2CAHOPA	0÷0.35 bar VG	G 1/4" (f)	-20÷80 °C	10V±1mV	±0.1% f.s.
7.12	Sensing & Inspection Technologies	A5076TBA2CAHOPA	0÷0.35 bar VG	G 1/4" (f)	-20÷80 °C	10V±1mV	±0.1% f.s.
7.13	Sensing & Inspection Technologies	A5076TBA2CAHOPA	0÷0.35 bar VG	G 1/4" (f)	-20÷80 °C	10V±1mV	±0.1% f.s.
7.14	Kulite Semiconductor	XTEL-37-IA-190M-65PSIG	0÷4.48 bar G	M5 (m)	25÷232 °C	500mV±50 mV	±0.1% f.s.
7.15	Kulite Semiconductor	XTEL-37-IA-190M-65PSIG	0÷4.48 bar G	M5 (m)	25÷232 °C	500mV±50 mV	±0.1% f.s.
7.16	Kulite Semiconductor	XTEL-37-IA-190M-65PSIG	0÷4.48 bar G	M5 (m)	25÷232 °C	500mV±50 mV	±0.1% f.s.
7.17	Kulite Semiconductor	XTEL-37-IA-190M-65PSIG	0÷4.48 bar G	M5 (m)	25÷232 °C	500mV±50 mV	±0.1% f.s.
7.18	Kulite Semiconductor	XTEL-37-IA-190M-65PSIG	0÷4.48 bar G	M5 (m)	25÷232 °C	500mV±50 mV	±0.1% f.s.
7.19	Kulite Semiconductor	XTEL-37-IA-190M-65PSIG	0÷4.48 bar G	M5 (m)	25÷232 °C	500mV±50 mV	±0.1% f.s.
7.20	Kulite Semiconductor	XTEL-37-IA-190M-65PSIG	0÷4.48 bar G	M5 (m)	25÷232 °C	500mV±50 mV	±0.1% f.s.
7.21	Kulite Semiconductor	ETL-173-190M-2BARA	0÷2 bar A	M5 (m)	20÷120 °C	500mV±50 mV	±0.1% f.s.
7.22	Kulite Semiconductor	ETL-173-190M-1.7BARA	0÷1.7 bar A	M5 (m)	-40÷177 °C	500mV±50 mV	±0.1% f.s.
7.23	Kulite Semiconductor	ETL-175-190M-1.7BARA	0÷1.7 bar A	M5 (m)	-40÷177 °C	500mV±50 mV	±0.1% f.s.

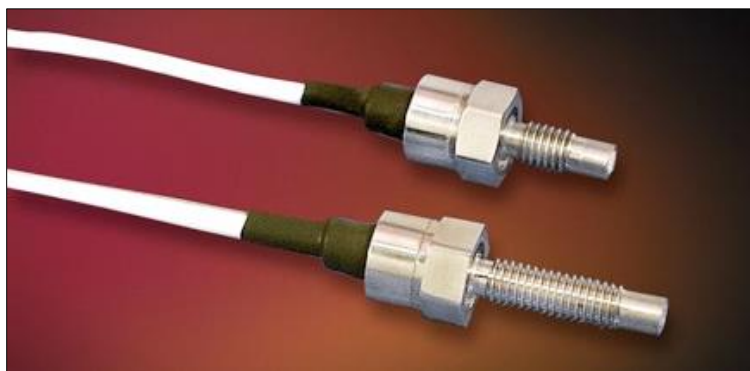*Table B-0.1 – Pressure Sensors' Characteristics*
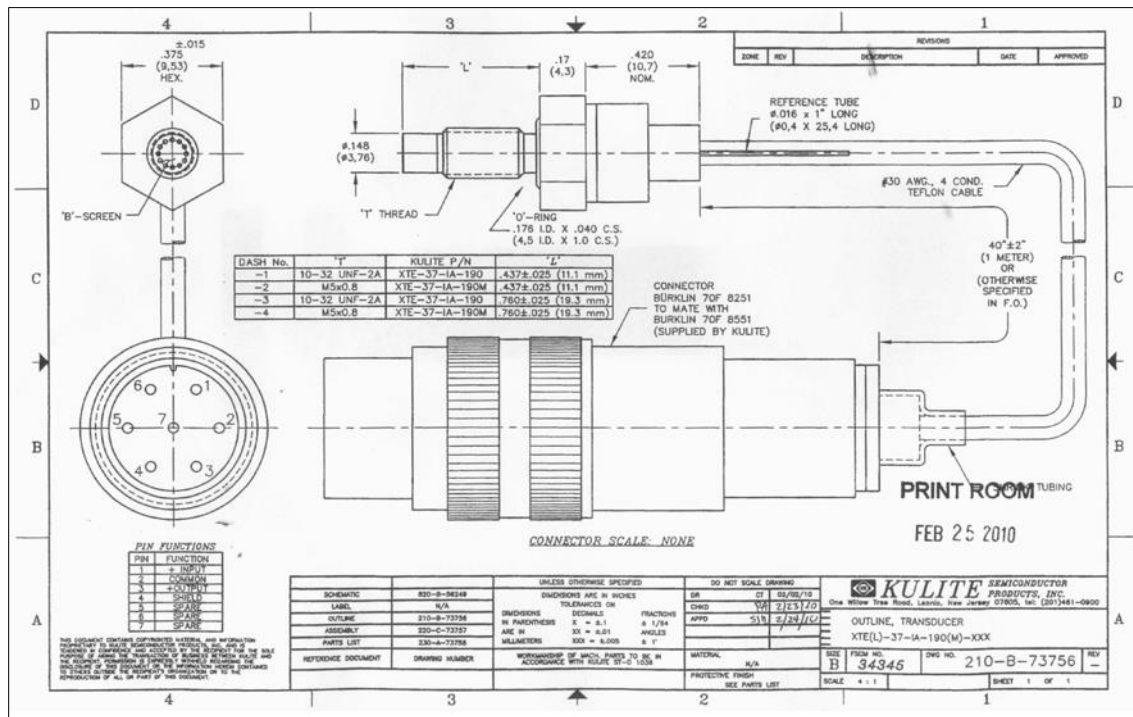

Figure B-0.3 – Kulite Sensors

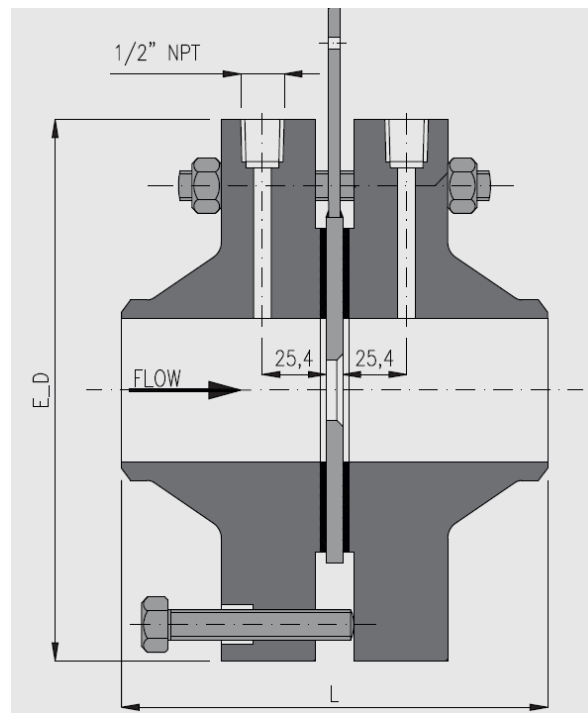*Figure B-0.4 – Schematic Representation of Kulite Transducers*

Figure B-0.5 – Schematic Representation of Flanges with Calibrated Orifice and main geometrical data

Figure B-0.6 – ABB Sensyflow FTM500-IG

Figure B-0.7 – Accelerometer PCB 352C33

Figure B-0.8 – Accelerometer Brüel & Kjær type 4393

Figure B-0.9 – Microphone G.R.A.S. 40AE 1/2"

Figure B-0.10 – Microphone G.R.A.S. 26CA 1/2" CCP

117

Figure B-0.11 – AGILENT 34980A Data Acquisition System

Details on TURBO acquisition code

The acquisition code TURBO requires a number of input files with a specific identification. Input and output files are defined through a technique previously established by the research group which allows the operator to easily identify the tested components and the type of test. For this reason, the component number (nt) and the test configuration (cfg) need to be specified before the start of a test. The test number (ppp), the test point (p) and the number of measurements for each test point (m) also need to be provided. The input files are:

- CONFIG_nt_cfg.txt contains general information on the test,

- CANALI_nt_cfg.txt contains information on the measured parameters with the respective measurements channel number and sensor code,

- DIMGRUPPO_nt_cfg.txt contains information on the tested turbocharger's geometric characteristics and dimensions;

- VIELABORAZIONE_nt_cfg.txt contains a list of the Virtual Instruments (sub-Vis) used for the first phase of data post-processing;

- TRASDUTTORI AMPLIFICATI.txt contains the calibration coefficients for all pressure sensors;

- FATTORE DI VISCOSITÀ.txt allows the software to calculate the mass flow rate value from the laminar mass flow meter signal.

The code provides as output files:

- V_nt_ppp_p_m.txt is created after the acquisition of each measurement and records the different readings of the measures used to more accurately calculatedly the average value,

- T_nt_ppp.txt contains the values of the quantities that were directly measured (i.e. total temperature and static pressure) and the ones derived from the measured quantities (i.e. power and efficiency);

- CFG_nt_ppp.txt: contains general information on the test.

C Appendix: C++ code for waste gate valve control system

```cpp
//define pin name
#define pwm_1 13
#define dir_1 7
#define pwm_2 11
#define dir_2 4
#define sensor1 A0
#define sensor2 A3
#define posmin1 53
#define posmax1 973
#define posmin2 163.0
#define posmax2 963.0



// Pid parameters
typedef struct{
  double Kp;
  double Ki;
  double Kd;
  float last_error;
  float error;
  float changeError;
  float totalError;
  float pidTerm;
  int pwm_value;
  float setpoint;
} PID;

PID pid1 = {15, 0.00032, 0, 0, 0, 0, 0, 0, 0, 0};
PID pid2 = {25, 0.001, 0, 0, 0, 0, 0, 0, 0, 0};

float sensor_read1;
int pwm_value1;
float sensor_read2;
int pwm_value2;

void setup(){
//declare pins as INPUT/OUTPUT
pinMode(pwm_1, OUTPUT);
pinMode(dir_2, OUTPUT);
pinMode(pwm_2, OUTPUT);
pinMode(dir_2, OUTPUT);
pinMode(A0, INPUT);
```

```
pinMode(A3, INPUT);
Serial.begin(19200);
}


void loop(){
InitCpuTick();
ParserCmd();
sensor_read1 = float ((analogRead(sensor1)) - posmin1)*100/(posmax1-posmin1);
sensor_read2 = float ((analogRead(sensor2)) - posmin2)*100/(posmax2-posmin2);

PIDcalculation1();
if (sensor_read1 < pid1.setpoint) {
  digitalWrite(dir_1, HIGH);// Forward motion
 } else {
  digitalWrite(dir_1, LOW);//Reverse motion
 }

analogWrite(pwm_1, pid1.pwm_value);
Serial.print("pwm_value1 = ");
Serial.print(pid1.pwm_value); //Display the value of PWM
Serial.print(" posizione valvola = ");
Serial.println(sensor_read1); //Display the value of sensor


PIDcalculation2();
if (sensor_read2 < pid2.setpoint) {
  digitalWrite(dir_2, LOW);// Forward motion
 } else {
  digitalWrite(dir_2, HIGH);//Reverse motion
  pid2.pwm_value=pid2.pwm_value/10;
 }

analogWrite(pwm_2, pid2.pwm_value);
Serial.print("pwm_value2 = ");
Serial.print(pid2.pwm_value); //Display the value of PWM2
Serial.print(" posizione valvola farfalla = ");
Serial.println(sensor_read2); //Display the value of sensor
Serial.println(pid2.setpoint);
DelayCpuTick();
}

void PIDcalculation1(){

 pid1.error = pid1.setpoint - sensor_read1;
```

```
  pid1.changeError = pid1.error - pid1.last_error; // derivative term
  pid1.totalError += pid1.error; //accumalate errors to find integral term
  pid1.pidTerm   =   (pid1.Kp   *   pid1.error)   +   (pid1.Ki   *   pid1.totalError)   +   (pid1.Kd   *
pid1.changeError);//total gain
  pid1.pidTerm = constrain(pid1.pidTerm, -255, 255);//constraining to appropriate value
  pid1.pwm_value = max (int (abs(pid1.pidTerm)), 2);//make sure it's a positive value
  pid1.last_error = pid1.error;
}

void PIDcalculation2(){

  pid2.error = pid2.setpoint - sensor_read2;

  pid2.changeError = pid2.error - pid2.last_error; // derivative term
  pid2.totalError += pid2.error; //accumalate errors to find integral term
  pid2.pidTerm   =   (pid2.Kp   *   pid2.error)   +   (pid2.Ki   *   pid2.totalError)   +   (pid2.Kd   *
pid2.changeError);//total gain
  pid2.pidTerm = constrain(pid2.pidTerm, -255, 255);//constraining to appropriate value
  pid2.pwm_value = max (int (abs(pid2.pidTerm)), 2);//make sure it's a positive value
  pid2.last_error = pid2.error;
}
```

D Appendix: C++ code for e-compressor and by-pass valve control system

```cpp
#include <SPI.h>
#include <mcp2515.h>
#define pwm_1 5
#define dir_1 7
#define PinMaster 8
#define PinTrigger 4

unsigned long previousMillis = 0;
long interval = 9;
struct can_frame canMsgR;
struct can_frame canMsgW;
long Speed_setpoint;
long Speed;
long Speed_master;
float BP_target;
bool tolerance = false;
float threshold = 10;
long Speed_int;
bool key_on = false;
int MasterPin_status = LOW;
int prevMasterPin_status = LOW;
bool BP_close = false;



MCP2515 mcp2515(10);


void setup() {
  pinMode(PinMaster, INPUT);
  pinMode(PinTrigger, OUTPUT);
  canMsgW.can_id  = 0x112;
  canMsgW.can_dlc = 8;
  canMsgW.data[0] = 0x00; //key off
  canMsgW.data[1] = 0xFD;
  canMsgW.data[2] = 0x00;
  canMsgW.data[3] = 0x17;
  canMsgW.data[4] = 0x70;
  canMsgW.data[5] = 0xD8;
  canMsgW.data[6] = 0x09; //idle speed
  canMsgW.data[7] = 0xC4; //idle speed
```

```
  Serial.begin(115200);
  SPI.begin();

  mcp2515.reset();
  mcp2515.setBitrate(CAN_500KBPS, MCP_8MHZ);
  mcp2515.setNormalMode();

  Serial.println("------- CAN Read ----------");
  Serial.println("ID  DLC   DATA");
}

void loop() {
 unsigned long currentMillis = millis();
 float CmdValue;
 ParserCmd();
 MasterPin_status = digitalRead(PinMaster);
 if ((MasterPin_status == HIGH) && (prevMasterPin_status == LOW)) { //se arriva il master, chiave è
on. Master arriva solo se anche start è on
   digitalWrite(PinTrigger, HIGH);
   canMsgW.data[0] = 0x4A;
   CmdValue = Speed_master;
   CmdValue = CmdValue/2;
   canMsgW.data[6] = (int(CmdValue) & 0xFF00)>>8;
   canMsgW.data[7] = int(CmdValue) & 0x00FF;
   if (!key_on) Speed_setpoint = Speed_master;
   key_on = true;
   if (BP_target > 5000){
    BP_close = true;
     }
    }
  if ((MasterPin_status == LOW) && (prevMasterPin_status == HIGH)) { //se levi il master, key on,
5000 rpm. Master arriva solo se anche start è on
   digitalWrite(PinTrigger, LOW);
   canMsgW.data[0] = 0x4A;
   canMsgW.data[6] = 0x09; //idle speed
   canMsgW.data[7] = 0xC4; //idle speed
   Speed_setpoint = 80000; // lasciare aperto bypass
   key_on = true;
   BP_close = false;
    }
  prevMasterPin_status = MasterPin_status;


  // invio msg su CAN ogni 10ms
  if(currentMillis - previousMillis > interval) {
   mcp2515.sendMessage(&canMsgW);
```

```
    previousMillis=currentMillis;
  }
  else {
  // lettura CAN
  if (mcp2515.readMessage(&canMsgR) == MCP2515::ERROR_OK)
  {
   // lettura velocità
   //Speed_int = (int(canMsgR.data[4])<<8) | (int(canMsgR.data[5]));
   Speed_int = (long(canMsgR.data[4])*256 + (long(canMsgR.data[5])));
   Speed = (Speed_int*2);
    if (((Speed_setpoint-Speed)/Speed_setpoint*100) < threshold){
    tolerance = true;}
    else {
    tolerance = false;}
    if (((tolerance == true) && (key_on == true)) || (BP_close == true))
    { // chiudi valvola 5v continui a scheda cyt (pwm 255 or DO high low)
     analogWrite(pwm_1, 255);
    }
   if(((key_on == false) || (tolerance == false)) || (BP_close == false)) {
    analogWrite(pwm_1, 0);
    }

   Serial.print(canMsgR.can_id, HEX); // print ID
   Serial.print(" ");
   Serial.print(canMsgR.can_dlc, HEX); // print DLC
   Serial.print(" ");

   for (int i = 0; i<canMsgR.can_dlc; i++)  {  // print the data

    Serial.print(canMsgR.data[i],HEX);
    Serial.print(" ");
    }
   Serial.println();
  }

 }
} // end loop
```